RICE UNIVERSITY

Deformation Styles of Allochthonous Salt Sheets during Differential Loading Conditions: Insights from Discrete Element Models

by

Scott Allen Maxwell

A THESIS SUBMITTED
IN PARTIAL FULFILLMENT OF THE
REQUIREMENTS FOR THE DEGREE

Master of Science

APPROVED, THESIS COMMITTEE:

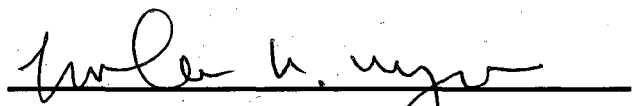

Julia K. Morgan, Associate Professor, Chair
Earth Science

John B. Anderson, W. Maurice Ewing Professor
Earth Science

Brandon Dugan, Assistant Professor
Earth Science

HOUSTON, TEXAS
MAY 2009

ABSTRACT

Deformation Styles of Allochthonous Salt Sheets during Differential Loading Conditions: Insights from Discrete Element Models

by

Scott Allen Maxwell

The Discrete Element Method (DEM) was used to model the advance of allochthonous salt sheets through differential loading. The effects of basal slope angle, initial salt thickness, sediment thickness, loading time, progradation rate, and the mechanical strength of the overburden were tested to determine their influence on the development of stratigraphic and structural relationships in the emerging salt and sediment structures. These simulations show that the advance of salt is driven by gravitational instability and sediment loading. Salt advance is greatest with high basal slopes, thick salt, weak sediments, and high sediment progradation rates. The rate of salt advance determines the angle of a subsalt sediment ramp, which influences the final geometry of the system. High angle ramps form with slow salt front advance rates and tend to form counterregional sediment geometries, while low angle ramps form with rapid salt front advance and tend to produce roho geometries.

Acknowledgements

I would like to acknowledge the tireless work of my thesis advisor, Juli Morgan, without whom this project could never have been completed. I am especially indebted to her efforts to modify the DEM code to produce whatever parameters or tools I thought might aid in the modeling efforts presented in this thesis. I would also like to thank the other members of my thesis committee, John Anderson and Brandon Dugan, for their insights into various aspects of this project.

Juli and I are also indebted to ExxonMobil for their financial support, as well as, the many insightful conversations about the progress of these efforts with members of the Upstream Research Company. I would also like to specifically thank Gary Gray of ExxonMobil for the field trip to La Popa Basin, Mexico which helped to jumpstart this project.

I am also indebted to the financial support of my parents, Harry and Patti Maxwell, as well as my in-laws, Dan and Rebecca Mehr, who kept food on our table and clothes on our children. I also thank my mother-in-law, Deborah Mehr, for her love and support even while battling cancer. Sadly, she was not able to see this work completed.

Finally, I would like to thank my wife, Melanie, for her patience, support, and advice as I worked on this project.

Table of Contents

Table of Figures

Appendices

Tables

Appendices

INTRODUCTION

The areas around salt bodies have long been known to be excellent exploration areas for oil and gas reservoirs. Salt movement causes the flanking and overlying sediment layers to fracture and fold, creating both stratigraphic and structural traps for hydrocarbons (Halbouty, 1979). Seismic surveys show complicated stratal geometries and deformation structures in salt basins around the world, such as: the Gulf of Mexico (Wu et al., 1990), the North Sea (Koyi and Petersen, 1993; Remmelts, 1995), offshore Brazil (Demercian et al., 1993; Cobbold et al., 1995; Mohriak et al., 1995), and offshore West Africa (Lundin, 1992; Duval et al., 1992; Cramez and Jackson, 2000). Less common surface exposures of salt tectonic systems, such as: La Popa Basin, Mexico (Laudon, 1984; Giles and Lawton, 1999; Rowan et al, 2003); the Flinders Range, Australia (Rowan and Vendeville, 2006); and Central Iran (Talbot and Aftabi, 2004), also reveal spectacular upturned beds, unconformable relationships, and growth strata indicative of syn-kinematic deposition (i.e., halokinetic sequences, Giles and Lawton, 2002). However, observations of natural salt systems provide only snapshots of their evolution, commonly spatially limited, and offer little constraint on the physical and mechanical properties that controlled their growth. The focus of this paper is to explore how the underlying mechanisms of salt movement (sediment and tectonic loading of weak buoyant salt) affect the development of emergent salt sheets and the corresponding deformation to the overlying and flanking sediment layers. The Discrete Element Method (DEM) is used to explore these mechanisms.

A great deal of work has been done previously to understand the movement of salt within the earth. A large part of this work consists of numerical and physical models.

Numerical modeling has been carried out using Finite Element Methods (FEM) treating both the salt and the overlying sediment as viscous materials. These models can track the progressive growth of salt structures and the associated stress fields (Last, 1988; van Keken et al, 1993; Fletcher et al., 1995; Schultz-Ela, 2003; Gemmer et al., 2004, 2005), but commonly rely on simplified rheologies, especially for brittle sediments. Physical modeling has been carried out primarily using silicone gel to represent salt as a viscous material and sand to represent the overlying sediments (Vendeville and Jackson, 1992a, 1992b; Cotton and Koyi, 2000; Fort et al., 2004; Talbot and Aftabi, 2004; Rowan and Vendeville, 2006; Brun and Mauduit, 2009). Physical models have reproduced realistic geometries in three dimensions (3-D), but are difficult to scale correctly to natural systems (Hubbert, 1937; Cotton and Koyi, 2000). Also, physical models are difficult to probe to quantify physical and mechanical properties associated with deformation. The challenges posed by previous modeling efforts encourage us to explore a new application of DEM to study salt basin evolution. DEM, designed by Cundall and Strack (1979), can reproduce realistic rheologies for sediments layers around salt bodies (scaled appropriately to natural systems) and approximate rheologies for salt as a granular assemblage. DEM also offers the ability to monitor and probe the progressive structural and mechanical evolution of the system. This paper represents a pioneering study to test the applicability of DEM to this problem.

BACKGROUND

Salt

Salt deposits are found throughout the world both on passive margins, continental interiors, and orogenic belts (Hudec and Jackson, 2007). Salt, and other evaporites, are deposited in basins where evaporation rates exceed influx of water. This commonly occurs during continental rifting when rift basins are filled by rising sea levels. When sea level falls or plate movement closes ocean basins, the landlocked seas evaporate and deposit thick evaporite layers (Hsü et al., 1973, 1977). These layers are subsequently buried, when sea level rises again, by continental margin sediments (distal muds and prograding delta sands). Loading of the salt layers causes pressure gradients to develop, providing a driving force for salt flow (Jackson and Talbot, 1986; Last, 1988; Ge et al., 1997; Gemmer et al., 2004, 2005). The flow of salt can be modeled as viscous because its yield strength is negligible on geologic timescales (Jackson and Talbot, 1986). At strain rates between 10^{-12} and 10^{-14} s^{-1} and temperatures from 50 ° to 150 ° C, rocksalt has a viscosity of 10^{17} to 10^{18} Pa·s (Jackson and Talbot, 1986; Carter et al, 1993).

Allochthonous Salt Sheets

Field examples, numerical models, and geometric restorations of continental margins show that salt nappes and salt diapers form allochthonous salt sheets when they reach the seafloor and begin to flow downslope. (Fletcher et al., 1995; Cotton and Koyi, 2000; Talbot and Aftabi, 2004; Hudec and Jackson, 2007). Salt will either flow downslope as new salt is driven up the feeder due to continued loading of the autochthonous salt layer (extrusive advance), or it will move forward due to loading of sediment on the

allochthonous sheet itself (open-toed and thrust advance)(Hudec and Jackson, 2006). It has been hypothesized that during the process of open-toe advance, two end-member patterns of roof deformation can form: roho systems (Diegel et al., 1995; Schuster, 1995; Rowan et al., 1999), and counterregional systems (Schuster, 1995; Rowan et al., 1999) (Figure 1).

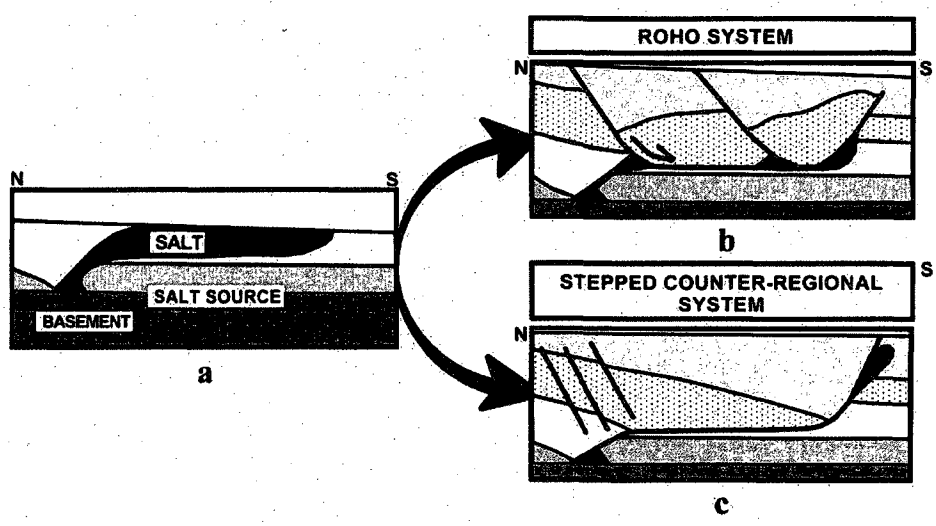

Figure 1: Cartoon showing (a) initial salt geometry, and proposed geometries for (b) roho salt systems and (c) stepped counterregional salt systems. Roho systems are favored by weak sedimentary roofs and highly extensional environments while counterregional systems are favored by complete salt expulsion (Schuster, 1995).

Sediment subsidence into salt is driven by the negative buoyancy of mature sediment basins. After sediment has accumulated thicknesses of 1.5-2.0 km, the salt/sediment density contrast is great enough to allow the basins to subside (Velde, 1996). It has been proposed that roho and counterregional systems are driven by the subsidence of these mature sediments and the associated deformation (faulting) of the basins involved (Schuster, 1995; Hudec and Jackson, 2006). Hudec and Jackson (2006) further proposed that roho systems should be favored by areas of gravitational instability (steep slopes),

low sedimentation rates (thin, weak roof), and long emergent salt sheets (space for extension). This extension is accommodated along basinward dipping listric normal faults that sole into the back of the salt sheet (Schuster, 1995; Hudec and Jackson, 2006). In cross section, this subsidence leaves triangular salt diapirs trapped in between subsiding blocks (Rowan et al., 1999) (Figure 1). Counterregional systems are characterized by complete expulsion of the allochthonous salt sheet. The resultant geometry is an apparent landward dipping normal fault (Schuster, 1995; Rowan et al., 1999; Hudec and Jackson, 2006). These systems are hypothesized to form under conditions unfavorable to overburden extension (Hudec and Jackson, 2006).

The factors that control the different roof deformation styles above advancing salt sheets have been investigated through geometric restorations using seismic and well data (Diegel et al., 1995; Schuster, 1995; Hudec and Jackson, 2006), leading to the hypotheses reviewed above. But to date, the physical and mechanical controls that govern these modes of deformation have not been explored. An understanding of how differential loading conditions change deformation patterns in the overlying and flanking sediments during salt sheet advance will aid researchers in modeling the growth histories of known salt structures and in identifying and evaluating possible hydrocarbon reservoirs in their flanking sediment layers.

METHODOLOGY

Discrete Element Method

The basis of the Discrete Element Method (DEM) has been outlined most completely by Cundall and Strack (1979), and summarized by Morgan and McGovern (2005). The

method applies Newton's second law of motion to particles with elastico-frictional contacts (Figure 2). The method first solves for forces imposed on the surfaces of each particle by neighboring particles or boundaries and then calculates a displacement based on the acceleration caused by the sum of these forces. Particles, therefore, transmit forces to other neighboring particles. Failure of these bridging contacts by interparticle slip causes discrete structures to develop within the material, such as faults and fractures.

Particle contact forces are calculated during each timestep of the model run. For example, repulsive normal forces (f_n) on particle boundaries are calculated as:

$$f_n = k_n \delta_n \tag{1}$$

where k_n represents the normal interparticle stiffness and δ_n denotes the amount of overlap between particles (Morgan and McGovern, 2005). Overlap is calculated as the difference between the sum of the radii and the center to center distance of two particles. A positive value indicates that the particles are in contact. Shear forces resulting from particle interaction are calculated using a similar equation:

$$f_s = k_s \delta_s \tag{2}$$

where k_s dictates the shear stiffness between the particles (Morgan and McGovern, 2005). Although stated very simply here, both the k_s and k_n values are nonlinear quantities proportional to the contact area of overlapping particles following the Hertz-Mindlin theory (Johnson, 1985). Shear forces at interparticle contacts are also limited by the applied value of interparticle friction (μ_p):

$$f_s^{max} = \mu_p f_n \tag{3}$$

When the maximum shear force is exceeded (f_s^{max}), slip occurs, allowing particles to move past each other. It is this mechanism that allows discrete structures, such as faults, to emerge.

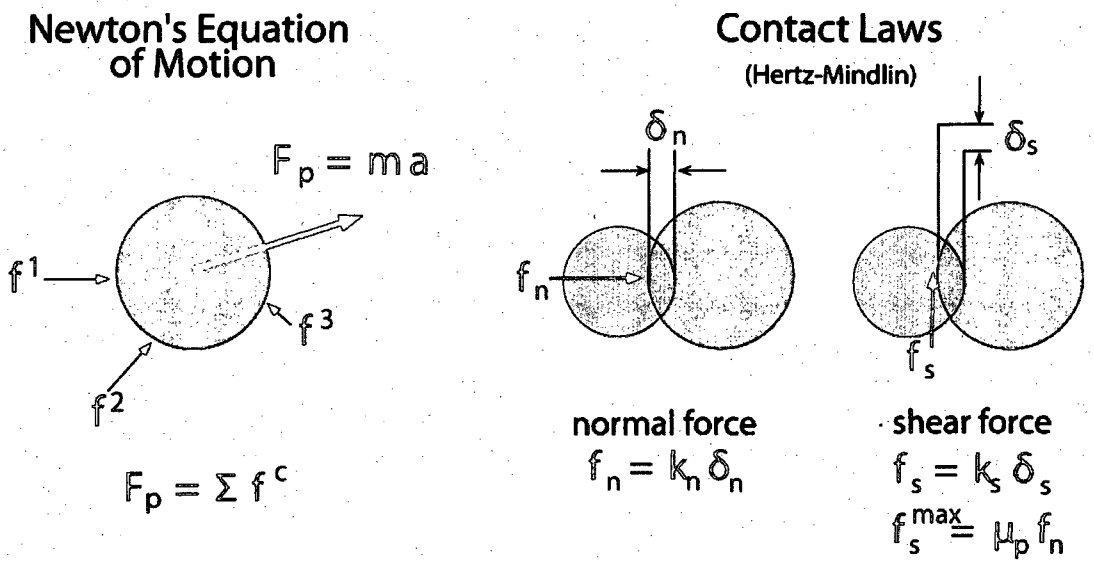

Figure 2: Schematic representation of particle interactions calculated for each time step throughout DEM simulations. Contact normal and shear forces are imparted by corresponding relative particle displacements, scaled by the appropriate contact stiffness. Stiffness is actually a non-linear term calculated from Hertz-Mindlin theory of contact (e.g., Morgan and Boettcher, 1999). Contact forces are summed during each timestep to obtain the out-of-balance particle centroid force that drives particle motion.

Particle contacts can also be bonded together, imparting cohesion to the material assemblage. Bonding is implemented in this study by introducing an elastic beam that can support tensile and shear forces below some predefined limits, defined as tensile strength and cohesion, respectively (Morgan, in prep). This beam does not support any

moment, and therefore does not resist particle rotation. The bond-induced forces are calculated as:

$$b_n = E\,\delta_n * A \tag{4a}$$

$$b_s = G\,\delta_s * A \tag{4b}$$

where b_n and b_s are the tensile and shear force, respectively, and E and G are the Young's modulus and shear modulus of the bond, respectively. A is the cross-sectional area of the elastic bond, assumed to be a circle with a radius equal to that of the smallest particle in contact. Bond tensile forces are generated when particles are not in contact, i.e., $\delta_n < 0.0$, and are limited by the tensile strength, T, scaled by bond area, i.e., T*A. Bond shear forces can be generated in both tension and compression. In compression, bond shear forces, b_s are limited by equation (3) with an additive cohesive strength, C, scaled by area, i.e., C*A. In tension, shear forces are limited by the relationship C*A (b_n – T*A), assuring that cohesive strengths are zero at tensile failure, and equal to C when contact separation is zero. Thus, the properties and strength of each bond are defined by its elastic moduli, E and G, and its tensile and cohesive strengths, T and C, respectively.

For each timestep, the net force and moments are calculated for each particle by summing the components of all contact forces acting on a particle. These quantities are used to determine net linear and angular accelerations from which particle displacements and rotations are determined. The net force (F_p) and net moment (M_p) are calculated by:

$$F_p = m_p x''_p \tag{5a}$$

$$M_p = I_p \theta''_p \tag{5b}$$

where m_p is the particle mass, x''_p is the net linear acceleration, I_p is the moment of inertia, and θ''_p is the net angular acceleration (Morgan and McGovern, 2005). During each

timestep, the motion of each particle causes new interactions with adjacent particles, requiring an update of the contact forces. Damping of particle motions removes energy from the system, serving as a proxy for inelastic deformation in real materials (Cundall and Strack, 1979).

Using the equations described above, the simulation proceeds through the alternating calculations of contact forces, particle centroid forces, moments, and displacements for each particle during every timestep. By tracking individual particle displacements the model is able to capture discrete discontinuities in the assemblage, such as faults and fractures, and follow these structures as they evolve.

DEM Advantages and Challenges

DEM simulations offer certain advantages when modeling heterogeneous systems; in particular, allowing us to quantify discrete forces and displacements acting on individual particles. The discrete nature of DEM simulations provides valuable insight into the discontinuous behavior of systems that can be approximated as granular. It is also possible to derive continuum properties by averaging discrete quantities over a finite volume (e.g., Oda and Iwashita, 1999). For example, stress tensors, strain tensors, and porosity can be calculated across the 2-D or 3-D domain (Satake, 1999), providing measures easily related to bulk properties derived from the field or the laboratory. Some of the calculation methods are outlined by Morgan and Boettcher (1999) and Morgan and McGovern (2005a and 2005b).

One other important aspect of this approach, and a major advantage that it provides over other numerical modeling methods, is that the rheologic behavior of the material is a

product of the aggregate particles' physical interactions, and can evolve through time. This is in contrast to models using the Finite Element Method (FEM), which have been used in the past to model salt diapirism and salt sheets (Last, 1988; van Keken et al, 1993; Fletcher et al., 1995; Schultz-Ela, 2003; Gemmer et al., 2004, 2005). In these cases, the rheology is prescribed. Some FEM models have also treated the overlying strata as viscous, which precludes true coulomb brittle deformation that must occur in these sediments as layers bend, fold, and fault. By using the discrete element method, we are better able to approximate the overall rheology of the overriding and flanking sediment layers of advancing salt sheets.

In this way, DEM resembles physical sandbox models that explore emergent sediment deformation. Numerical modeling using DEM, however, has key advantages over the physical models used in many salt sheet studies that simulate brittle sediment deformation. Often, a material with the necessary physical properties is commercially unavailable, expensive, or difficult to use (Appendix D). Also, the forces in physical models can be somewhat unrealistic because the force of gravity cannot be easily scaled with the model. DEM allows us to input appropriate physical properties of the materials and the inferred boundary forces that act on the system.

However, there are some challenges associated with DEM models, such as, finite particle size and the rheologic limitations of the particle assemblage. Particles represent physical grain aggregates in real systems (e.g., fractured blocks). However, because the introduction of a large number of particles is computationally intensive, the imaging of very small-scale deformation in large-scale simulations becomes difficult. The rheologic limitations, in particular, the granular assumption for salt, which is understood to behave

viscously in nature, must also be overcome. The granular nature of the DEM approach specifies frictional interactions between particles, rather than viscous creep. However, we can pick a set of parameters that most effectively captures the overall material behavior observed in natural salt. In order to test the rheology of both the salt and sediment proxies used in these experiments, suites of calibration experiments were carried out and the results are reviewed below.

EXPERIMENTAL DESIGN AND MATERIAL PROPERTIES

Model Set-up

Simulations were run using a 70 km long and 30 km tall numerical domain (Figure 3). Vertical walls of particles were placed at the lateral edges of the domain and a horizontal wall was placed along the base of the domain.

The salt sheet is deposited by randomly generating salt particles (red) above the left 29 km of the domain and allowing them to settle under gravity (Figure 3). Sediment particles (66 particles/km or approximately 0.8 km^2 per km) are then deposited in two batches: one on the back of the salt sheet representing sediment layers deposited on the continental slope (above the salt), and the other in front of the salt (to the right) to simulate abyssal plain distal mud deposition. Under the differential load of the continental slope sediments, the salt particles flow to the right onto the newly deposited abyssal plain sediments. Once the initial settling of particles is completed, a planar surface is imposed by "eroding" excess particles above a prescribed height in both the "continental slope" and the "abyssal plain" sediment layers. Salt particles and pre-existing sediments are not eroded. The system is then allowed to continue deforming

under the new load. After a predetermined amount of time, the sediment particles are bonded together to simulate diagenetic cementation with time and burial. New sediments are then deposited on top of these cemented particles and the process is repeated following the same pattern (settling, erosion, deformation, bonding) until 9 layers have been deposited. Sediment particles are colored (green, white, and yellow) to aid in distinguishing layering and deformation.

Particle properties were chosen to best capture natural Earth materials (Table 1). Salt and sediment particles assemblages consisted of two particle radii dimensions (50 and 75 m) with equal abundances of each particle size. Salt particles were assigned zero surface contact friction with all particles in the domain, thereby, offering no resistance to interparticle slip. However, the granular packing of the salt results in an internal friction coefficient of ~0.1 (Morgan, 2004) which is consistent with the derived strength of salt in laboratory studies (Carter et al., 1993). Salt particles were also assigned zero friction contacts with the base and walls of the domain. Sediment particles were assigned moderate friction coefficients of 0.3 for interactions among themselves and with the wall particles. Sediment particles also were bonded to each other and to the walls upon settling, in order to resist granular flow. Using densities of 2500 kg/m^3 for sediment layers, 2200 kg/m^3 for salt, and 1000 kg/m^3 for water, the buoyant density of salt and sediment layers in a typical submarine environment was calculated by subtracting the density of water from the density of the layer. To approximate this average density in our models, salt and sediment particles were set at 1200 kg/m^3 and 1500 kg/m^3, respectively. No pore pressure build-up effects were considered. Simulations were run using the Intel Xeon computing cluster (SUG@R) at Rice University.

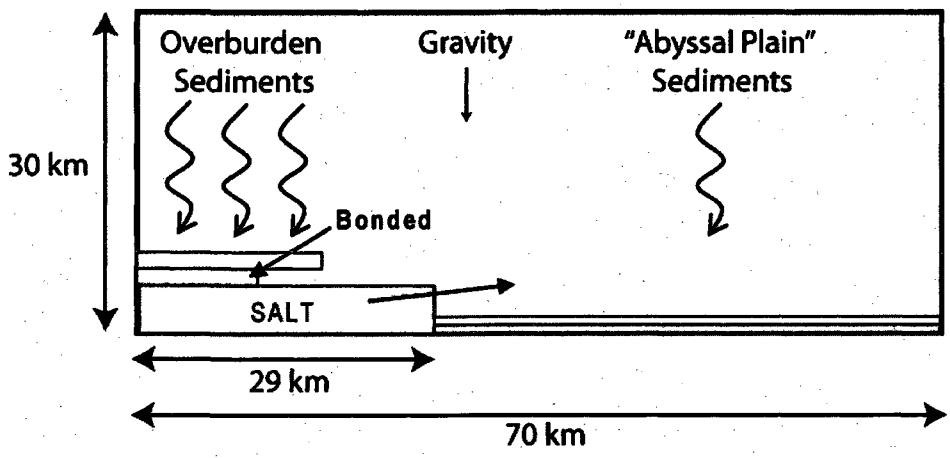

Figure 3: Experimental set-up for allochthonous salt-sheet simulations. Salt is deposited in left 29 km of a 70 km wide domain bounded by fixed walls. Sediment layers are added in batches (shown by green and yellow layers), and in two separate areas: one on the back of the salt sheet to build the sediment overburden and the other in front of the salt sheet representing abyssal plain deposition. Sediment particle batches in both areas are bonded to impart cohesion after settling, but before the next batch is created. The differential load causes salt to flow up and over the abyssal plain sediments. Salt evacuation and ongoing sediment deposition causes deformation of the overburden. The basal slope is adjusted by changing the direction of the gravitational acceleration vector.

Table 1: Particle properties used for all suites of experiments.

Particle type	Radii (m)	Density (g/cm^3)	Coef. of Friction	Particle Stiffness
Salt	75, 50	1200	0.00	8.00E+08
Sediment	75, 50	1500	0.30	3.00E+09
Wall	125	1500	0.30	3.00E+09

Material Calibration

Salt Rheology

Because rocksalt is not a granular material, it is necessary to determine how well its expected behaviors can be reproduced using our "salt" particles. To assess the dynamic properties (in particular, viscosity) of this salt analog used in our models, salt particles were placed in numerical shear boxes under different confining pressures. Each box was sheared by moving the top and bottom walls of the box to induce right lateral shear (Figure 4). A variety of wall velocities were used to vary strain rate at each of the

confining pressures. Stresses were monitored and recorded. Overall shear stress was obtained by summing the components of force acting on each particle and dividing by volume over which they were summed. The shear stress and strain rate were then plotted for comparison (Figure 5). The results show that at strain rates of 10^{-1} to 10^{3} s^{-1} the salt particles have an overall viscosity of 10^{8} to 10^{10} Pa·s. The viscosity increases with depth. Separate simulations demonstrate that this viscosity is similar at lower strain rates (Appendix B).

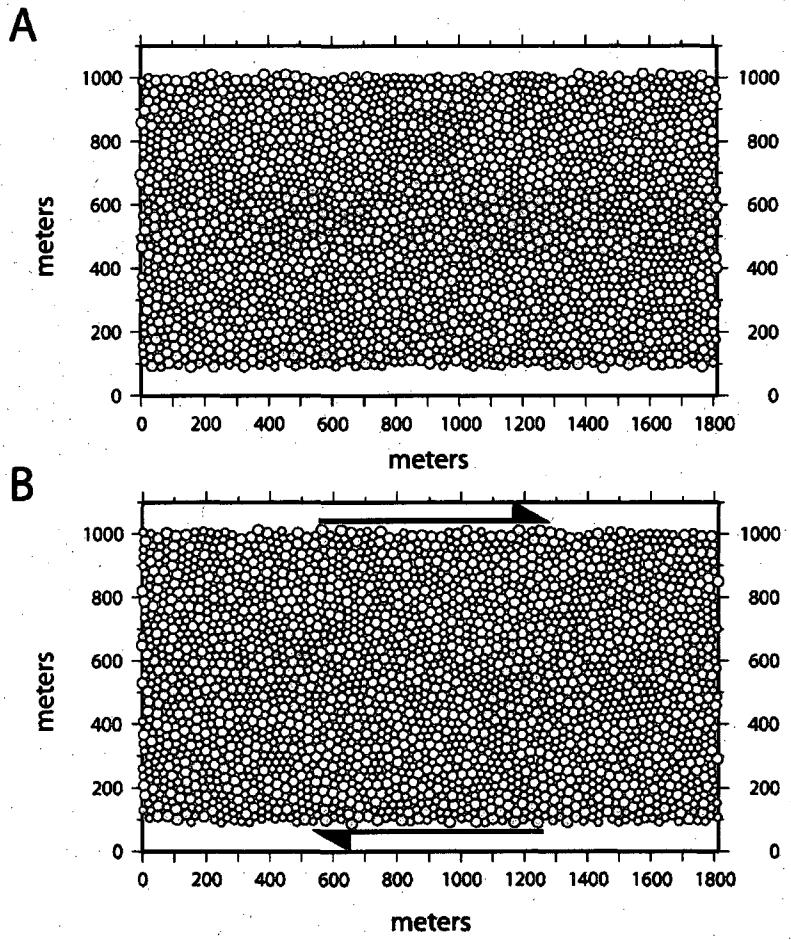

Figure 4: Numerical shear box to simulate salt rheology. Boundary walls (gray) are displaced laterally to induce shear into the low density, weak numerical salt. (A) Initial configuration; (B) 180% strain. The top wall is moved to the right and the bottom to the left. Colored particles are present as marker beds but do not represent a change of particle type. Elongation and tilt of vertical marker shows overall homogeneous deformation.

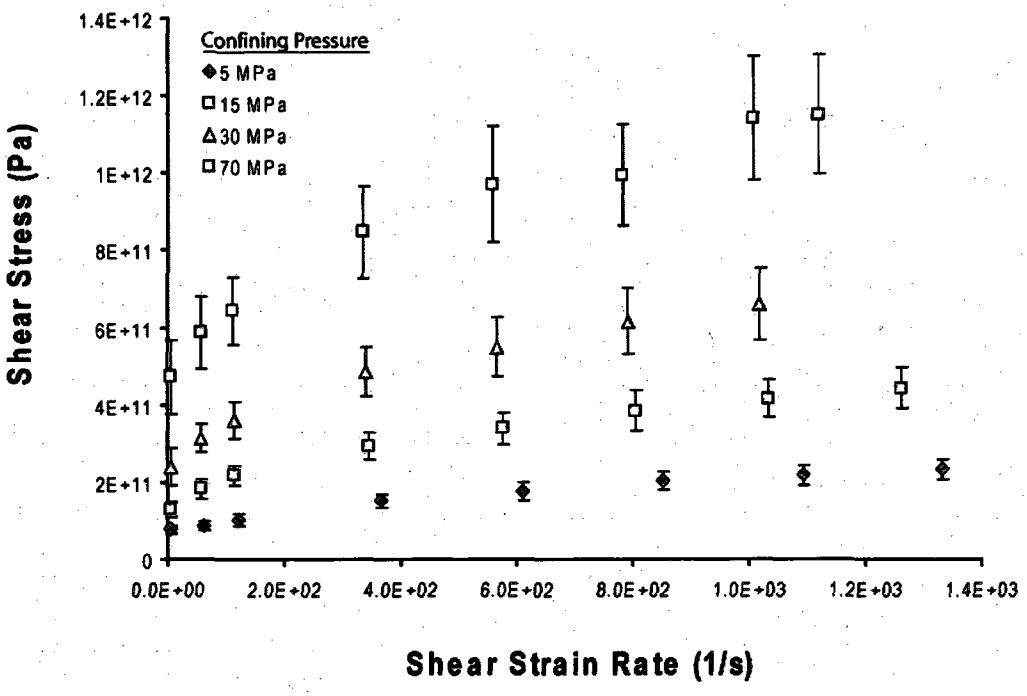

Figure 5: Shear stress vs. shear strain rate for different confining pressures. The slope of the best fit line to data points in each suite represents the viscosity of the material at those conditions. Viscosity generally decreases with lower normal stresses and higher strain rates. Error bars are black and represent one standard deviation for shear stress.

This "granular viscosity" is much less than the observed viscosities of natural salt (10^{17}-10^{18} Pa·s; Jackson and Talbot, 1986; Carter et al, 1993). Additional tests (Appendix B) show that the viscosity could be increased by increasing the friction of the particle surfaces. However, this also increases the overall strength and causes greater slip localization, which is not consistent with rocksalt behavior under natural conditions. Particle contacts with no friction result in distributed deformation (Figure 4) which is more characteristic of viscous flow. We also examined the effect of the elastic shear stiffness of the particles on the overall viscosity of the salt assemblage (Appendix B). The results show that increasing the stiffness results in an increase in apparent viscosity because stiffer particles are less able to squeeze past each other. However, high stiffness

also reduces the ability of the granular material to creep under low stress. Therefore, we choose to maintain low particle stiffnesses in order to capture the most representative granular-viscous behavior.

Although our numerical salt exhibits an anomalously low viscosity, we can compensate for this discrepancy by scaling time in our models. Because sedimentation provides a driving force for the evacuation of salt, sedimentation rate is directly related to the shear strain rate of the salt layer. By dramatically increasing the sedimentation rate of our models, a favorable ratio of simulated strain rate to natural strain rate is obtained, such that, the range of shear stresses acting on the salt sheet in our simulations is similar to the range of shear stresses in natural systems at much lower strain rates (Figure 6). As a result, our simulations occur over a much shorter time span than natural examples. However, we argue that the overall structures that develop in our system should be representative, especially in sedimentary rocks, which arguably have very little time dependence in their rheology (Jaeger and Cook, 1969).

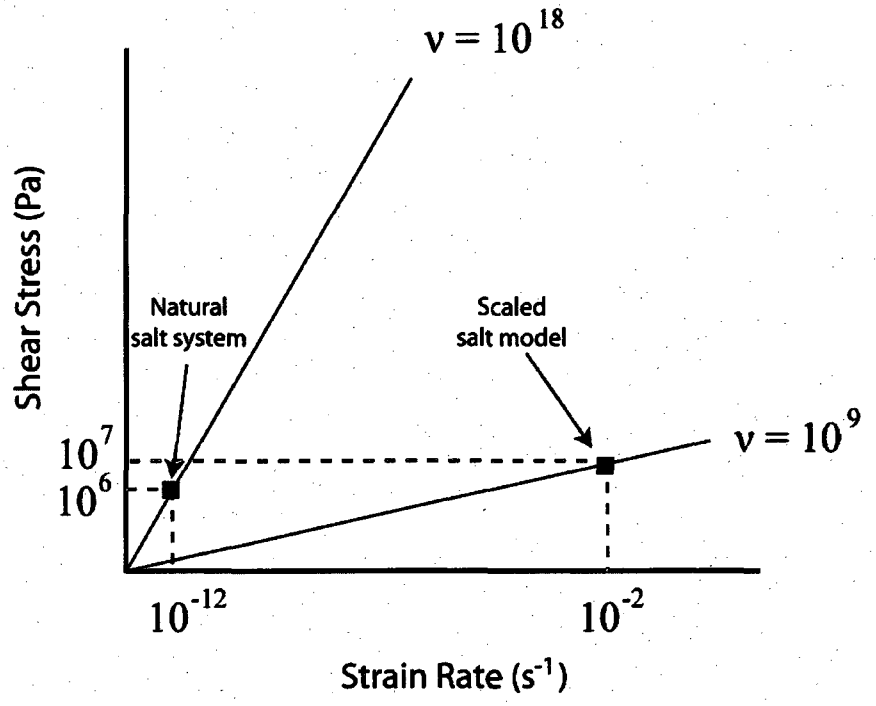

Figure 6: Schematic graph (not to scale) showing the relationship of shear stress to strain rate for natural salt (viscosity of 10^{18} Pa·s) and the granular salt used in these models (viscosity of 10^{9} Pa·s). Black squares represent the locations of natural and simulated examples. Similar shear stresses are experienced in both cases.

Sediment Strength

Sediment cohesive strength will also play an important role in determining the style of deformation in the overriding sediment layers during salt sheet advance. Cohesive strengths for sediments above salt detachments likely span a large range because of the wide variation of the micro-properties (eg., grain size, porosity, cementation, distribution of micro-cracks) in these rocks (Karig and Morgan, 1994; Saffer et al., 2003; Yun et al., 2006). The behavior of our granular material is also dependent on a wide range of micro-properties (e.g., particle size, particle elastic moduli, interparticle friction, and bond strength), which will control the bulk behavior (i.e., macro-properties), such as, cohesive strength, compressive strength, and tensile strength (Potyondy, 2007). Interparticle bond strengths at particle contacts are especially important in affecting the overall bulk

strength and behavior of the particle assemblage. This relationship must be determined by calibration tests.

Our calibration of bulk rock properties to grain-scale and bond-scale properties is still in an early stage, but has drawn from the work of previous studies. Potyondy and Cundall (2004) found that bonded DEM simulations are able to reasonably reproduce rock behaviors, such as elasticity, fracturing, acoustic emission, damage accumulation producing material anisotropy, hysteresis, dilation, post-peak softening and strength increase with confinement. In additional studies by Cho et al. (2007), it was determined that using "clumped particle" models improved the ability of DEM simulations to recreate reasonable rock properties for granites over a variety of stress paths. However, due to the scale of our simulations, the clump particle method is not reasonable here. Furthermore, we are most interested in low strength materials that are well represented by individual bonded particles, as described below.

In order to relate particle-scale bond properties to bulk strength we carried out a series of bi-axial compression experiments on bonded particle assemblages. Sediment particles were consolidated uniaxially in a numerical compression box by moving the horizontal walls inward (Figure 7). The assemblage was fixed, and then subjected to a confining pressure. The horizontal boundary particles were assigned additive inward directed centroid forces to maintain the desired confining pressure on the horizontal boundary (simulating a deformable membrane). The left and right side walls (defining end plates to induce differential stress) were then moved inward until the assemblage failed. Stresses were monitored throughout the test in order to record both the peak and the residual strengths.

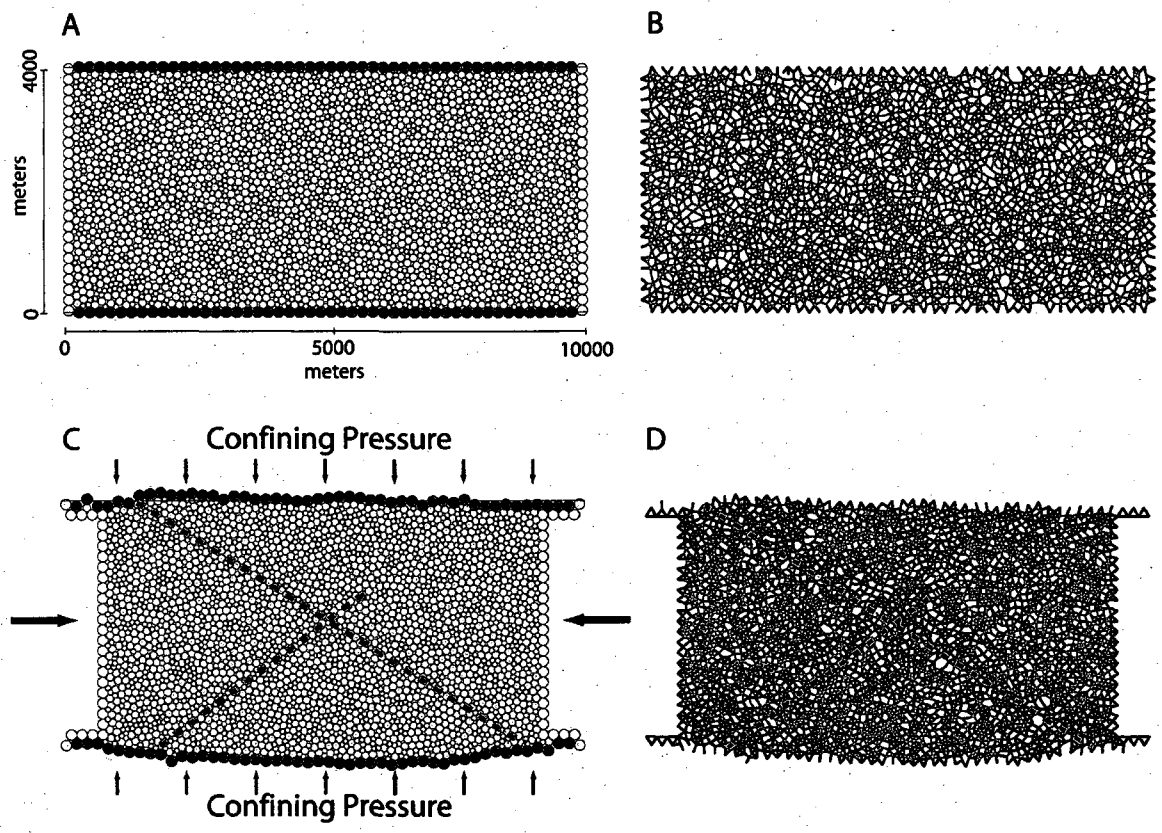

Figure 7: Representative sample configurations for uniaxial and bi-axial numerical calibration experiments. A) Particle assemblage following uniaxial consolidation to 10 MPa, imposed by moving horizontal black walls inward. Particle contacts are bonded after they have been consolidated by the inward push of the horizontal walls. B) Distribution of contact forces for configuration in A. Lines connect centers of particle pairs that support contact forces, and line width is scaled to force magnitude. Green denotes bonded contacts in compression; black denotes unbonded contacts in compression; red denotes bonded contacts in tension. C) Particle assemblage after 14 % axial strain imposed by moving vertical wall of white particles inward (as shown by black arrows). Bounding black particles act as a deformable membrane that maintains the desired inward directed confining pressure (40 MPa in this case). Dotted red lines show the approximate location of shear fractures that form. D) Distribution of contact forces for configuration in C. Same color scheme as in B. Note concentration of black contacts near shear fractures.

As an additional test of material properties, we selected bond strengths that represent a reasonable range of natural sediment-rock strengths, and examined their effects on deformation and resultant structure. A suite of salt sheet models was run with different shear and normal bond strengths (LN06A-LN06F, Table 2, see Figure 15), to determine

which strengths best reproduced observed faulting in offshore supra-salt areas. Ideally, the simulated sediments should be weak enough to localize deformation onto discrete high-angle normal faults, but not so weak that the bonded assemblage crumbles and deforms by distributed deformation. Tensile bond strengths of 10 MPa and cohesive bond strengths of 20 MPa represent the lowest possible strength configuration that was able to maintain realistic faulting (thin zones of deformation) without crumbling. Samples with these bond parameters, as well as, the other bond parameters used in this salt sheet model suite (LN06A-LN06F, Figure 15) were also studied using the compressive test described above (Appendix C).

Tested samples were consolidated and bonded under a range of consolidation stresses. These assemblages were then subjected to biaxial compression at varying confining pressures designed to match the lithostatic pressures (0-100 MPa) experienced by sediment layers during a typical model run (0-6 km burial, see Figure 9). A greater range of tests were run on samples with tensile bond strengths of 10 MPa and cohesive bond strengths of 20 MPa because this bond strength is used for the majority of our salt sheet simulations (Figure 8, Figure C-1). Furthermore, samples consolidated at 5 MPa and 10 MPa, with these bond strengths, were chosen as representative of average vertical stress states for newly bonded sediment in our models. Results from samples under these conditions show pressure dependent shear strengths up to 90 MPa for confining pressures of 100 MPa (Figure 8). By using the mean stress and half of the differential stress as an approximation for the failure envelope of the bonded particle assemblage an overall cohesive strength from 2 MPa to 3 MPa was determined. This also yields an internal friction angle between 15 ° and 16 °. Previous research carried out on sediment cores

from accretionary prisms shows that this cohesion is close to natural examples with cohesive strengths below 5 MPa (Karig and Morgan, 1994). The angle of internal friction is also within an acceptable range for real earth examples and submarine rocks (Byerlee, 1978, Gemmer et al., 2005).

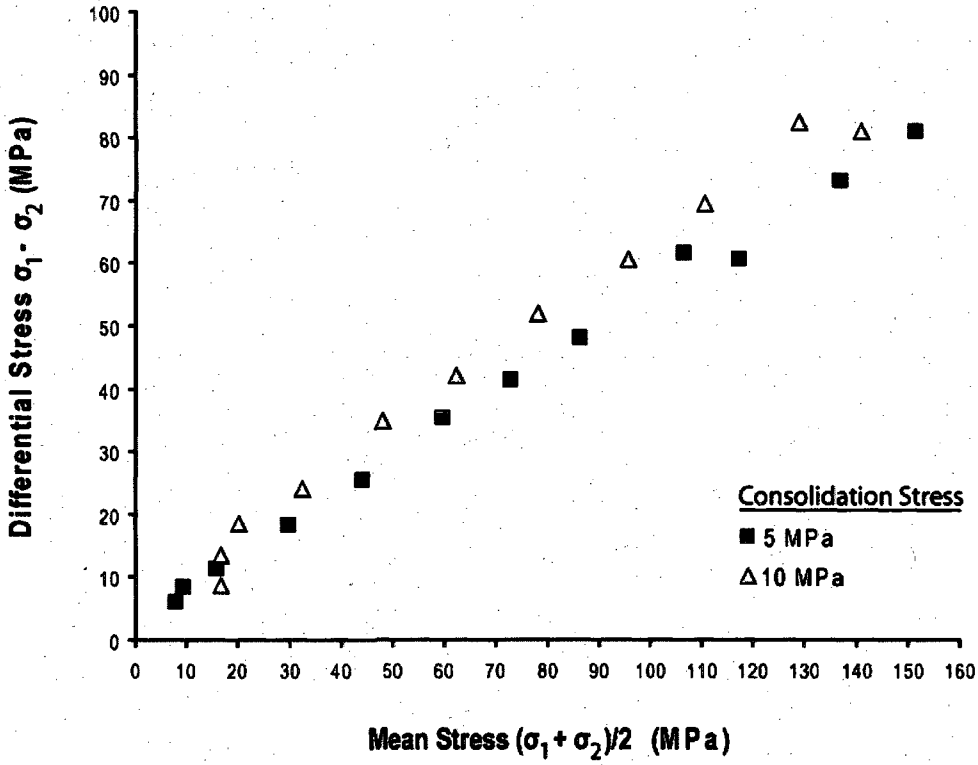

Figure 8: Plot of peak differential stress for biaxial compression experiments carried out at different confining pressures for particle assemblages preconsolidated to 5 MPa and 10MPa.

EXPERIMENTAL RESULTS

Suites of experiments were carried out to test the effects of different loading parameters on the development of sediment and salt structures during allochthonous salt sheet advance. These parameters include: basal slope angle, initial thickness of the salt sheet, sediment thickness, sediment progradation rate, variation in loading time, and mechanical strength of the sediments (Table 2).

Table 2: Suites of experiments and associated properties

Model	Basal Slope (°)	Sediment Aggradation (m)	Initial salt thickness (km)	Progradation rate (km/layer)	Tensile Strength (Pa)	Cohesive Strength (Pa)	Model Run (my)
Sediment Thickness							
LN02A	2.5	125	3	4	1.00E+07	2.00E+07	10.00
LN03B	2.5	250	3	4	1.00E+07	2.00E+07	10.00
LN02C	2.5	375	3	4	1.00E+07	2.00E+07	10.00
Time							
LN03B	2.5	250	3	4	1.00E+07	2.00E+07	10.00
LN03BA	2.5	250	3	4	1.00E+07	2.00E+07	3.33
Progradation Rate							
LN05A	2.5	250	3	2	1.00E+07	2.00E+07	10.00
LN03B	2.5	250	3	4	1.00E+07	2.00E+07	10.00
LN05C	2.5	250	3	6	1.00E+07	2.00E+07	10.00
Basal Slope							
LN03A	0	250	3	4	1.00E+07	2.00E+07	10.00
LN03B	2.5	250	3	4	1.00E+07	2.00E+07	10.00
LN03C	5	250	3	4	1.00E+07	2.00E+07	10.00
Initial Salt Thickness							
LN04A	2.5	250	1.5	4	1.00E+07	2.00E+07	10.00
LN03B	2.5	250	3	4	1.00E+07	2.00E+07	10.00
LN04C	2.5	250	4.5	4	1.00E+07	2.00E+07	10.00
Sediment Strength							
LN06A	2.5	250	3	4	1.00E+07	2.00E+07	10.00
LN06B	2.5	250	3	4	2.00E+07	4.00E+07	10.00
LN06C	2.5	250	3	4	3.00E+07	6.00E+07	10.00
LN06D	2.5	250	3	4	5.00E+06	1.00E+07	10.00
LN06E	2.5	250	3	4	0.00E+00	0.00E+00	10.00
LN06F	2.5	250	3	4	7.50E+06	1.50E+07	10.00

In nature, a variety of processes can control these parameters. High slopes can form when ocean basins thermally subside or when tectonic uplift raises continents (Rowan et al., 2004). They can also be produced locally on the ocean floor by slumping and landsliding of weak sediment units (McAdoo et al., 2000). Thicker salt deposits form when sedimentary basins open and close allowing periodic flooding and evaporation (e.g. Mediterranean, Hsü et al., 1973, 1977). Sedimentation rates can vary when drainage basins of rivers that discharge sediment into the ocean basin are modified by tectonic uplift or glacial ice sheets (Galloway, 2005). Sedimentation rate can also affect the relative rates of sediment aggradation (sediment thickness) and progradation depending

on the balance of sediment input to accommodation space above the salt sheet. Sediment progradation occurs when there is a greater volume of sediment influx than accommodation space on the continental slope. When sediment supply is equal to the accommodation space above a salt sheet, stratigraphic units aggrade (Anderson et al. 2004). Sea level can also have an effect on the deposition of new sediment units. A fall in sea level could increase the rate of sediment progradation, whereas, a rise in sea level could cause an increase in aggradation, although high sedimentation rates can cause progradation at any time (Vail et al., 1977).

In addition, there are many other parameters that were not considered in this study that could also affect the development of sediment and salt geometries in submarine systems. Possible factors include: basement faulting (North Sea, Koyi and Petersen, 1993), pre-existing salt basin topography (volcanic domes, Brazil, Mohriak et al., 1995), salt with interbedded sediment and volcanic layers (offshore Isreal, Cartwright and Jackson, 2008; and offshore Morocco, Hafid, 2006), and variations in the 3-D geometries of salt sheets and multiple salt feeders (Schuster, 1995). The results of the parameters tested are reviewed below.

Basal Angle

The basal slope angle of each model was adjusted by tilting the direction of gravitational acceleration relative to the base. Three examples are shown in Figure 10, with gravity oriented at 0 °, 2.5 °, and 5 ° for models LN03A, LN03B and LN03C respectively (Table 2). The range of slopes was picked to represent typical slopes on continent margins where allochthonous salt sheets may form on or near the surface

(McAdoo et al., 2000; Anderson et al., 2004). A base sedimentation rate of 250 m/my was chosen using sediment thicknesses from published seismic lines over remnant allochthonous salt sheets (O'Conner and Weimer, 2004). This sedimentation rate represents a minimum aggradation value allowed per layer. Sediment thickness can be greater locally where salt withdrawal creates additional accommodation space. Initial salt thicknesses for all models shown in Figure 10 were 3000 m.

Early deformation in the 0 ° basal slope model (LN03A) was characterized by subsidence of the frontal portion of the sediment overburden as salt was expelled over the abyssal plain sediments (Figure 9). With continuing sedimentation, the overburden developed a series of landward dipping normal faults. Salt diapirs exploited the weakness of these counterregional faults but were unable to rise to the surface because of the thick sediment overburden. Total extension of the sediment overburden, as measured by displacement of the outer edge of the first depositional layer, was 2 km. Salt advanced 11 km during the deposition of the other sediment layers but sediment extension was minimal after the deposition of the first layers. Due to the slow advance of salt, the abyssal plain sediments formed a steep ramp (11 °) which slowed the advanced of salt even further. Progradation of the sediment layers eventually overwhelmed the migration of salt, and effectively stopped salt evacuation.

At a 2.5 ° basal slope, model LN03B exhibited greater extension in the both the sediment layers (14km) and the salt (23 km). Salt flowed downslope extending the sediment overburden to form a series of minibasins during early deformation. Salt rose buoyantly in between the minibasins to form diapirs, which were quickly suppressed by continuing sedimentation. Deformation concentrated within these weak zones to form a

series of basinward dipping listric normal faults. Slip along these faults provided accommodation space at the surface, which was filled by the next sediment layer, forming growth strata (Figure 10b). Continuing sedimentation and progradation caused active faulting to concentrate along the toe of the slope, allowing greater salt expulsion onto the subsalt sediment ramp (8 °, corrected for the tilted gravity vector). This style of overburden deformation resembles the results of other numerical simulations (e.g., Gemmer et al., 2004; Ings et al., 2004).

Model LN03C, with a 5 ° basal slope, was characterized by similar deformation as seen in LN03B (2.5 ° basal slope) but with even greater extension in both the sediment layers (42 km) and the salt (38 km). Extension and salt sheet advance created large amounts of accommodation space on the back of the overburden requiring extra sediments to be added. Sediment basins were carried downslope by the flow of salt instead of driving the salt forward by fault block subsidence. As sedimentation continued, diapirs between minibasins were suppressed as sediments formed growth strata along listric basinward dipping normal faults. The subsalt sediment ramp was 1 ° (corrected for the tilt of gravity).

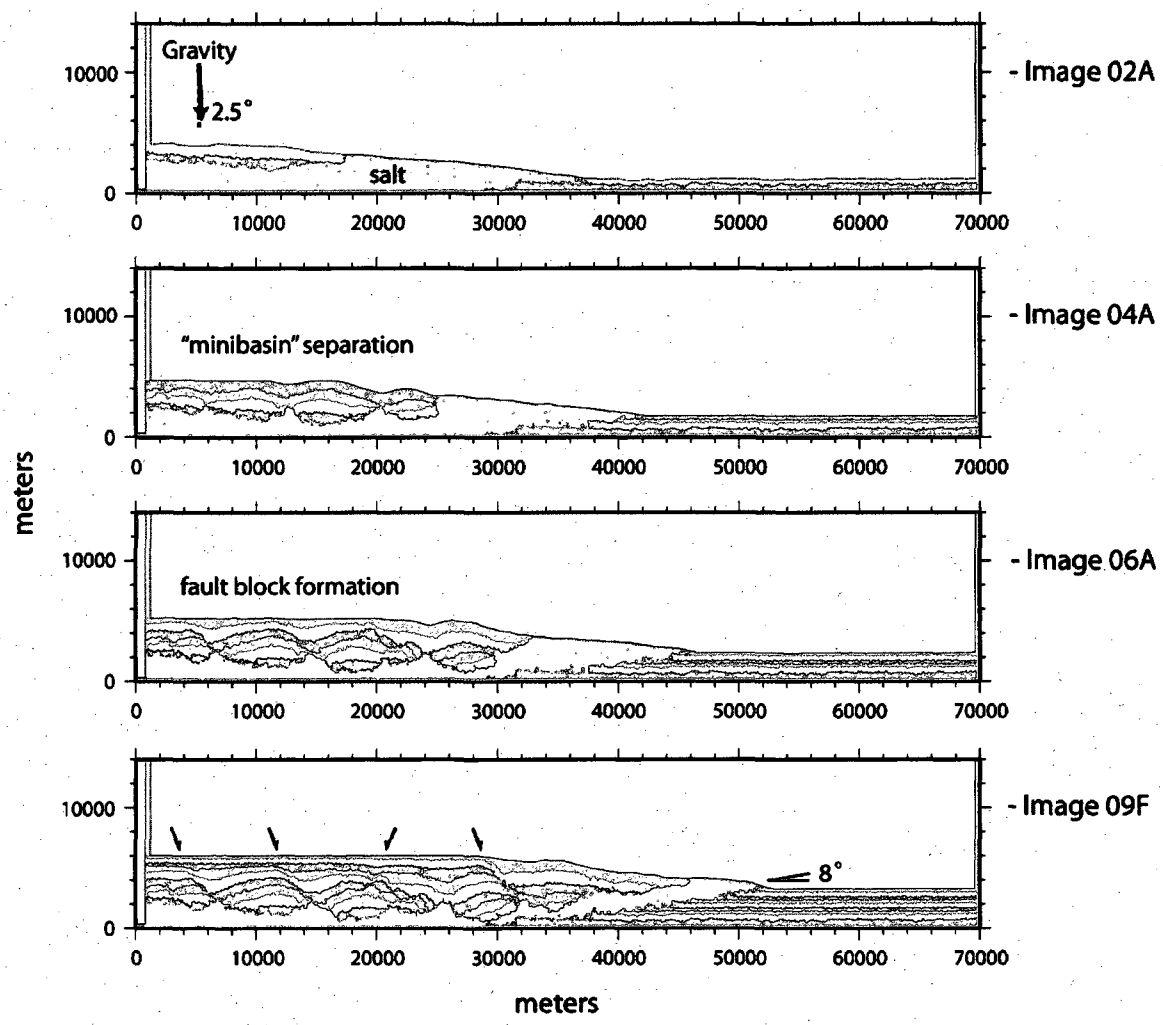

Figure 9: Sequential plots of particle configuration for the progressive growth of base model (LN03B), against which all subsequent models are compared. In image 2A, salt has just begun to advance out over the basin sediments from the load of the two sediment layers. The green layer is bonded; the white layer is not. Faults begin to appear in image 4A and are well developed with growth strata in image 6A. The last image 9A shows the deposition of the last layer in this experiment. Deformation produces roho stratigraphic geometries in the overburden. Fault positions are denoted by black arrows.

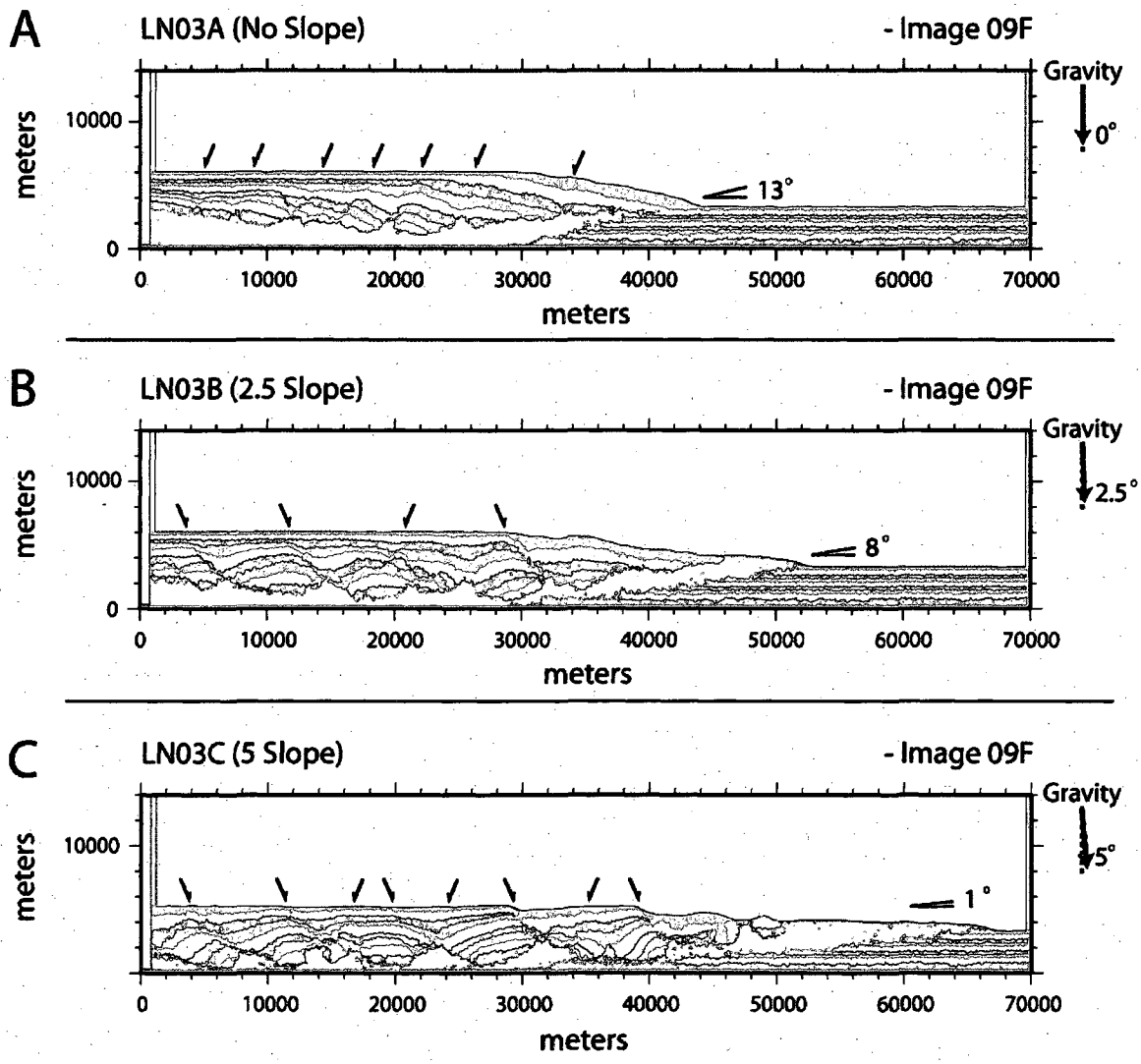

Figure 10: Plots of particle configurations for the suite of models representing variations in basal slope. A) Zero slope. Extension in the overburden is small and contained on small landward dipping faults. Prograding sediment layers prevent salt from completely evacuating. B) 2.5 degree slope. This is the base model against which all subsequent suites of models are compared. A roho stratigraphic geometry forms through deformation on basinward dipping normal faults. C) 5.0 degree slope. Sediment basins are carried downslope by the flow of salt outpacing the progradation of new sediment layers. Deformation in the overburden occurs on basinward dipping faults. Fault positions are denoted by black arrows.

Initial Salt Thickness

A suite of models was run to test the effects of salt thickness on the evolution of the overlying sediment structures. A base salt thickness of 3 km was selected from examples in the literature of salt thicknesses during salt sheet advance (Grando and McClay, 2004). This thickness was chosen to ensure that the salt sheet would be thick enough to flow. Tests of thickness show that a salt thickness of less than 3 particles has limited ability to flow, and the area acts as a salt weld (an area where overburden sediments have subsided onto the subsalt sediment basement, Rowan et al., 2004). Comparison salt thicknesses of 1.5 km and 4.5 km were chosen to complete the model suite (Table 2, Figure 11). A 2.5 ° slope was used in all cases as representative of continental slope surface dips onto which the allochthonous sheets would be extruded (Anderson et al., 2004). As LN03B has both a 2.5 ° slope and an initial salt thickness of 3 km, both of which are representative of nature (Bally, 1983; Grando and McClay, 2004), it was chosen as our base case against which all other models are compared.

Model LN04A (thin salt, Figure 11) showed a similar deformation pattern as the 0 ° slope model presented above (LN03A, Figure 10a) although with less faulting and extension in the overburden. Subsidence of the frontal portions of the sediment layers caused thinning of the salt, essentially forming a salt weld. After welding, prograding sediments quickly overtook the advancing salt, covering the salt toe, and further slowing deformation. A counterregional stratigraphic geometry might have formed if salt had completely evacuated the regions below these prograding sediment layers. The salt, however, was trapped below the advancing sediments and unable to escape. The slow advance of salt is recorded by the steepness (44 °) of the subsalt sediment ramp.

Thicker salt (LN04C) resulted in early formation of minibasins that transform into basinward dipping fault blocks with continued sedimentation. Salt advanced 6 km further than in the base model (LN03B), overburden extension was 5 km more, and the subsalt sediment ramp (7 °) was slightly lower. Because of the additional extension, especially during the initial stages of deposition, minibasins were well defined and remained as active depocenters throughout the simulation. Minibasins continued to subside and fill until they welded with the basal wall.

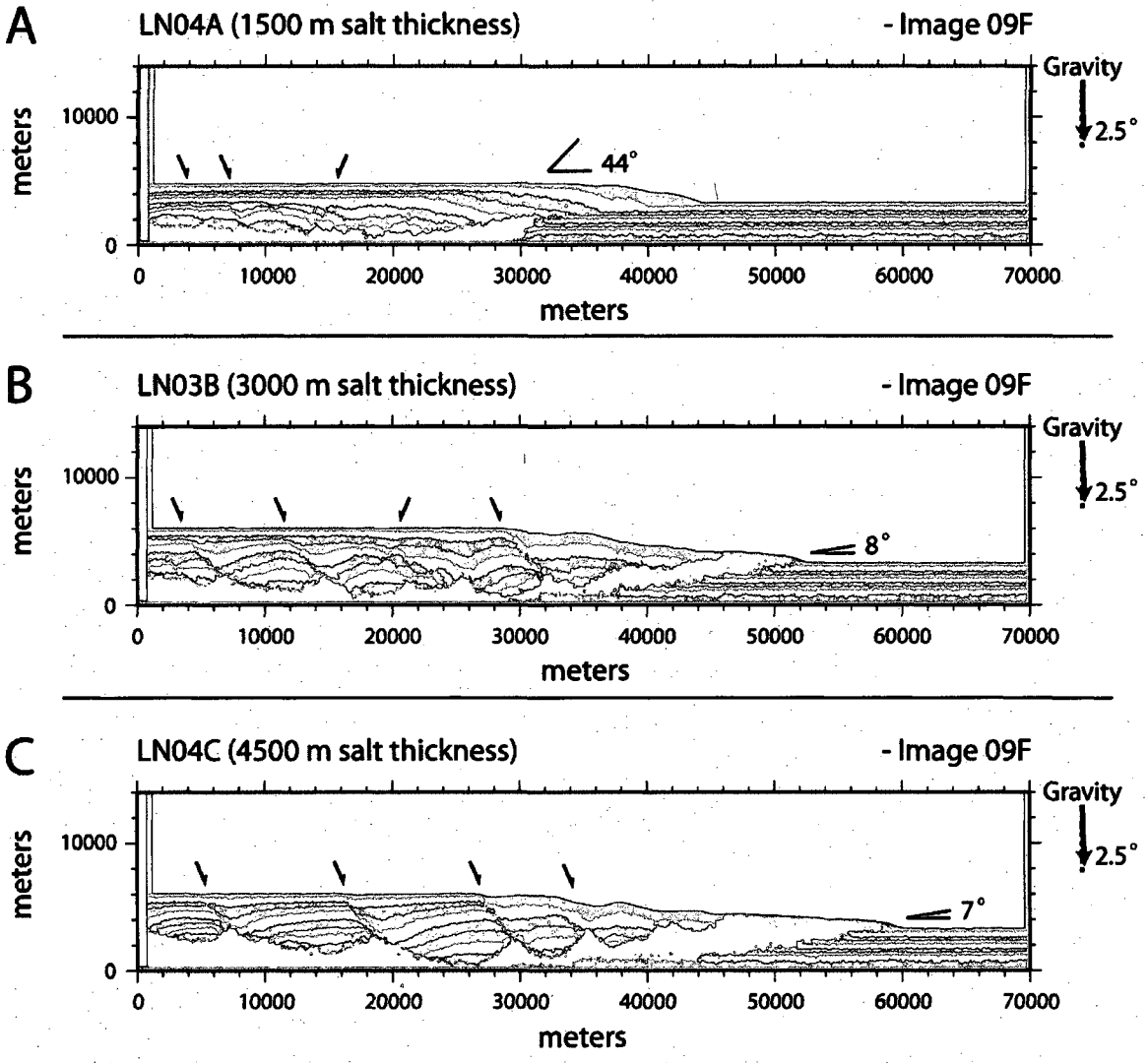

Figure 11: Plots of particle configurations for the suite of models representing variations in initial thickness of salt. A) 1.5 km initial salt thickness. Deformation is similar to LN03A, which formed a counterregional-like sediment geometry. B) 3 km initial salt thickness. Base model (see Figure 10 for description). C) 4.5 km initial salt thickness. Minibasins are well defined and grow very large because they are able to continue subsiding throughout the model run. The deformation pattern forms a roho sediment geometry. Fault positions are denoted by black arrows.

Sediment Thickness

The suite of models for which sedimentation rate was varied by changing the thickness of the sediment packages over constant time increments is displayed in Figure 12. All models in this suite were run on a 2.5 ° basal slope, with an initial salt thickness of 3 km, and compared to the base model LN03B. Two additional sedimentation rates were chosen to complete the suite (125 m/my and 375 m/my, compared to 250m/my for model LN03B, Table 2). Sediment thickness was varied by raising or lowering the prescribed erosion level and increasing or decreasing the number of particles deposited per kilometer in each layer.

Low sediment thickness (LN02A, Figure 12) caused moderate extension of the overburden (9 km) resulting in a series of separated minibasins. Extension occurred mainly on basinward dipping normal faults. Salt advance was lower (13 km) than in the base model, which resulted in a 19 ° subsalt sediment ramp. At the end of the simulation, sediments prograded over the salt sheet toe, slowing deformation.

Early deformation of the high sediment thickness model (LN02C) was dominated by extension of the overburden on basinward dipping normal faults. When the salt sheet thinned sufficiently for the subsiding basins to weld, deformation was taken up by a series of landward dipping normal faults. This style of faulting increased with continuing sedimentation as the sediment layers prograded across the 5 ° subsalt sediment ramp. A graben formed in between these two distinct zones of faulting. Overall overburden extension was 18 km and salt sheet advance was 29 km. The volume of salt expelled from below the sediment overburden increased compared to the other models in this suite (Figure 12).

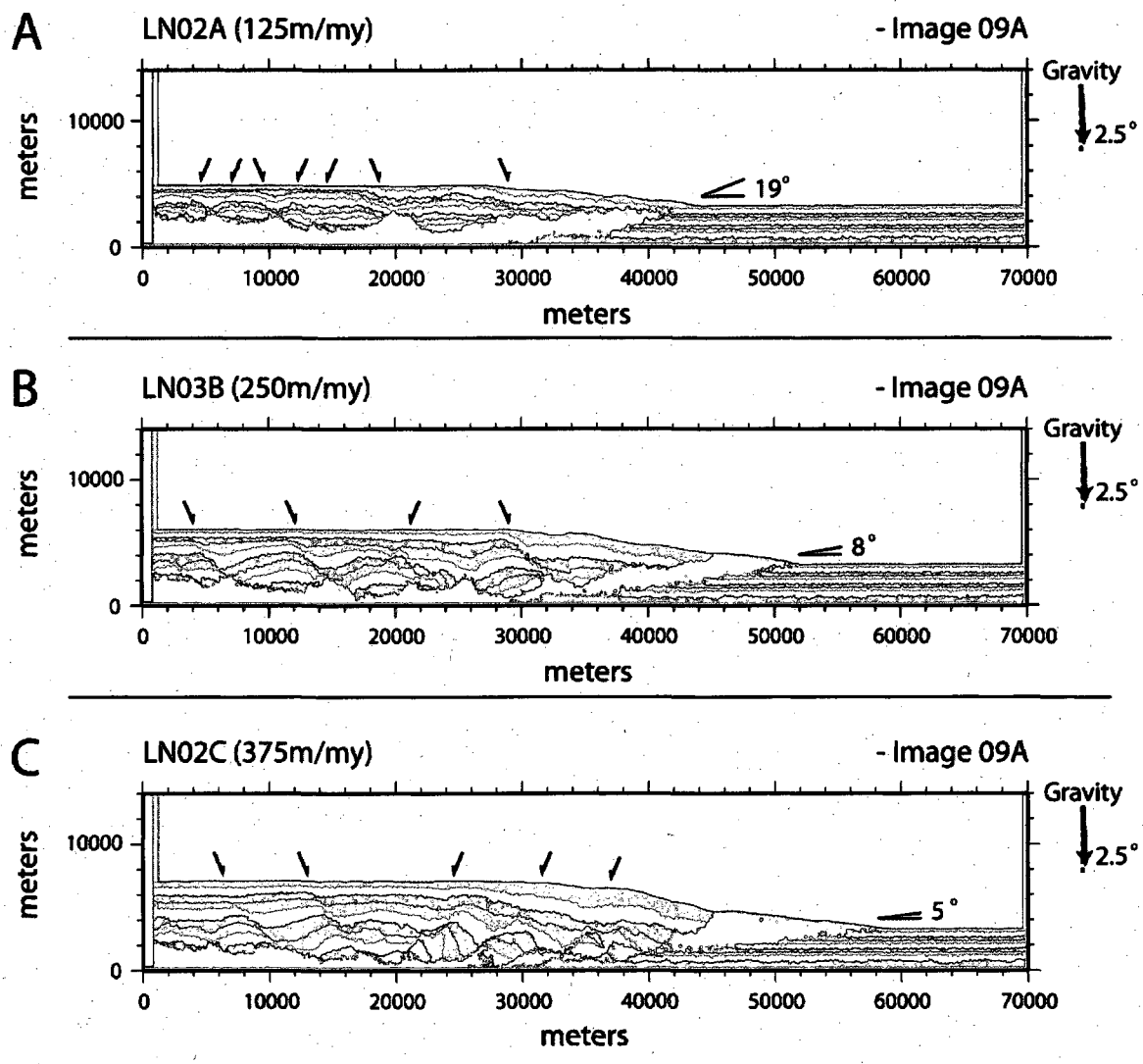

Figure 12: Plots of particle configurations for the suite of models representing variations in sediment thickness. Sedimentation rates represent the minimum aggradation allowed during deposition. Thick sediment layers occur when accommodation space is created by salt evacuation. A) 125 m/my. Minibasin separation and subsidence dominate the deformation. Small basinward dipping faults form near the end of the run, creating limited amounts of listric growth strata. B) 250 m/my. Base model, (see Figure 10 for discussion). C) 375 m/my. Early overburden deformation occurred on basinward dipping faults but switched to landward dipping faults when the salt sheet thinned. Fault positions are denoted by black arrows.

Loading Time

A second test of sedimentation rate was conducted using a suite of models in which the length of time between the deposition of each layer was varied, while maintaining fixed sediment input (Figure 13). Sediment thickness remained constant between the models. LN03BA was run with 1/3 the number of timesteps as the base model (Table 2); i.e., the total number of timesteps per layer deposition and deformation was cut from 180,000 to 60,000 (1 my to 0.33 my). All of the other model parameters remained the same. LN03BA underwent an initial phase of extension through a series of basinward dipping normal faults. When progradation of the sediment layers overtook the thinning front of the salt, this extension switched to mainly landward dipping normal faults across the entire domain. When compared to LN03B (Figure 13c), overburden extension was 7 km less although the salt advanced nearly the same distance. The total volume of salt expelled decreased with less settling time, however, the subsalt sediment ramp remained similar. If the models are compared on the basis of equal run length (when each model reaches 3.33 my; Figure 13a and Figure 13b) instead of equal sediment thicknesses, then LN03BA shows nearly 8 km more salt advance, but 3 km less horizontal sediment extension. A greater volume of salt was expelled by LN03B in all comparisons.

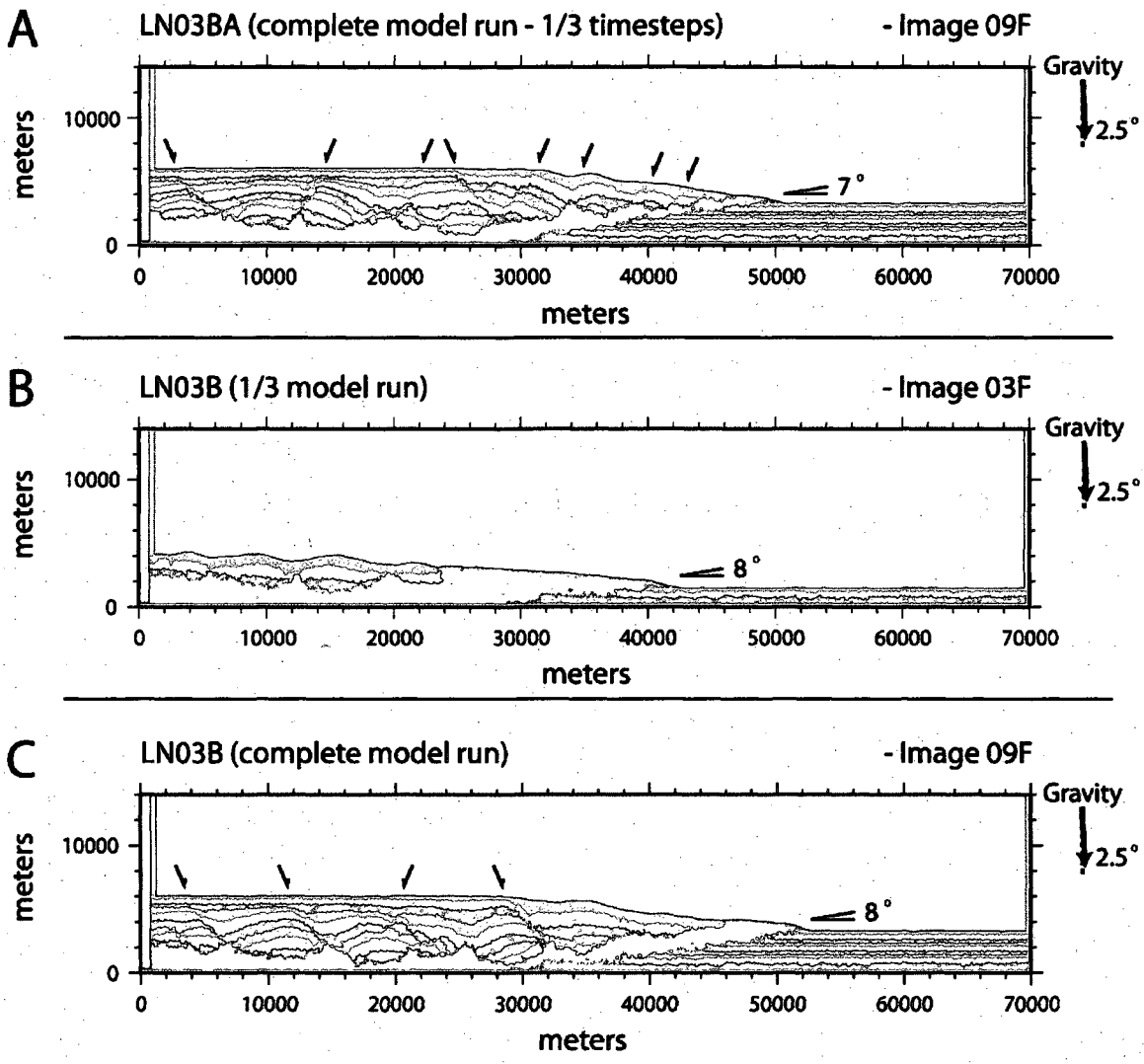

Figure 13: Plots of particle configurations for the suite of models representing variations in length of time allowed between deposition of sediment layers. A) Full model run in 3.33 my. Early deformation occurs on basinward dipping faults but switches to landward dipping faults when the salt sheet thins. B) Base model at 3.33 my or 1/3 of its total run. Deformation is still dominated by the separation of minibasins. Basinward dipping normal faulting has not yet initiated. A greater volume of salt has been expelled than in LN03BA but has not advanced as far. C) Full run time of the base model (10 my)(see Figure 10 for description). Fault positions are denoted by black arrows.

Progradation Rate

Another suite of models varied rates of sediment progradation to explore the effects of sedimentation rate (Figure 14). Sediment layers in the low progradation rate model (LN05A, Figure 14a) advanced 2 km each depositional layer while sediment layers in the moderate (LN03B, Figure 14b) and high (LN05C, Figure 14c) progradation rate models advanced 4 and 6 km, respectively. Other model parameters remained the same. Early deformation was very similar in all of the models, but quickly diverged. Deformation began in LN05A with the formation and separation of minibasins. Because the progradation rate was low, sediment deposition remained well behind the salt sheet toe creating the potential for large amounts of overburden extension as the salt sheet advanced (23 km at the end of the run). The subsalt sediment ramp (11 °) was fairly high. Areas of early diapir growth were suppressed by sediments as the minibasins continued to separate, forming a series of grabens. The frontal portion of the sediment overburden was extended by a listric basinward dipping normal fault.

Deformation during high progradation rates was similar to the patterns observed in LN03BA (Figure 13a) with down-lapping sediment layers quickly overtaking the salt sheet toe. This effectively stopped salt evacuation, despite the low subsalt sediment ramp (4 °). In general, salt advanced the furthest in the highest progradation models (27 km) but a greater volume of salt was expelled from below the overburden in the models with lower progradation rates. Overburden extension also increased for models with lower progradation.

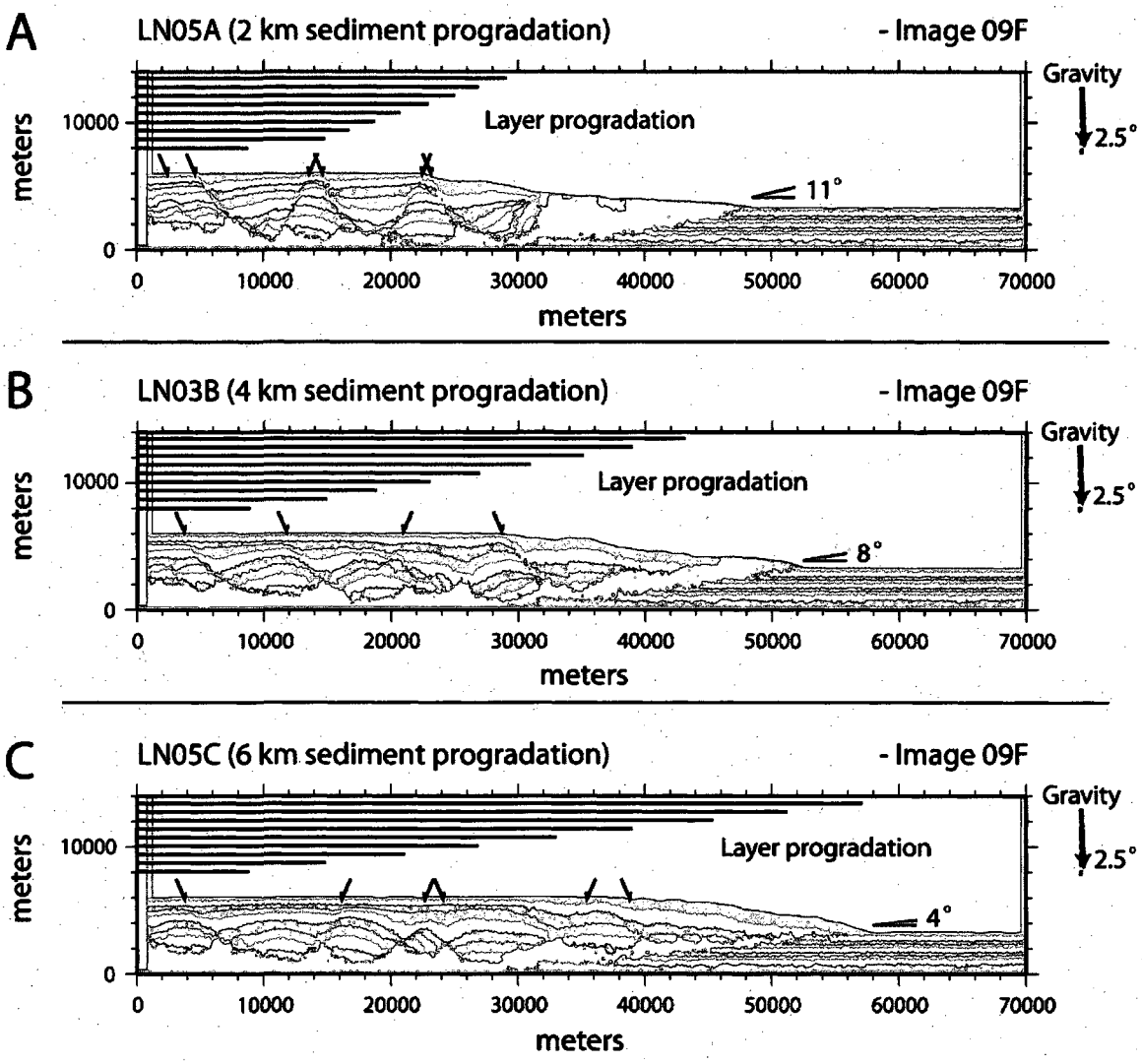

Figure 14: Plots of particle configurations for the suite of models representing variations in progradation rate. A) 2 km progradation every layer. Deformation is dominated by minibasin separation with sediment grabens infilling and deflating the inter-basin salt diapirs. Basinward dipping normal faults control deformation on the front of the overburden. B) 4 km progradation every layer. Base Model (see Figure 10 for a description). C) 6 km progradation every layer. The quick progradation of the sediment layers halts both sediment extension and salt advance as the sediments advance over the salt sheet toe. Fault positions are denoted by black arrows.

Sediment Strength

The effects of mechanical strength variations in the sediment layers were tested by changing the shear and normal components of the interparticle bond strengths (Table 2, Figure 15). A reference case with no bonding is also shown (LN06A Figure 15a). The lowest strength sediment models (LN06A and LN06B) were dominated by distributed deformation (particle flow) because particle bonds broke easily during burial. Overburden extension and salt evacuation were greatest in these models. Deformation of the overburden was dominated by landward dipping normal faults, producing small horsts and grabens. Landward dipping faults were especially prominent near the toe of the overburden where the salt was thinnest as it advanced up the subsalt sediment ramp. The sediment ramp angle was 6 ° for both models.

Intermediate strength models were dominated by horst and graben style faulting (LN06C, Figure 15c). A transition to basinward dipping normal faults occurred at higher sediment strengths (LN06D/LN03B, Figure 15d). The subsalt sediment ramp steepened slightly with greater sediment strength, from 7 ° (LN03C) to 8 ° (LN06D).

The highest strength sediment models (LN06E, Figure 15e; LN06F, Figure 15f) were dominated by the subsidence of minibasins that developed between tensile cracks as new sediment layers were deposited. Salt exploited the tensile cracks to form vertical diapirs wedging the basins apart. Subsequent sediment layers then filled in the space created by the separating minibasins. This style of deformation led to the development of turtle structures with concave-down layers subsiding into the evacuating salt on both sides of the basins. The size of the basins and the angle of the subsalt sediment ramp (10 ° in LN06F, Figure 15f) increased with sediment strength.

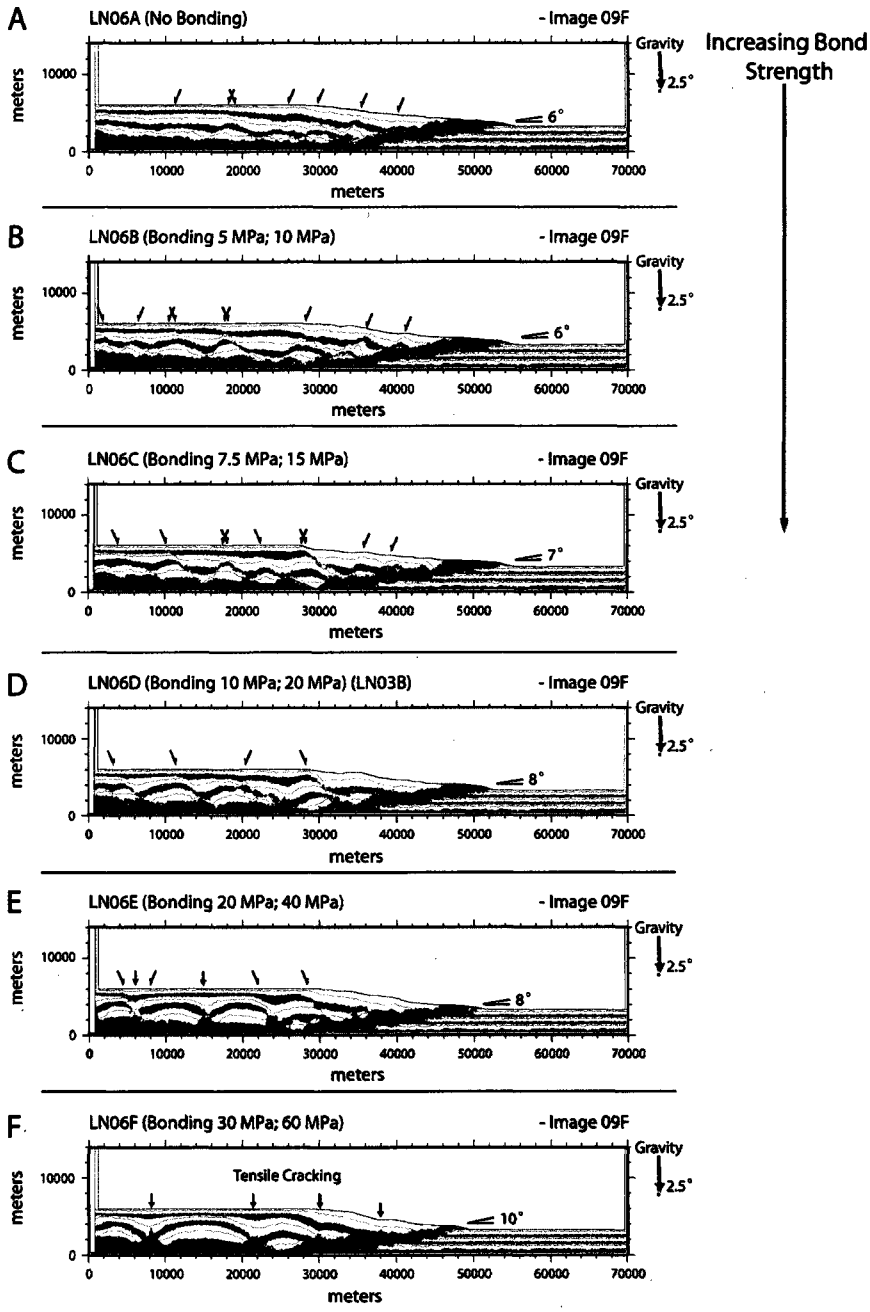

Figure 15: Plots of particle configurations for the suite of models representing variations in sediment strength. The heading of each model shows tensile strength; cohesive strength. A) No bonding. B) Low strength bonds. Overburden extension in A and B forms through distributed deformation, or granular flow. In B the bonds are too weak to remain intact with burial. C and D) intermediate strength bonds. Basinward dipping faults dominate deformation. E and F) High strength bonds. Tensile fractures form between separating minibasins which are exploited by salt diapirs to wedge the basins apart. Turtle structures from as newly deposited sediments subside into these weak areas. Fault positions are denoted by black arrows.

DISCUSSION

As shown from the suites of models, the DEM simulations reproduce realistic deformation features of sediment layers above salt sheets, while reasonably representing the flow and advance of the salt sheet itself. The simulations accurately reproduce natural deformation structures such as salt diapirs, salt nappes, listric growth faults, turtle structures, grabens, and minibasins. The model results also show that variations in the tested model parameters (basal slope, initial salt thickness, sediment thickness, loading time, progradation rate and sediment strength) produce distinctly different salt and sediment structures, providing insights into the controls on natural systems.

Salt Extrusion and Overburden Extension

The relative changes in the rate of salt advance, the volume of salt extruded, and the magnitude of sediment overburden extension, played important roles in determining the structural styles of the models reviewed above.

The volume of salt extruded from beneath the sediment overburden appears to correlate with overburden extension in our models. The models with greatest salt extrusion and sediment extension were: high slope (LN03C, Figure 10c), thick salt (LN04C, Figure 11c), thick sediments (LN02C, Figure 12c), low progradation (LN05A, Figure 14a), and weak sediments (LN06A, Figure 15a). Extension in the overburden provided a driving force that caused the salt to flow more rapidly, inducing extrusion. In some cases, such as high basal slopes, the gravitational instability of the slope allowed salt to flow downhill without the need of significant loading from subsiding and

extending sediment layers. The sediment layers extended as they flowed downslope on top of the evacuating salt.

Despite the correlation of the extrusion of salt to the sediment overburden seen in these simulations, in natural settings, the amount of overburden extension does not always correlate with the total advance of the salt sheet (i.e., the location of the front of the salt sheet through time) (Diegel et al., 1995; Hudec and Jackson, 2006). The majority of our models do show this trend, except for the simulations in the progradation model suite (Figure 14). The salt sheet in the high progradation model (LN05C, Figure 14c) advanced 8 km more than the salt sheet in the low progradation model (LN05A, Figure 14a) but was significantly thinner. The rapidly advancing sediments in the high progradation case pushed the salt forward. However, salt in the main body of the salt sheet was unable to evacuate efficiently because the toe of the salt sheet was overrun by the prograding sediment layers. This also caused a suppression of extension in the sediment overburden (an effect noted by Hudec and Jackson (2006) citing unpublished model results).

The rapid advance of salt in the high progradation model also produced a low subsalt sediment ramp angle. Because the abyssal plain sediments are deposited at the downslope edge of the salt sheet, the ramp provides an excellent marker for the advance of salt through time (Jackson and Talbot, 1991). Rapidly advancing salt sheets, therefore, produce low angle ramps, while salt sheets with little advance produce high angle ramps. The angle of the ramp is also a factor in the development of the emergent structures and deformation, both in the sediment layers and salt, because it can change the basal angle of the salt sheet and slow sediment overburden extension.

Deformation Styles

Faulting

The interplay of overburden extension and salt advance influences the orientation and style of faulting in the sediment overburden. In our models, extension in the overburden was accommodated primarily by basinward or landward dipping normal faults, and occasionally by tensile cracking. In general, basinward dipping faults occurred in areas of high extension (e.g., high slopes and thick salt), whereas landward dipping faults occurred in horst and graben systems or in areas of low extension (e.g., thin salt, low slopes or inverted basal slopes on subsalt sediment ramps).

In some cases (LN02C, Figure 12c), the style of sediment deformation changed from basinward dipping normal faults to landward dipping normal faults midway through the model run. The basinward dipping faults began to form when the salt sheet thinned with the expulsion of salt from beneath the subsiding basinward-dipping fault blocks (Figure 16). With continuing sedimentation, deformation continued on landward dipping normal faults as the prograding layers advanced up the subsalt sediment ramp. Similar effects can be seen in LN03BA (Figure 13a), LN06B (Figure 15b), and LN06C (Figure 15c), where the landward dipping slope of the ramp produced landward dipping faults near the front of the sediment layers despite the predominance of basinward dipping faults elsewhere. This same effect can be observed in natural examples where basinward dipping normal faults form when sediment layers are deposited above the sediment ramp (Schuster, 1995). Changes in the thickness of the salt sheet (by salt evacuation under thick sediments) or the angle of the basal slope (by the subsalt sediment ramp) can have, therefore, a profound effect on the evolution of the system.

The orientation of faulting also changes with the strength of the sediment layers (Figure 15). With increasing sediment strength, fault orientations change from landward dipping in the weakest sediments (Figure 15a) to predominately basinward dipping in the intermediate strength sediments (Figure 15c). Tensile cracking is noted in the strongest sediments (Figure 15f). Landward dipping faults occur in the weakest models because deformation is distributed throughout the overburden (i.e., granular flow). The distributed flow of the sediments also causes more continuous shearing in the underlying salt, resulting in more efficient expulsion. This results in thinning of the salt sheet, causing the predominance of landward dipping faults. Higher strength models are dominated by tensile cracking, because the sediment basins act as coherent blocks that are wrenched apart by the evacuating salt. The spacing of these tensile cracks increases with increasing sediment strength resulting in wider basins.

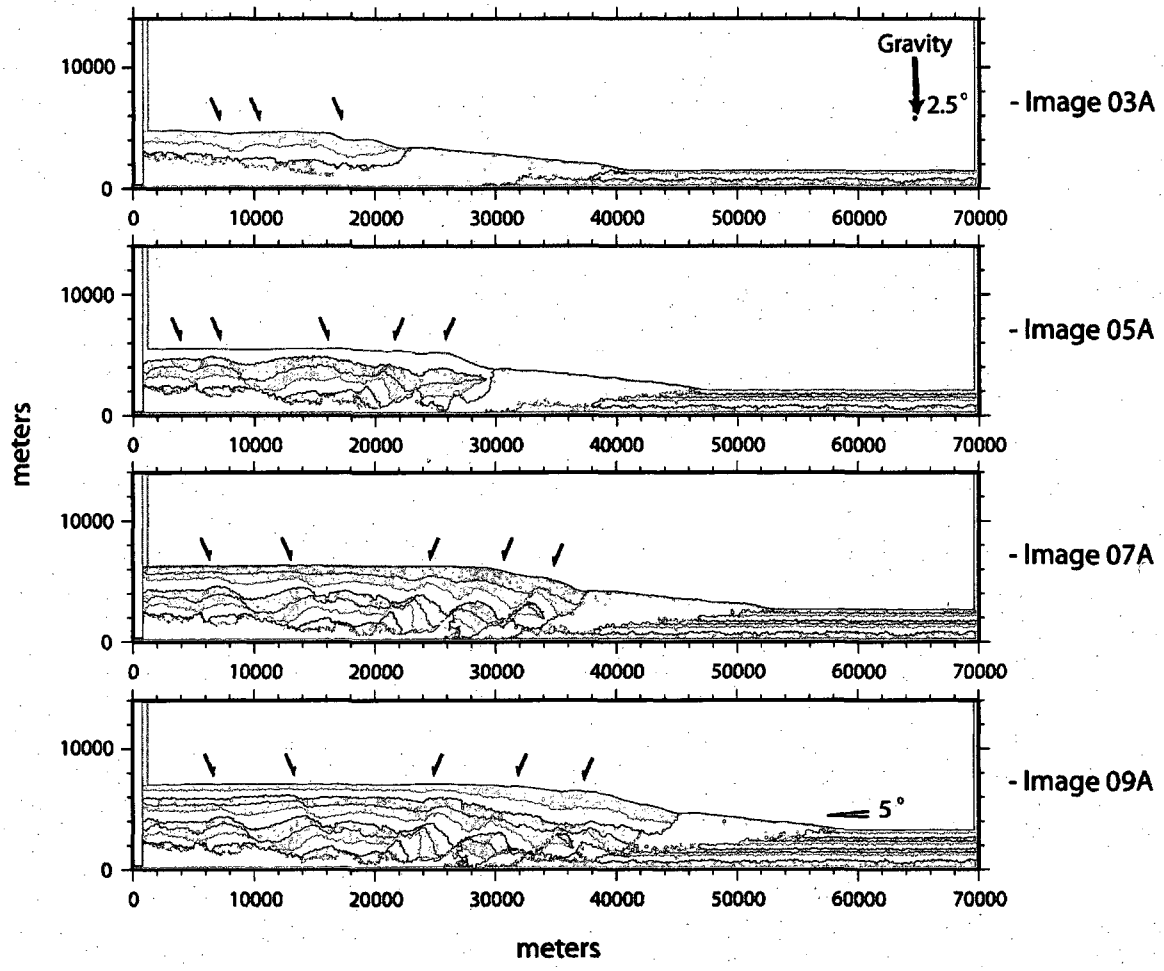

Figure 16: Sequential plots of particle configuration for the progressive growth of simulation LN02C (thick sediment). Deformation began on basinward dipping normal faults but switched to landward dipping normal faults over the portions of the salt sheet that had thinned. As the sediment layers prograded, the subsalt sediment ramp tilted the basal slope of the salt landward and intensified landward faulting. Fault positions are denoted by black arrows.

Roho vs. Counterregional Sediment Geometries

The combination of all these factors (e.g., salt extrusion, sediment progradation, fault orientation, and sediment ramp evolution) results in the evolution of stratigraphic relationships that can be compared to natural examples, and the hypotheses of Hudec and Jackson (2006). Hudec and Jackson (2006) hypothesized that roho sediment geometries should form in areas with high potential for extension, whereas, counterregional sediment

geometries would form where overburden extension is unfavorable (Figure 1). A review of our model results shows that the simulations with the highest overburden extension (high slope, LN03C, Figure 10c; thick salt, LN04C, Figure 11c) closely resembled the stratigraphic relationships of roho systems, with basinward dipping normal faults soling into the salt sheet (e.g., Diegel et al., 1995; Schuster, 1995; Rowan et al., 1999; Hudec and Jackson, 2006). Additional simulations that produced roho geometries included the base model (LN03B) and the moderate sediment strength model (LN06C, Figure 15c).

Exceptions to this trend of roho geometries in models with high overburden extension include simulations with low progradation (LN05A, Figure 14a) and no bonding (LN06A, Figure 15a). The first example (LN05A) shows 23 km of overburden extension, which is only slightly less than the maximum extension shown for sediment extension on the 5 ° basal slope of LN03C (Figure 10c). Instead of roho-type fault blocks, as would be predicted for this much extension, a series of horsts and grabens formed. The low progradation rate also caused less salt front advance, resulting in a steep subsalt sediment ramp. This result shows that not all sediment geometries can be lumped into the end-member cases being studied here (Mcbride et al., 1998).

The second exception to the trend of roho geometries in models with high overburden extension, is the low sediment strength simulation with no bonding (LN06A, Figure 15a). This simulation produced a counterregional sediment geometry, despite 18 km of overburden extension. As discussed above, this model deforms through sediment flow, which is most likely unrealistic on this scale, and therefore, is probably not a good example of a counterregional system.

Simulations with more realistic sediment rheologies produced counterregional sediment geometries at low slopes (LN03A, Figure 10a) and with thin salt (LN04A, Figure 11a). In both models, sediments prograded and subsided as salt slowly advanced up a steep subsalt sediment ramp. Before the salt could completely evacuate, however, the prograding sediment layers overtook the salt sheet toe and halted salt evacuation. This may have prevented true counterregional sediment geometries from forming in these models.

In both counterregional examples, there is very little overburden extension. Other model parameters that suppress extension in the overburden include: short loading time (LN03BA, Figure 13a, 7 km extension), high progradation rates (LN05C, Figure 14c, 13 km extension), and high sediment strength (LN06F, Figure 15f, 11 km extension). Although landward dipping faults were prevalent in some of these models, they did not produce counterregional geometries. Hudec and Jackson (2006) also predicted that strong sediment layers should form counterregional geometries because they would subside without faulting into the salt sheet. Indeed, the strongest sediment simulation (LN06F, Figure 15f) did produce large subsiding basins; however, the subsidence of these basins formed turtle structures, not counterregional sediment geometries. Again, salt evacuation was incomplete.

The suite of models with sediment thickness variations (Figure 12) also produced intriguing results that are somewhat contradictory to the hypotheses presented be Hudec and Jackson (2006). Thin sediment layers were hypothesized to form a weak cover that would stretch and fault to form roho geometries. However, our thin sediment thickness simulation (LN02A, Figure 12a) produced little overburden extension (9 km) and failed

to create any obvious roho geometry. Thick sediment layers are predicted to be strong, and should, therefore, subside without extension to form counterregional geometries. Although the frontal portion of the overburden in the thick sediment simulation (LN02C, Figure 12c) resembles a counterregional geometry, the initial deformation occurred through basinward dipping faults which produced a low subsalt sediment ramp angle and thus, an overall "mixed" system. The basinward dipping faults, however, formed before the salt had thinned sufficiently to induce landward dipping faults. The roho style of deformation also occurred before the overburden sediments approached the subsalt sediment ramp (which effectively tilted the basal slope of the salt sheet landward). As the sediments prograded and were deposited over this portion of the salt sheet, the tendency for landward faulting increased, although extension continued on the basinward dipping faults. The initial slope angle and the initially thick salt provided a high potential for sediment extension (18 km) and allowed the roho style basinward dipping faults to form in the overburden. The thick sediments provided the push to advance the salt sheet forward and create the low subsalt sediment ramp angle.

One of the notable differences between roho and counterregional salt systems observed in nature is that, in general, roho systems form low angle sediment ramps (Schuster, 1995, his Figures 5 and 8; and Rowan et al., 1999, their Figure 13) and counterregional systems form high angle sediment ramps (Schuster, 1995, his Figures 10, 13, and 15). As noted above, the ramp plays an important role in the evolution of deformation in the system and influences, as shown by natural examples in the literature, whether roho or counterregional systems will form. Because the angle of the ramp is controlled by the advance of salt, areas with high potential for salt flow will produce low

angle ramps, whereas, areas with low potential will form high angle ramps. An additional parameter that can affect the angle of the ramp, but that is not varied in our numerical simulations, is the abyssal plain sedimentation rate (Appendix D). The rate of salt advance and the angle of the ramp will also affect the length of the salt sheet. Schuster (1995) suggested that shorter salt sheets were more likely to produce counterregional systems. In our models, the parameters that produced the lowest salt expulsion and advance were low basal slope (LN03A, Figure 10a) and thin salt (LN04a, Figure 11a). As predicted, these simulations also produced high angle ramps, short salt sheets, and counterregional-like geometries.

Low basal slope and a thin initial salt thickness, therefore, are important natural parameters in the creation of counterregional geometries because overburden extension is suppressed, salt advance is slow, and a high angle subsalt sediment ramp is produced. However, even with limited extension in the sediment overburden in our low slope and thin salt simulations, the salt did not completely evacuate to form true counterregional sediment geometries. This may reflect inconsistencies in the rheology and kinematics of our modeled salt as compared to real salt flow.

Salt Kinematics

To better understand this phenomenon, an investigation of salt flow profiles in our models was undertaken. Past researchers have linked the mode of viscous salt flow to sediment deformation in the overburden (Last, 1988; Gemmer et al., 2004, 2005; Ings et al., 2004; Hudec and Jackson, 2006; Cartwright and Jackson 2008; Brun and Mauduit, 2009). In particular, when faults occur in the sediment overburden, fault offset induces

simple shear (Couette flow) in the underlying salt. Pure shear (Poiseuille flow) occurs when sediment basins remain un-faulted and sediments subside without lateral translation (Last, 1988; Gemmer et al., 2004, 2005; Cartwright and Jackson, 2008) (Figure 18). A snapshot of LN04C taken after the deposition of the sixth sediment layer (Figure 17) shows that incremental displacement, which correlates with flow rate, in the salt increases from left to right. The greatest flow velocities occur at the toe of the slope where deformation occurs by Couette flow. This pattern of deformation (Couette flow of salt on slopes) was also observed in the numerical models of Ings et al. (2004). Salt flow in the back of the salt sheet also occurs by Couette flow. This flow type occurs because sediment velocities, seen on the flow profile, exceed those for the salt, inducing lateral shear in the salt (Gemmer et al., 2004). A close examination of the flow profile located at 30 km reveals that beneath the toe of the sediment overburden, salt flows by a combination of Couette and Poiseuille flow (Figure 17). The subsidence of the new sediments deposited in this region induces Poiseuille flow, while Couette flow is induced by the downslope flow of salt.

As shown in Figure 17, both Couette flow and Poiseuille flow occur in our models. Why then are counterregional geometries less common than roho geometries? The answer may lie in the granular nature of the salt proxy that we have used in these experiments. Although we have successful created a material that has the ability to flow through both Poiseuille and Couette flow, the pressure dependent rheology of our granular salt suppresses Poiseuille flow by resisting shear deformation at depth (Figure 5). Shallow salt flows more readily, particularly with the driving force created by the overburden sediments sliding downslope, favoring Couette flow profiles. Counterregional

geometries should form as sediment basins subside without faulting, however, when conditions dictate low extension of the overburden sediments (e.g., LN03A, LN04A, LN03BA, LN05C) the limited ability of the particulate salt to deform by Poiseuille flow prevents the salt from completely evacuating. This failure of our models may demonstrate the importance of Poiseuille flow in the creation of counterregional systems. Roho stratigraphic geometries will form when faulting and overburden extension induces Couette flow in the underlying salt, inducing shear, whereas counterregional stratigraphic geometries will form when the overburden subsides without significant extension into the underlying salt, inducing Poiseuille flow (Figure 18).

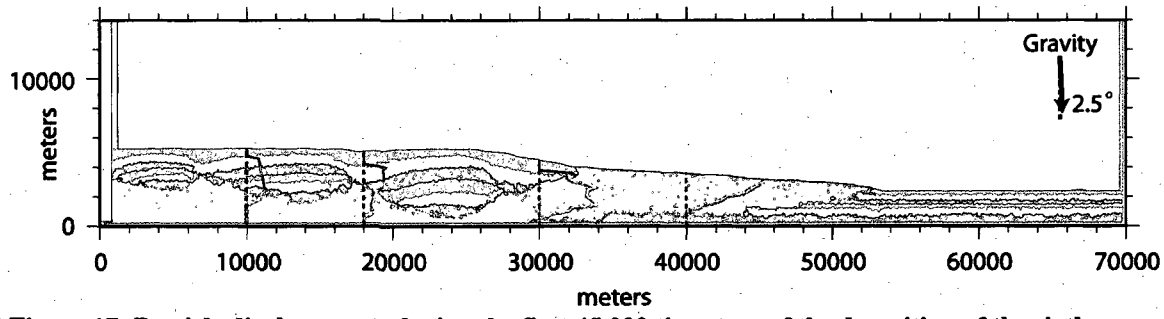

Figure 17: Particle displacements during the first 45,000 timesteps of the deposition of the sixth depositional layer of model LN04C (note 2.5 degree basal slope). Blue lines representing the total displacements of the particles along vertical profiles at 10, 18, 30, and 40 km. Displacements on the back of the salt sheet show that flow in the salt occurs by Couette flow. Flow at the front of the overburden occurs by a combination of Poiseuille and Couette flow. Flow at the toe of the salt occurs by Couette flow as salt advances downslope.

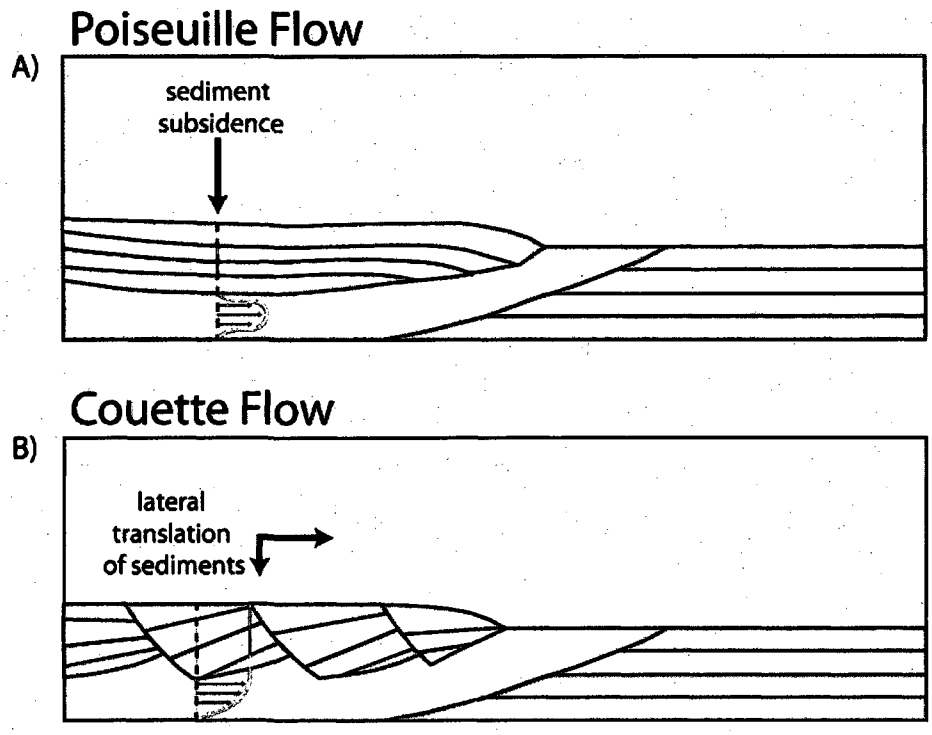

Figure 18: Cartoon representing the different modes of viscous salt flow and the accompanying sediment deformation. Blue lines represent the relative displacement of the area along the dotted line through time. A) Poiseuille flow occurs when coherent sediment basins subside into the underlying salt layers without significant faulting. B) Couette flow is induced in the salt layer when sediment displacement exceeds the velocity of salt, inducing simple shear in the upper layers of salt.

Sedimentation Rate

Despite the challenges posed by granular salt flow, the results presented are sufficient to show the importance of basal slope angle and initial salt thickness. The effect of the sedimentation rate on the evolution of the system is more elusive.

Increasing sediment thickness (aggradation) and increasing progradation both cause increases in sedimentation rate, i.e., greater depositional volumes in the sediment layers. A reduction in the time between layer deposition is also effectively an increase in the progradation rate. This is supported by the similarity of the model results for reduced run time (LN03BA, Figure 13a) and high progradation (LN05C, Figure 14c). Hudec and Jackson (2006) proposed that higher sedimentation rates would result in counterregional systems and low sedimentation rates would produce roho systems. None of the sedimentation rate simulation suites presented here produced end member roho or counterregional geometries. However, variations of sediment thickness and progradation produced key changes to the overall geometry of the system (i.e., ramp angle, overburden extension), that could influence the development of one of the end member geometries over the other.

Thick sediment layers, in our simulations, produce low angle ramps and large overburden extension while thin sediment layers produce high angle ramps and low overburden extension. The frontal portion of the overburden in the thick sediment layer model (LN02C, Figure 12c) forms a counterregional geometry, despite the low angle of the ramp. Our simulations also show that high progradation rates produce low angle ramps due to an increase in salt front advance rate, while low progradation rates produce

an increase in the ramp angle, despite an increase in the volume of salt evacuated from beneath the overburden.

The thick sediment layer model (LN02C, Figure 12c) also had a fairly high progradation rate (4 km/layer). This factor may have helped produce the low ramp angle while the thick sediment layers themselves caused the expulsion of salt, resulting in the counterregional overburden frontal geometry. The geometry produced in this simulation may be analogous to the expulsion rollover sediment geometries observed in nature and modeled by Ge et al. (1997). Their models show that progradation of sediment layers can cause salt expulsion and basinward-dipping expulsion sediment rollovers with a flat base, consistent with restorations from the Gulf of Mexico (Wu et al., 1990) and offshore Brazil (Demercian et al., 1993; Mohriak et al., 1995). In our models, high progradation rates drive salt forward, maintaining a low ramp angle, while thick sediments provide the pressure required to drive salt expulsion from beneath the sediment overburden.

Low progradation rates, in our simulations, also result in an increase in salt expulsion. However, the ramp angle is high because the salt is not driven forward by the advancing sediment front. A combination of low progradation, which creates the high angle ramp, and thick sediment layers, which provide the head for salt extrusion, may produce the end-member counterregional geometry observed in nature.

Another factor that is not considered in this study is the sedimentation rate over the abyssal plain region of our simulations. However, if the allochthonous salt sheet was not emergent at the edge of the continental slope, as presented in these models, then the sedimentation rate in front of the salt sheet may be larger than the rates presented, resulting in high ramp angles and counterregional geometries. This effect can be seen in

the thin sedimentation rate simulation (LN02A, Figure 12a) which had a high angle ramp due to the relatively high sedimentation rate in front of the salt sheet. This occurred because the abyssal plain sedimentation rate was not varied in accordance to the lower sedimentation rate over the salt sheet. This observation is consistent with the hypotheses of Hudec and Jackson (2006) who noted that several examples of salt evacuation systems in the Gulf of Mexico changed from roho to counterregional after they were brought inbound of the continental shelf break.

In an effort to further understand the effects of sedimentation rate on the emergent structures of salt systems, the relative sedimentation rates of the models that produced roho (LN03B, LN03C and LN04C) and counterregional (LN03A and LN04A) systems were also analyzed in more detail. The relative sediment flux in each of these models was quantified by summing deposited particles in each layer, and correcting for erosion (

Figure 19). The sedimentation rates shown appear to indicate that counterregional systems formed at lower sedimentation rates than roho systems. However, models with mixed sediment geometries (such as LN02C, with very high sedimentation rates) are excluded from this figure, and could have a significant impact on the result. This result may also be biased by the incomplete salt evacuation in the counterregional examples produced in our simulations, which resulted in less accommodation space. This result may show, however, that the interplay of sediment aggradation and sediment progradation may be more important to the overall development of the system than simply the amount of sediment added.

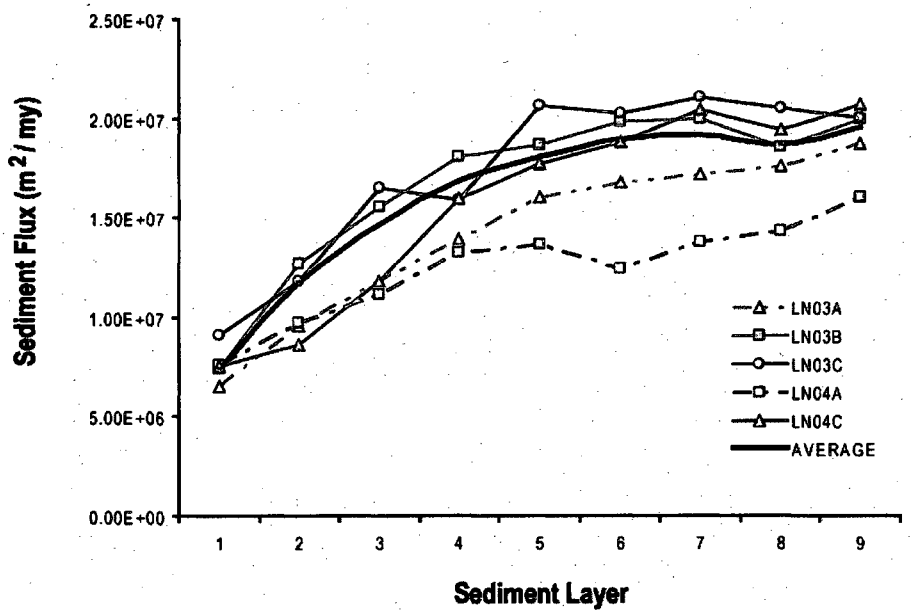

Figure 19: Plot of sediment flux for the models that showed apparent roho and counterregional sediment geometries. Counterregional models are shown with dashed lines and roho examples are shown with solid lines. An average sedimentation flux was also calculated for all models and graphed.

CONCLUSION

The simulations presented here show that realistic deformation and geometries of evolving salt sheets and their sediment overburdens can be created using DEM models. The models were able to capture realistic rheologies of supra-salt sediments using both non-cohesive and cohesive particles, thereby, reproducing realistic sediment deformation. Deformation occurred by landward dipping normal faults, basinward dipping normal faults and tensile cracking (at high sediment strengths) which accommodated overburden extension due to the evacuation of salt. In general, overburden extension correlated with salt front advance and salt extrusion. The rate of salt advance also determined the slope of the subsalt sediment ramp, which had a significant impact on determining the final

stratigraphic geometry. Salt advance was greatest under conditions of high slope and thick salt, which produced low angle ramps and roho sediment geometries. Low angle ramps were also created by high progradation rates, resulting in expulsion rollover sediment geometries. Low slopes and thin salt decreased the advance of salt, thereby, producing steep ramps and counterregional geometries. Counterregional geometries may also be created with low progradation rates and high aggradation. These results agree, generally, with the models for salt sheet advance presented by Hudec and Jackson (2006). However, we add that the relative rates of sediment progradation and aggradation play an important role in determining the final geometry of the system.

Although both Couette flow and Poiseuille flow occur in the granular salt used in these simulations, a lack of complete salt evacuation in our counterregional system examples appears to be caused by a deficiency of Poiseuille flow beneath the subsiding sediment basins. This appears to demonstrate the importance of flow type in controlling the evolution of salt structures.

Although further research in this field is needed to advance the techniques discussed in this paper, these models provide a basis for the use of the discrete element method to better understand the evolution of salt tectonic systems. The forward modeling of the areas around salt bodies will aid researchers in their understanding of the evolution of possible hydrocarbon traps and the migration of hydrocarbons pathways as these structures evolve.

REFERENCES CITED

Anderson, J.B., Rodriguez, A., Abdulah, K., Banfield, L.A., Bart, P., Fillon, R., McKeown, H., and Wellner, J., 2004, Late Quaternary stratigraphic evolution of the northern Gulf of Mexico: a synthesis: in Anderson, J.B., and Fillon, R. H., eds., Late Quaternary Stratigraphic Evolution of the Northern Gulf of Mexico Basin, Society of Sedimentary Research, Special Publication No. 79, p. 1-24.

Bally, A. W., 1983, Seismic Expression of Structural Styles, Vol 3, Tulsa, OK, The American Association of Petroleum Geologists.

Brun, J. P. and T. P. O. Mauduit, 2009, Salt rollers: Structure and kinimatics from analogue modeling: Marine and Petroleum Geology, v. 26, p. 249-258.

Byerlee, J.D., 1978, Friction of rocks: Pure Applied Geophysics, v. 116, p. 615-626.

Carter, N. L., S. T. Horseman, J. E. Russell, and J. Handin, 1993, Rheology of rocksalt: Journal of Structural Geology, v. 15, p. 1257-1271.

Cartwright, J. A. and Jackson, M. P. A., 2008, Initiation of gravitational collapse of an evaporite basin margin: The Messinian saline giant, Levant Basin, eastern Mediterranean: GSA Bulletin, v. 120, p. 399-413.

Cho, N., C. D. Martin, and D. C. Sego, 2007, A clumped particle model for rock: International Journal of Rock Mechanics and Mining Sciences, v. 44, p. 997-1010.

Cobbold, P. R., P. Szatmari, L. S. Dermercian, D. Coelho, and E. A. Rossello, 1995, Seismic and experimental evidence for the thin-skinned horizontal shortening by convergent radial gliding on evaporites, deep-water Santos Basin, Brazil, in M. P. A. Jackson, D. G. Roberts, and S. Snelson, eds., Salt Tectonics: a global perspective: AAPG Memoir 65, p. 305-321.

Cotton, J. T., and H. A. Koyi, 2000, Modeling of thrust fronts above ductile and frictional detachments: Application to the structures in the Salt Range and Potwar Plateau, Pakistan: GSA Bulletin, v. 112, p. 351-363.

Cramez, C. D., and M. P. A. Jackson, 2000, Superposed deformation straddling the continental-oceanic transition in deep-water Angola: Marine and Petroleum Geology, v. 17, p. 1095-1109.

Cundall, P. A., and O. D. L. Strack, 1979, A discrete numerical model for granular material: Geotechnique, v. 29, p. 47-65.

Dermercian, S., P. Szatmari, and P. R. Cobbold, 1993, Style and pattern of salt diapirs due to thin-skinned gravitational gliding, Campos and Santos basins, offshore Brazil: Tectonophysics, v. 228, p. 393-433.

Diegal, F. A., J. F. Karlo, D. C. Schuster, R. C. Shoup, and P. R. Tauvers, 1995, Cenozoic structural evolution and tectono-stratigraphic framework of the northern Gulf Coast continental margin, in M. P. A. Jackson, D. G. Roberts, and S. Snelson, eds., Salt Tectonics: a global perspective: AAPG Memoir 65, p. 109-151.

Duval, B., C. Cramez, and M. P. A. Jackson, 1992, Raft tectonics in the Kwanza Basin, Angola: Marine and Petroleum Geology, v. 9, p. 389-404.

Fletcher, R. C., M. R. Hudec, and I. A. Watson, 1995, Salt glacier and composite sediment-salt glacier models for the emplacement and early burial of allochthonous salt sheets, in M. P. A. Jackson, D. G. Roberts, and S. Snelson, eds., Salt Tectonics: a global perspective: AAPG Memoir 65, p. 77-108.

Fort, X., J. P. Brun, and F. Chauvel, 2004, Salt tectonics on the Angolan margin, synsedimentary deformation processes: AAPG Bulletin, v. 88, p. 1523-1544.

Galloway, W. E., 2005, Gulf of Mexico Basin depositional record of Cenozoic North American drainage basin evolution: Special Publication of the International Association of Sedimentology 35, P. 409-423.

Ge, H., M. P. A. Jackson and B. C. Vendeville, 1997, Kinematics and dynamics of salt tectonics driven by progradation, AAPG Bulletin, v. 81, p. 398-423.

Gemmer, L., S. J. Ings, S. Medvedev, and C. Beaumont, 2004, Salt tectonics driven by differential sediment loading: stability analysis and finite-element experiments: Basin Research, v. 16, p. 199-218.

Gemmer, L., C. Beaumont, and S. J. Ings, 2005, Dynamic modeling of passive margin salt tectonics: effects of water loading , sediment properties and sedimentation patterns: Basin Research, v. 17, p. 383-402.

Giles, K. A. and T. F. Lawton, 1999, Attributes and evolution of an exhumed salt weld, La Popa basin, northeastern Mexico: Geology, v. 27, p. 323-326.

Giles, K. A. and T. F. Lawton, 2002, Halokinetic sequence stratigraphy adjacent to the El Papalote diapir, northeastern Mexico: AAPG Bulletin, v. 86, p. 823-840.

Grando, G. and K. McClay, 2004, Structural evolution of the Frampton growth fold system, Atwater Valley-Southern Green Canyon area, deep water Gulf of Mexico: Marine and Petroleum Geology, v. 21, p. 889-910.

Hafid, M., 2006. Styles structuraux du Haut Atlas de Cap Tafelney et de la partie septentrionale du Haut Atlas occidental: Tectonic salifère et relation entre l'Atlas et l'Atlantique: Notes Mém. Serv. Géol. Maroc 465, p. 172

Halbouty, M. T., 1979, Salt Domes: Gulf Region, United States and Mexico: Gulf Publishing Company, Houston, TX.

Hsü, K. J., Ryan, W. B. F., Cita, M. B., 1973, Late Miocene desiccation of the Mediterranean: Nature, v. 242, p. 240-244.

Hsü, K. J., Montadert, L., Bernoulli, D., Cita, M. B., Erickson, A., Garrison, R. E., Kidd, R. B., Melieres, F., Müller, C., Wright, R., 1977, History of the Messinian salinity crisis: Nature, v. 267, p. 399-403.

Hubbert, M. K., 1937, Theory of scale models as applied to the study of geologic structures: Bulletin of the Geological Society of America, v. 48, p. 1459-1520.

Hudec, M. R. and M. P. A. Jackson, 2006, Advance of allochthonous salt sheets in passive margins and orogens: AAPG Bulletin, v. 90, p. 1535-1564.

Hudec, M. R. and M. P. A. Jackson, 2007, Terra infirma: Understanding salt tectonics: Earth-Science Reviews, v. 82, p. 1-28.

Ings, S. J., C. Beaumont, L. Gemmer, 2004, Numerical modeling of salt tectonics on passive continental margins: preliminary assessment of the effects of sediment loading , buoyancy, margin tilt, and isostasy: 2004 GCSSEPM Foundation Bob F. Perkins Research Conference papers (on CD).

Jackson, M. P. A., and C. J. Talbot, 1986, External shapes, strain rates, and dynamics of salt structures: Geological Society of America Bulletin, v. 97, p. 305-323.

Jackson, M. P. A., and C. J. Talbot, 1991, A glossary of salt tectonics: Geology Circular, Bureau of Economic Geology, Univ. of Texas, Austin, Texas, v. 91, p. 44.

Jaeger, J. C., and N. G. W. Cook, Fundamentals of Rock Mechanics, Chapman and Hall, London, 1969.

Johnson, K. L., Contact Mechanics, Cambridge Univ. Press, New York, 1985

Karig, D., and J. K. Morgan, 1994, Tectonic deformation: stress paths and strain histories in A. Maltman ed., The Geologic Deformation of Sediments, p. 167-204.

Koyi, H., and K. Petersen, 1993, Influence of basement faults on the development of salt structures in the Danish Basin: Marine and Petroleum Geology, v. 14, p. 117-142.

Last, N. C., 1988, Deformation of a sedimentary overburden on a slowly creeping substratum: in Swoboda, G., ed., Numerical Methods in Geomechanics, Innsbruck 1988, p. 2-10

Laudon, R. C., 1984, Evaporite diapirs in the La Popa basin, Nuevo Leon, Mexico: Geologic Society of America Bulletin, v. 95, p. 1219-1225.

Lundin, E. R., 1992, Thin-skinned extensional tectonics on a salt detachment, northern Kwanza Basin, Angola: Marine and Petroleum Geology, v. 9, p. 405-411.

McAdoo, B. G., L. F. Pratson, and D. L. Orange, 2000, Submarine landslide geomorphology, US continental slope: Marine Geology, v. 169, p. 103-136.

Mcbride, B. C., M. G. Rowan, and P. Weimer, 1998, The evolution of allochthonous salt systems, Northern Green Canyon and Ewing Bank (Offshore Louisiana), Northern Gulf of Mexico: AAPG Bulletin, v. 82, p. 1013-1036.

Mohriak, W. U., J. M. Macedo, R. T. Castellani, H. D. Rangel, A. Z. N. Barros, M. A. L. Latge, J. A. Ricci, A. M. P. Mizusaki, P. Szatmari, L. S. Demercian, J. G. Rizzo and J. R. Aires, 1995, Salt tectonics and structural styles in the deep-water province of the Cabo Frio region, Rio de Janeiro, Brazil, in M. P. A. Jackson, D. G. Roberts, and S. Snelson, eds., Salt Tectonics: a global perspective: AAPG Memoir 65, p. 305-321.

Morgan, J. K. and M. S. Boettcher, 1999, Numerical simulations of granular shear zones using the distinct element method: 1. Shear zone kinematics and the micromechanics of localization: Journal of Geophysical Research, v. 104, p. 2703-2719.

Morgan, J.K., 2004, Particle dynamics simulations of rate and state dependent frictional sliding of granular fault gouge: Pure Appl. Geophys., v. 161, p. 1877-1891.

Morgan, J. K. and P. J. McGovern, 2005, Discrete element simulations of gravitational volcanic deformation: 1. Deformation structures and geometries: Journal of Geophysical Research, v. 110.

Morgan, J. K. and P. J. McGovern, 2005, Discrete element simulations of gravitational volcanic deformation: 2. Mechanical analysis: Journal of Geophysical Research, v. 110.

O'Conner, S. M. and P. Weimer, 2004, Structural evolution of northern South Marsh Island, northern Gulf of Mexico: Analysis of a hybrid roho-stepped counter-regional slat system, and kinematic evolution of normal growth and linkage patterns: Gulf Coast Association of Geological Societies Transactions, v. 54, p. 557-572.

Oda, M. and K. Iwashita, Editors, Mechanics of Granular Materials: An Introduction, A.A. Balkema, Rotterdam (1999).

Potyondy, D. O., and P. A. Cundall, 2004, A bonded-particle model for rock: International Journal of Rock Mechanics and Mining Sciences, v. 41, p. 1329-1364.

Potyondy, D. O., 2007, Simulating stess corrosion with a bonded-particle model for rock: International Journal of Rock Mechanics and Mining Sciences, v. 44, p. 677-691.

Remmelts, G., 1995, Fault-related salt tectonics in the southern North Sea, the Netherlands, in M. P. A. Jackson, D. G. Roberts, and S. Snelson, eds., Salt Tectonics: a global perspective: AAPG Memoir 65, p. 261-272.

Rowan, M. G., M. P. A. Jackson, and B. D. Trudgill, 1999, Salt-related fault families and fault welds in the northern Gulf of Mexico: AAPG Bulletin, v. 85, p. 1454-1484.

Rowan, M. G., T. F. Lawton, K. A. Giles, and R. A. Ratliff, 2003, Near-salt deformation in La Popa basin, Mexico, and the northern Gulf of Mexico: A general model for passive diapirism: AAPG Bulletin, v. 87, p. 733-756.

Rowan, M. G., F. J. Peel, and B. C. Vendeville, 2004, Gravity-driven fold belts on passive margins, in K. R. McClay, ed., Thrust tectonics and hydrocarbon systems: AAPG Memoir 82, p. 157-182.

Rowan, M. G. and B. C. Vendeville, 2006, Foldbelts with Early salt withdrawl and diapirism: Physical model and examples from the northern Gulf of Mexico and the Flinders Ranges, Australia: Marine and Petroleum Geology, v. 23, p. 871-891.

Saffer, D. M., and C. J. Marone, 2003, Comparison of smectite- and illite-rich gouge frictional properties: Implications for the updip limit of the seismogenic zone along subduction megathrusts: Earth Planet. Sci. Lett., v. 215, p. 219-235.

Satake, M., 1999, Discrete Mechanics: Correspondence between discrete and continuum mechanical quantities: in M. Oda and K. Iwashita, eds., Mechanics of Granular Materials, p. 8-13.

Schultz-Ela, D. D., 2003, Origin of drag folds bordering salt diapirs: AAPG Bulletin, v. 87, p. 757-780

Schuster, D. C., 1995, Deformation of allochthonous salt and evolution of related salt-structural systems, eastern Louisiana Gulf Coast in M. P. A. Jackson, D. G. Roberts, and S. Snelson, eds., Salt Tectonics: a global perspective: AAPG Memoir 65, p. 177-198.

Talbot, C. J. and P. Aftabi, 2004, Geology and models of salt extrusion at Qum Kuh, central Iran: Journal of the Geological Society of London, v. 161, p. 321-334.

Vail, P. R., R. M. Mitchum, R. G. Todd, J. M. Widmier, S. Thompson, J. B. Sangree, J. N. Bubb, and W. H. Hatlelid, 1977, Seismic stratigraphy and global sea level in C.

E. Payton, ed., Seismic Stratigraphy – applications to hydrocarbon exploration, p. 49 -212

van Keken, P. E., C. J. Spiers, A. P. van der Berg and E. J. Muyzert, 1993, The effective viscosity of rocksalt: implementation of steady-state creep laws in numerical models of salt diapirism: Tectonophysics, v. 225, p. 457-476.

Velde, B., 1996, Compaction trends of clay-rich deep sea sediments: Marine Geology, v. 133, p. 193-201.

Vendeville, B. C. and M. P. A. Jackson, 1992, The rise of diapirs during thin-skinned extension: Marine and Petroleum Geology, v. 9, p. 331-353.

Vendeville, B. C. and M. P. A. Jackson, 1992, The fall of diapirs during thin-skinned extension: Marine and Petroleum Geology, v. 9, p. 354-371.

Wu, S., A. W. Bally, and C. Cramez, 1990, Allochthonous salt, structure and stratigraphy of the northeastern Gulf of Mexico: Part II – Structure: Marine and Petroleum Geology, v. 7, p. 334-370.

Yun, T. S., G. A. Narsilio, and J. C. Santamarina, 2006, Physical characterization of core samples recovered from the Gulf of Mexico: Marine and Petroleum Geology, v 23, p. 893-900.

Appendix A: Summary of Simulations

The following figures provide time progressive snapshots of each of the simulations described above as they evolved under the differential loads placed upon them. The snapshots shown were taken directly after the deposition of the sediment layer indicated by the image number to the right of the snapshot (e.g., the 3rd sediment layer has just been deposited in "Image 03A"). The last image in each figure represents the final configuration of the simulation after the deposition and deformation of the 9th sediment layer and is labeled as "Image 09F". Specific parameters for each simulation are given in Table 2.

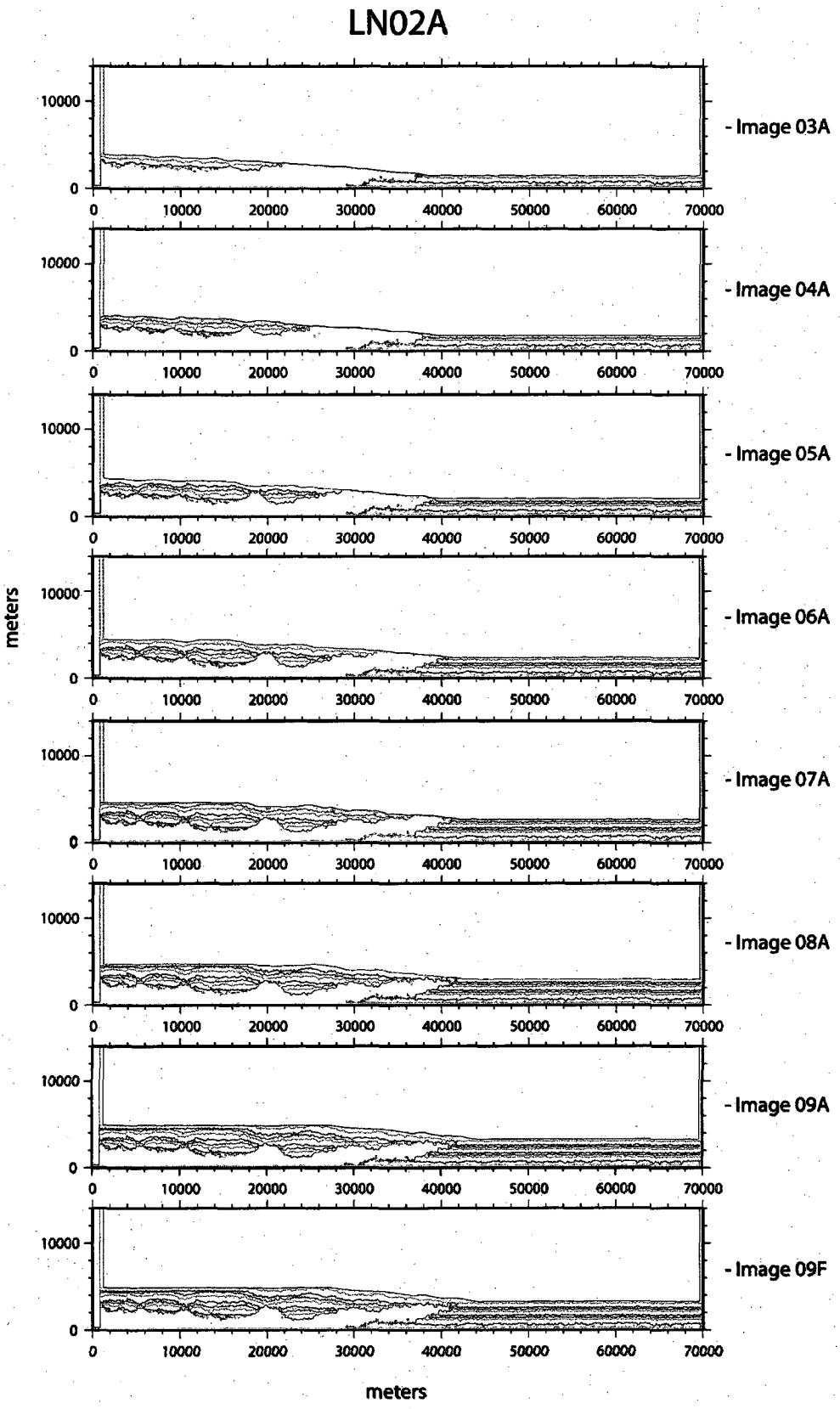

Figure A-1: Time progressive snapshots of the low sediment thickness model LN02A

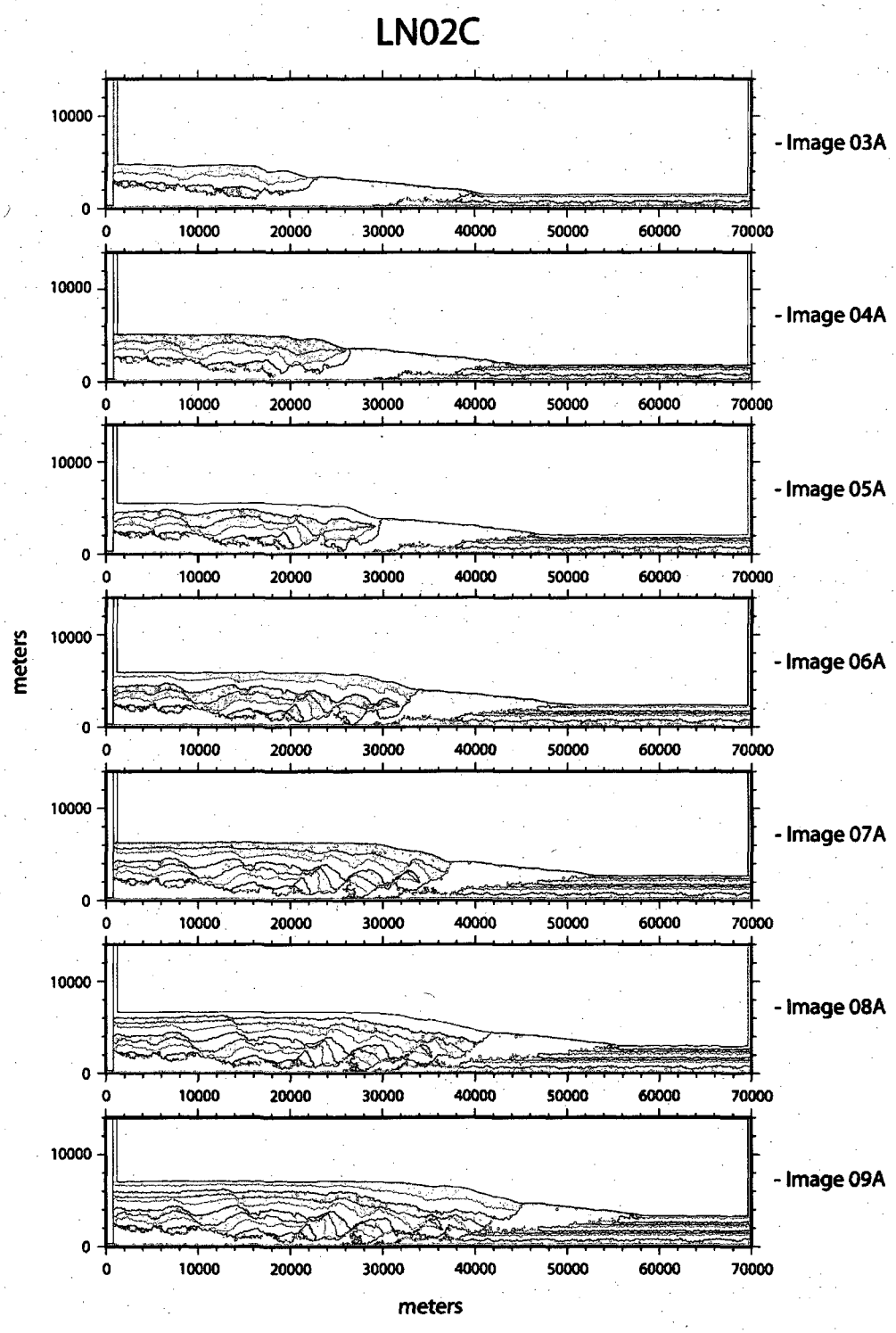

Figure A-2: Time progressive snapshots of the high sediment thickness model LN02C

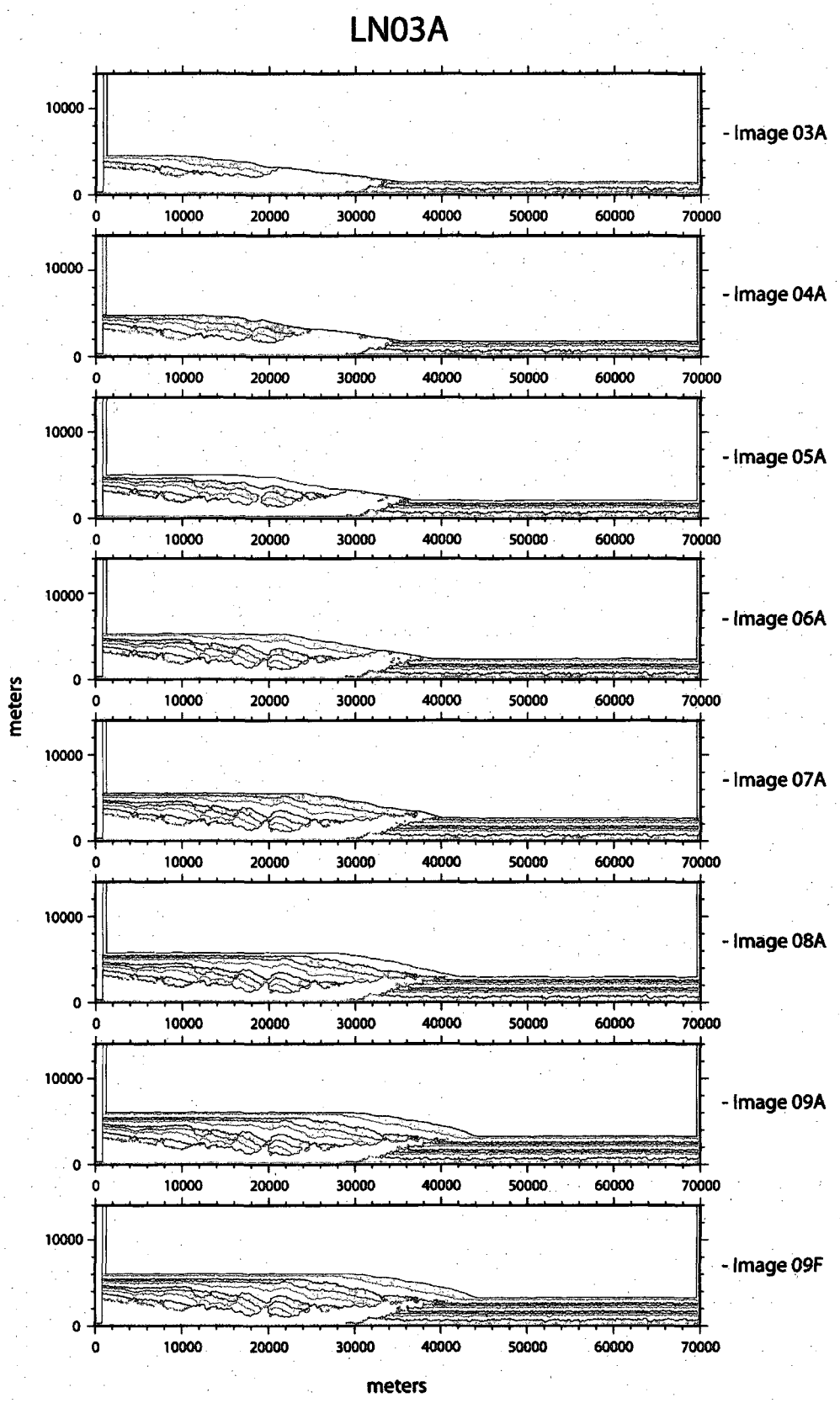

Figure A-3: Time progressive snapshots of the low basal slope model LN03A

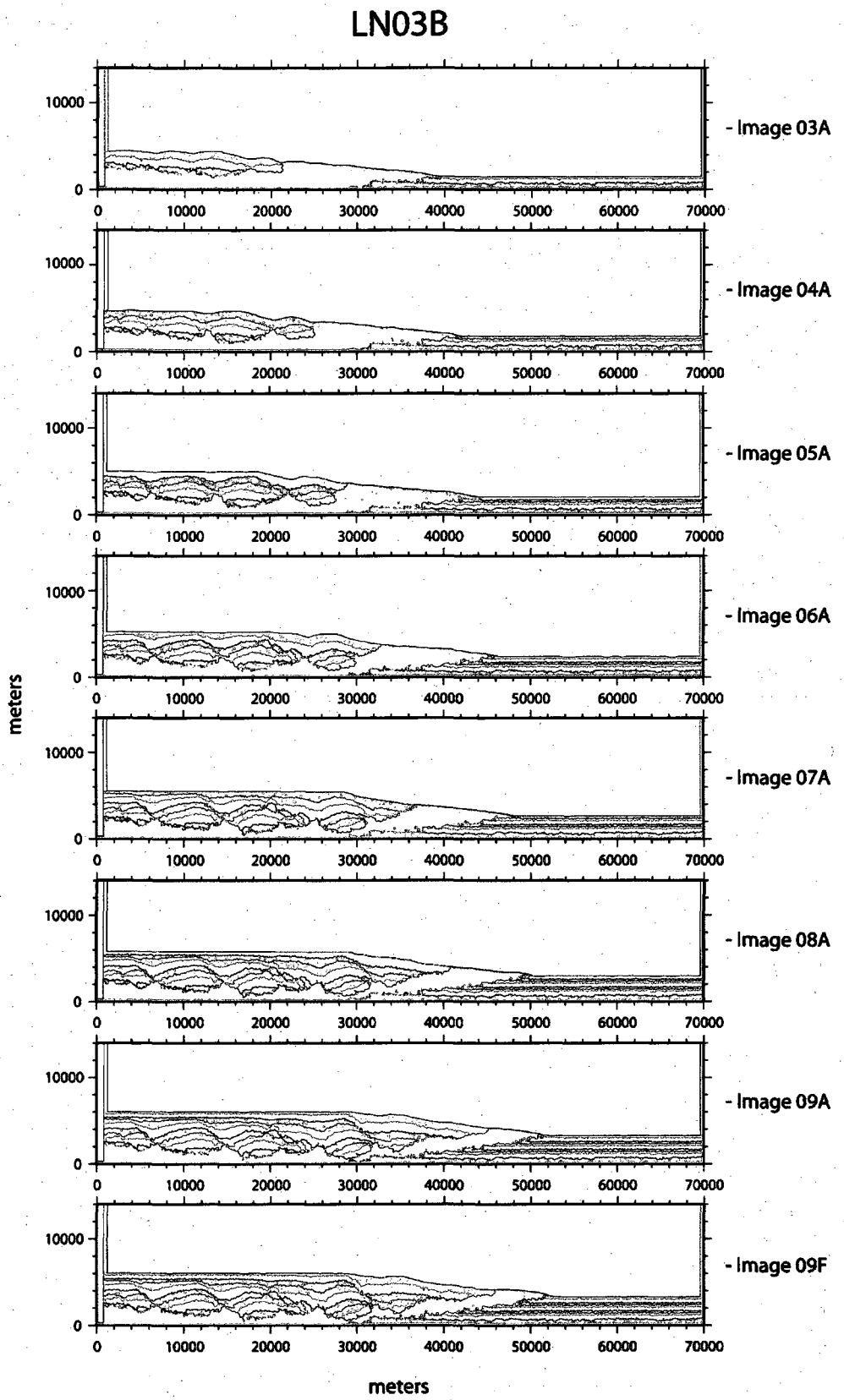

Figure A-4: Time progressive snapshots of the base model LN03B

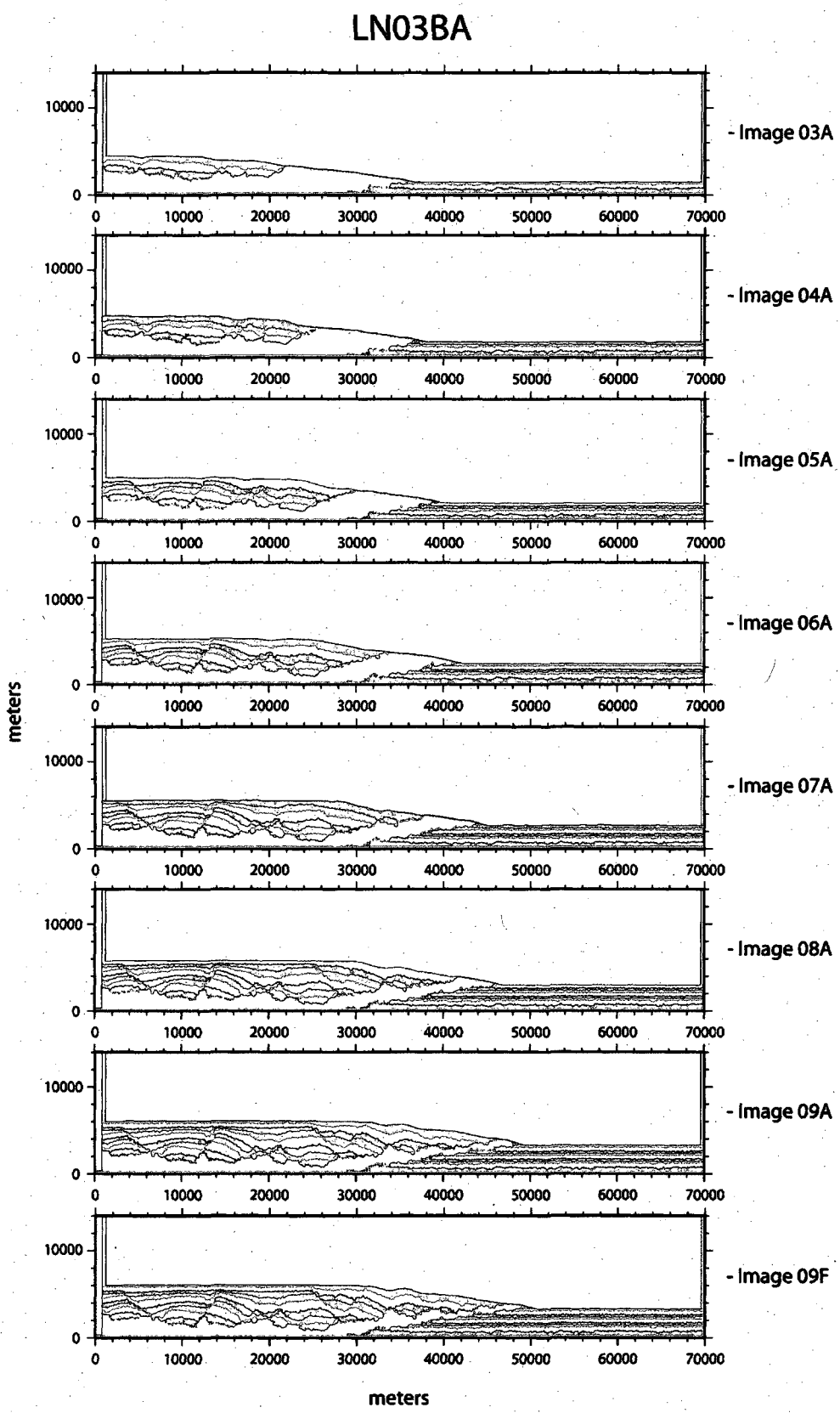

Figure A-5: Time progressive snapshots of the short loading time model LN03BA

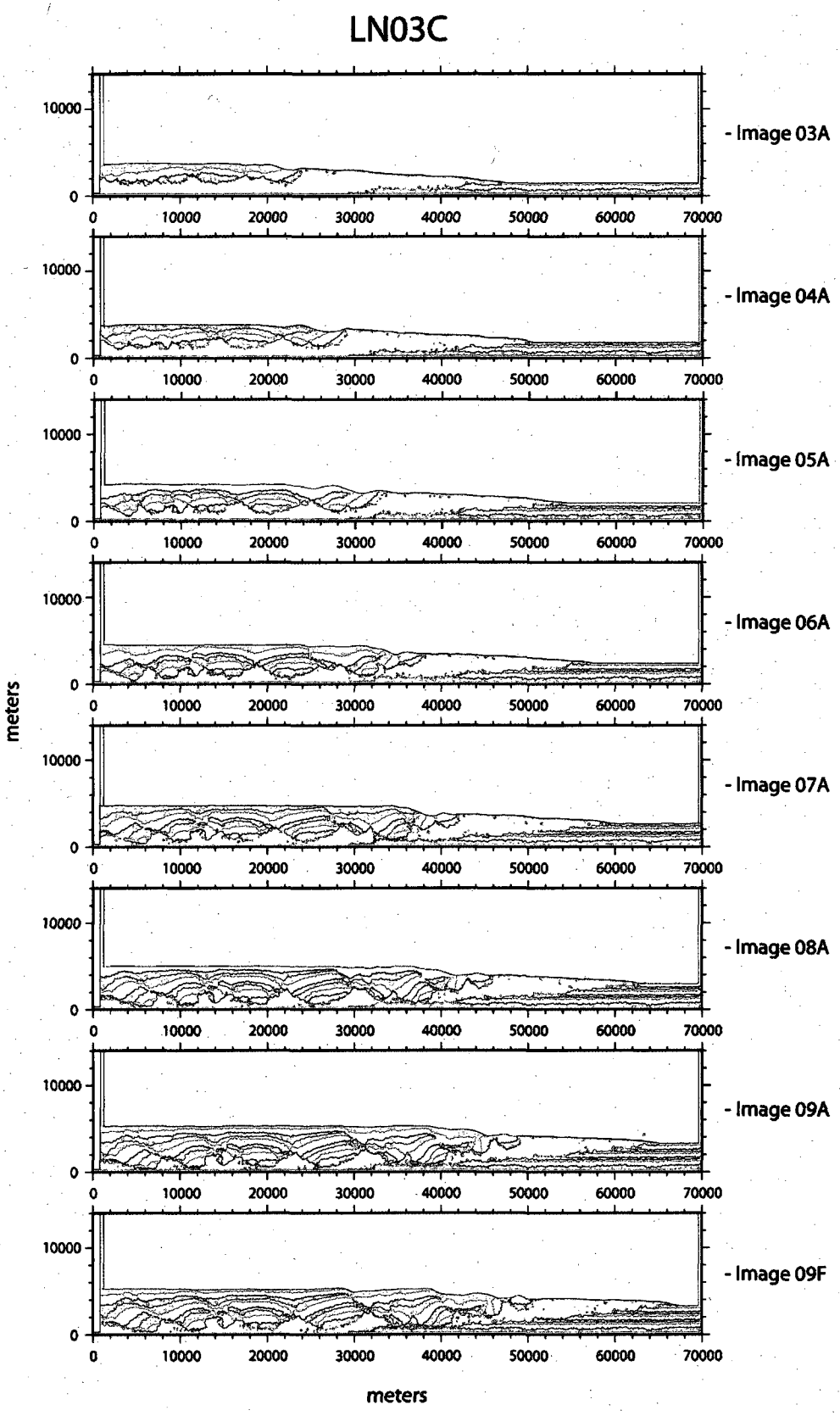

Figure A-6: Time progressive snapshots of the high basal slope model LN03C

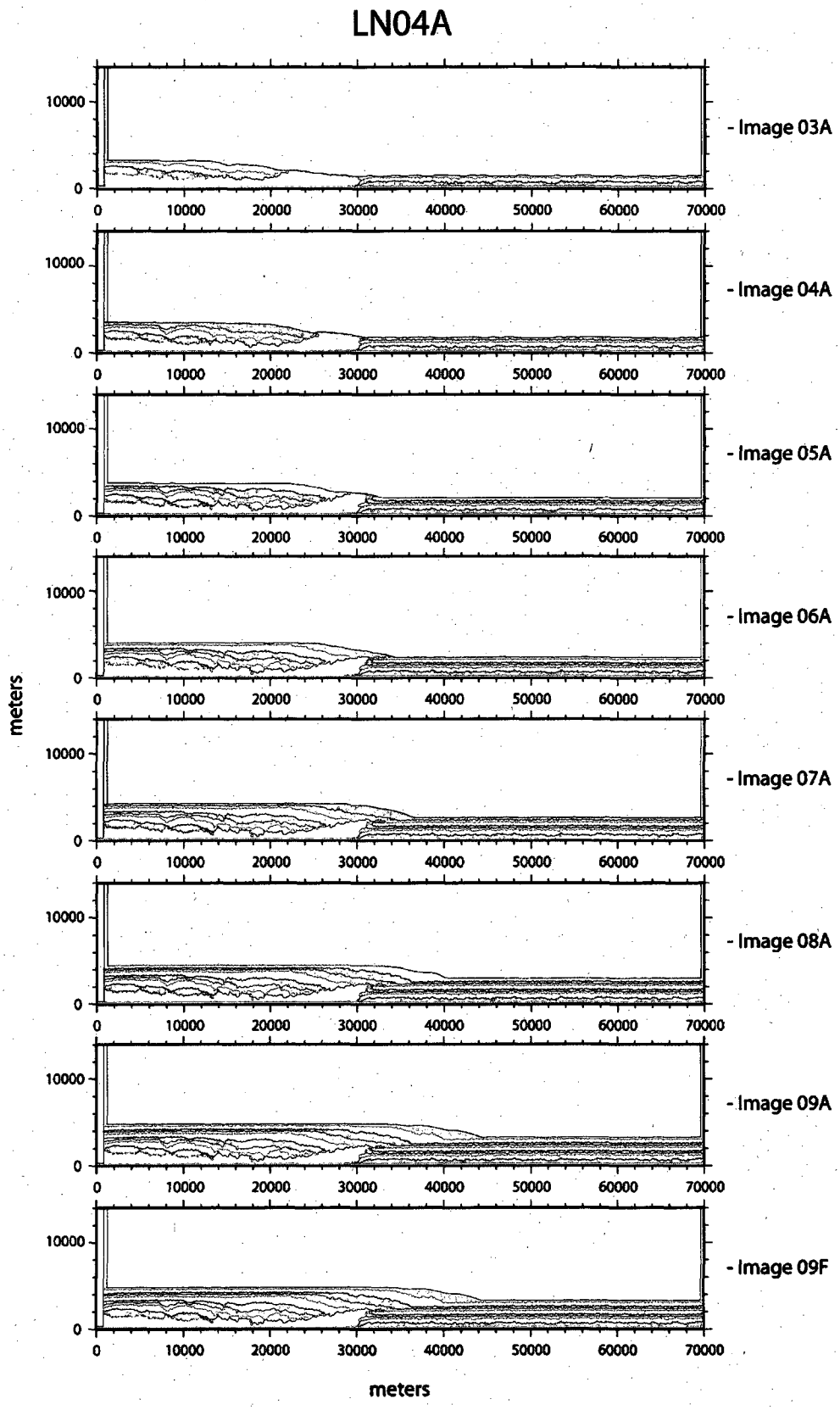

Figure A-7: Time progressive snapshots of the low initial salt thickness model LN04A

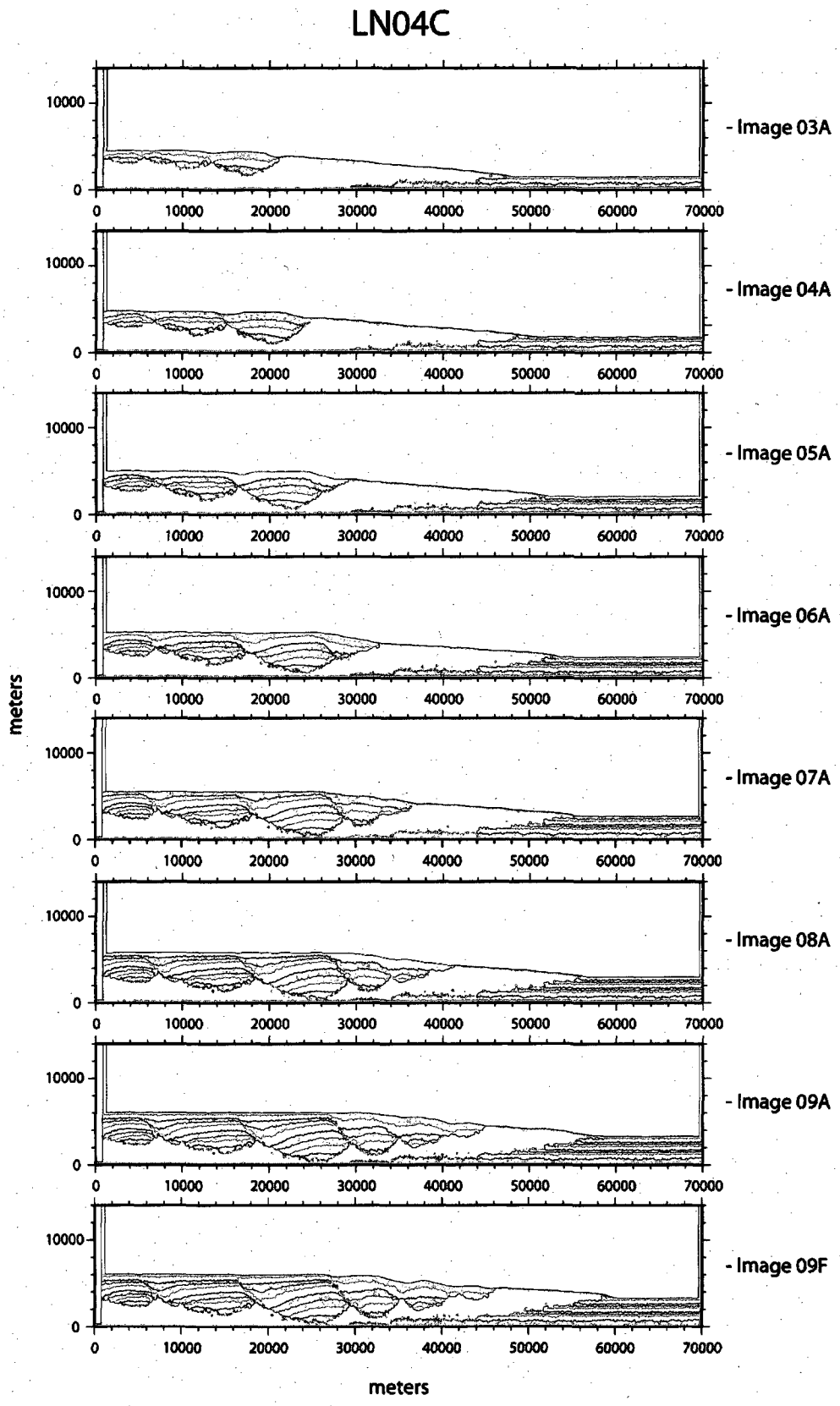

Figure A-8: Time progressive snapshots of the high initial salt thickness model LN04C

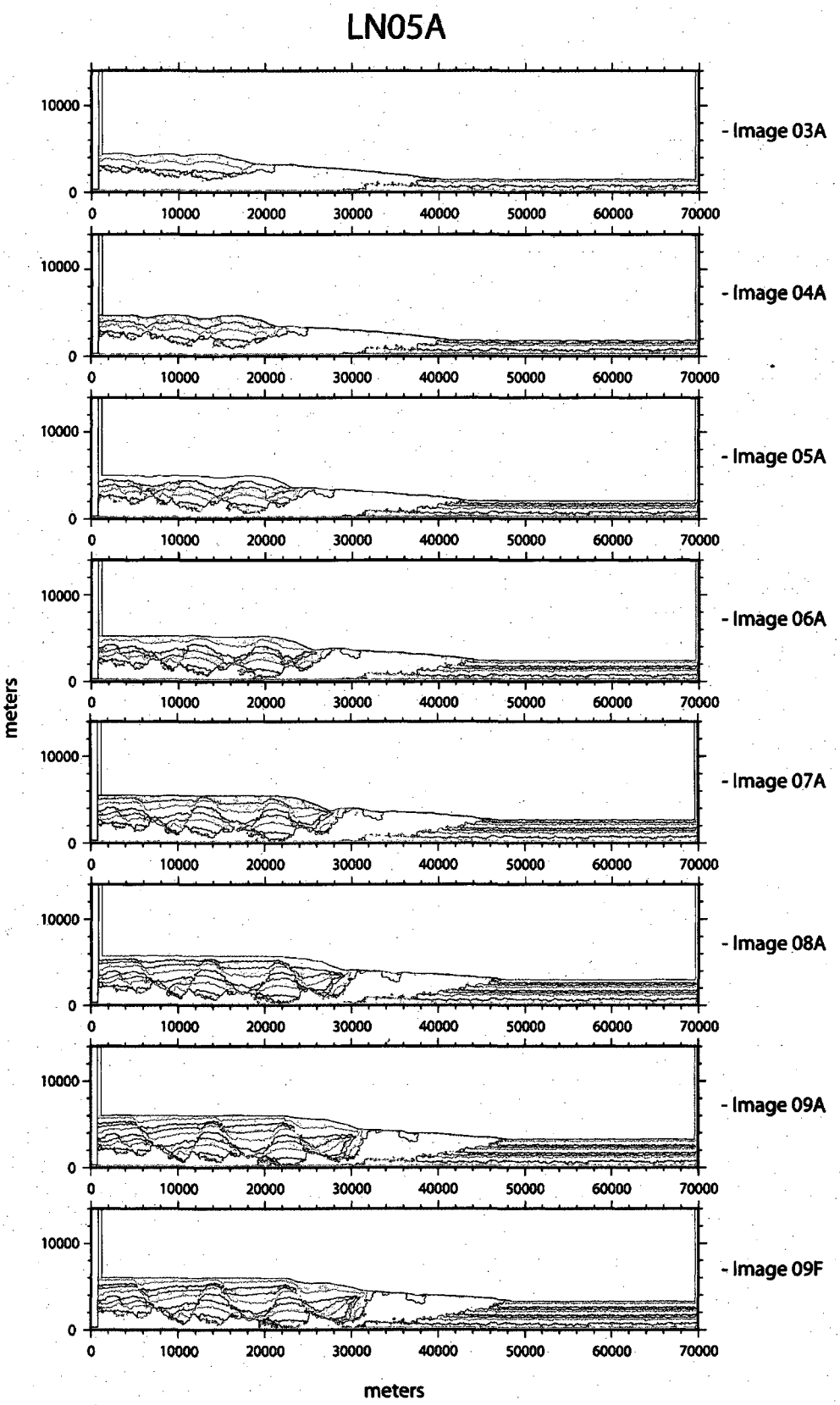

Figure A-9: Time progressive snapshots of the low progradation rate model LN05A

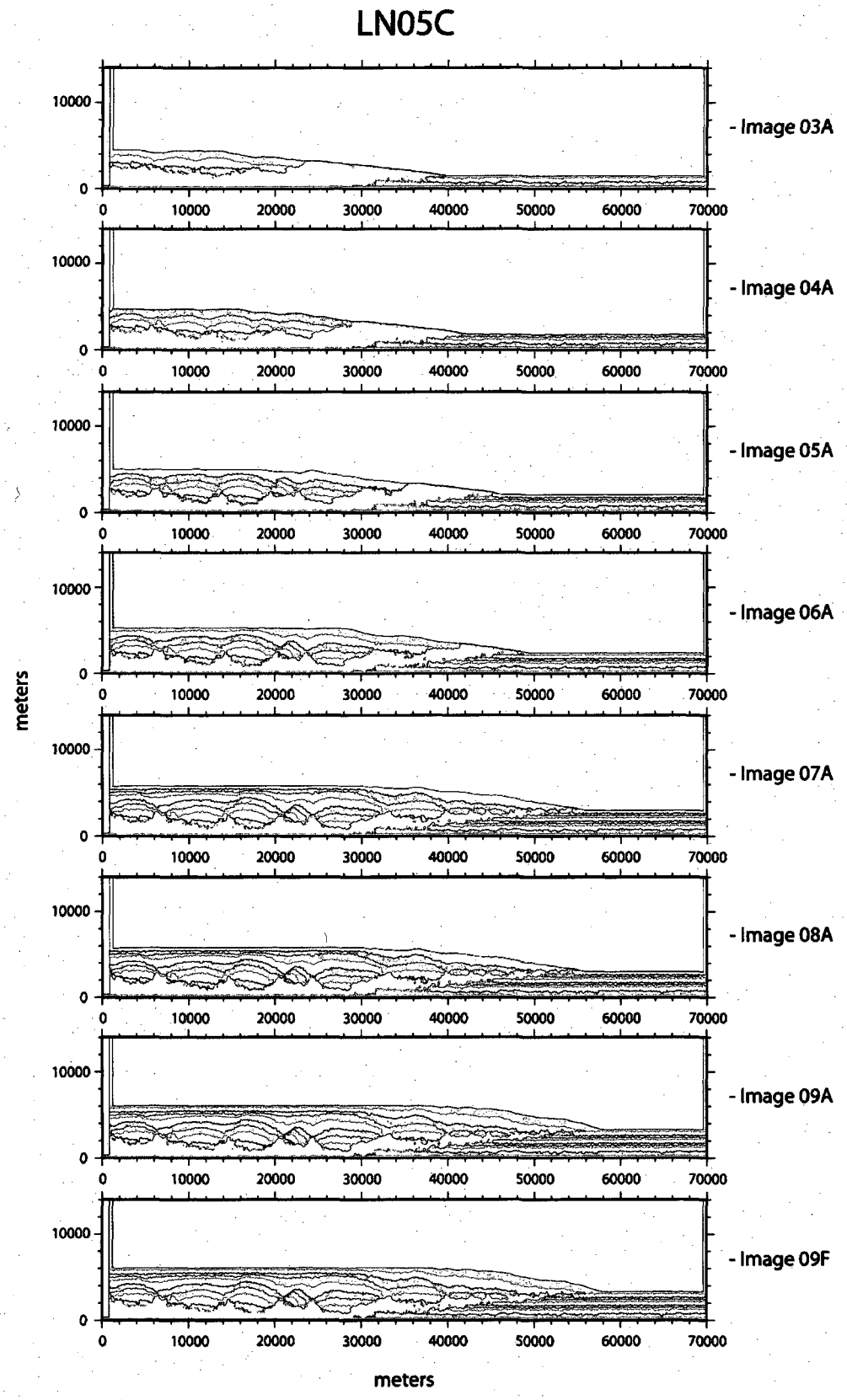

Figure A-10: Time progressive snapshots of the high progradation rate model LN05C

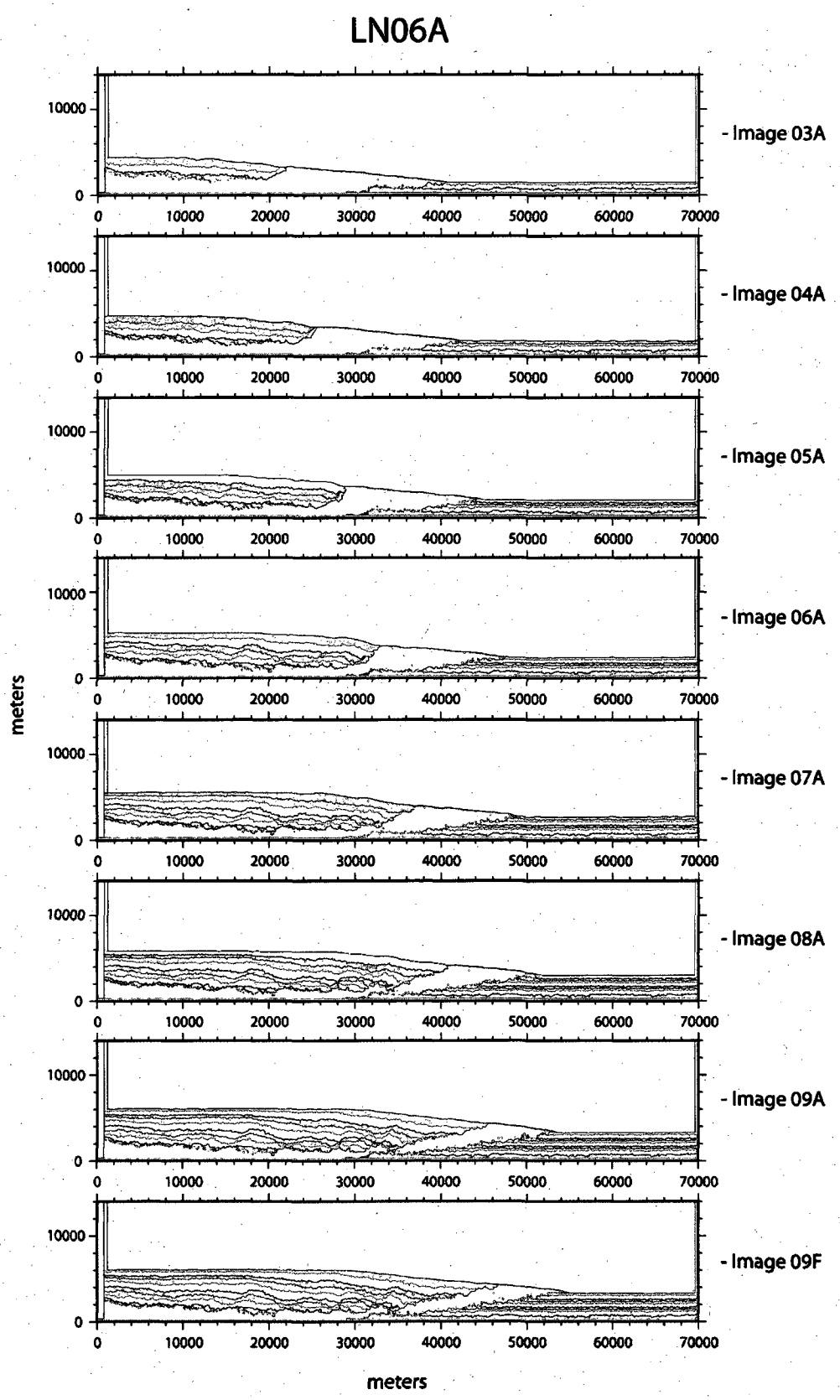

Figure A-11: Time progressive snapshots of the zero bonding model LN06A

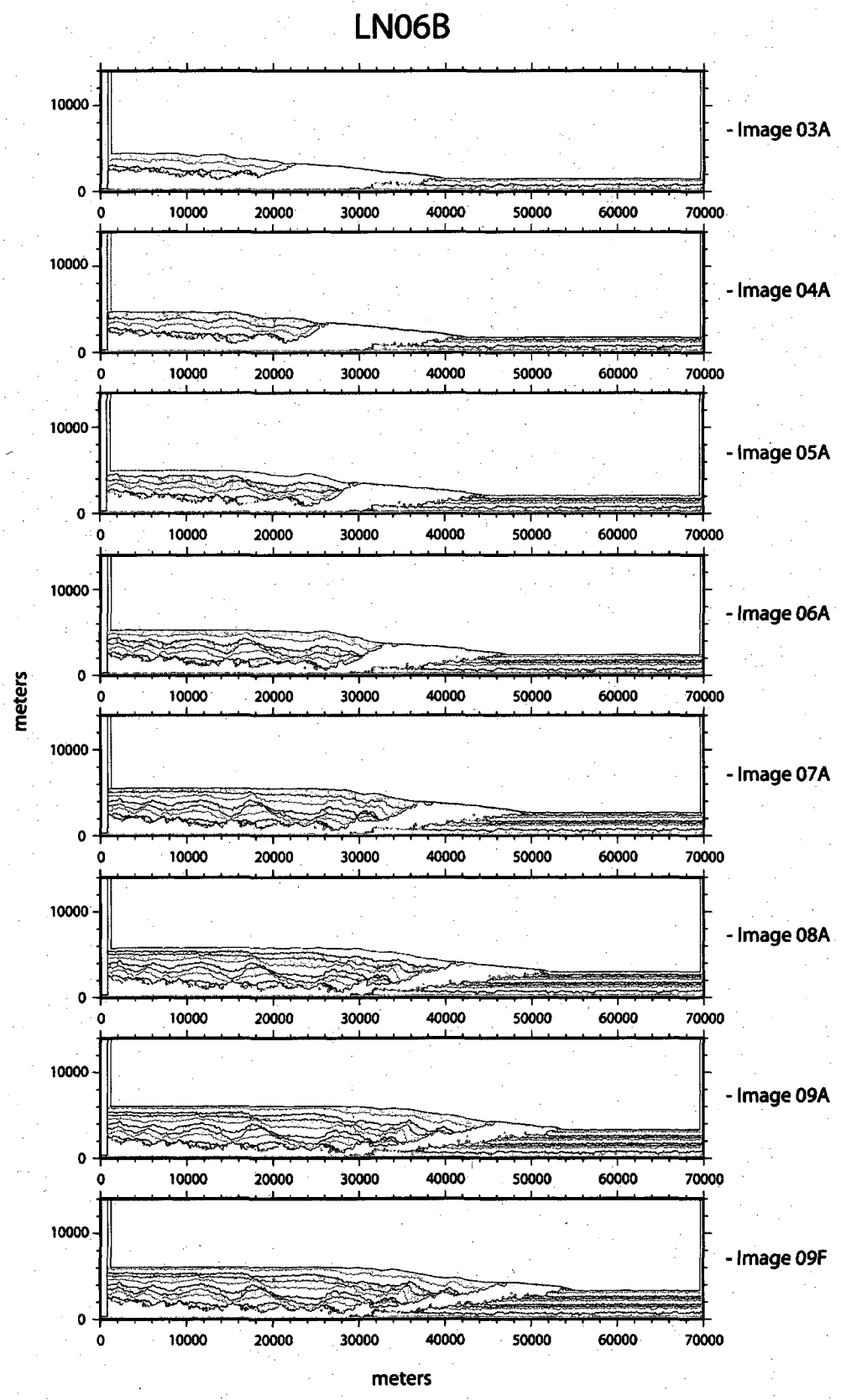

Figure A-12: Time progressive snapshots of the low sediment strength model LN06B

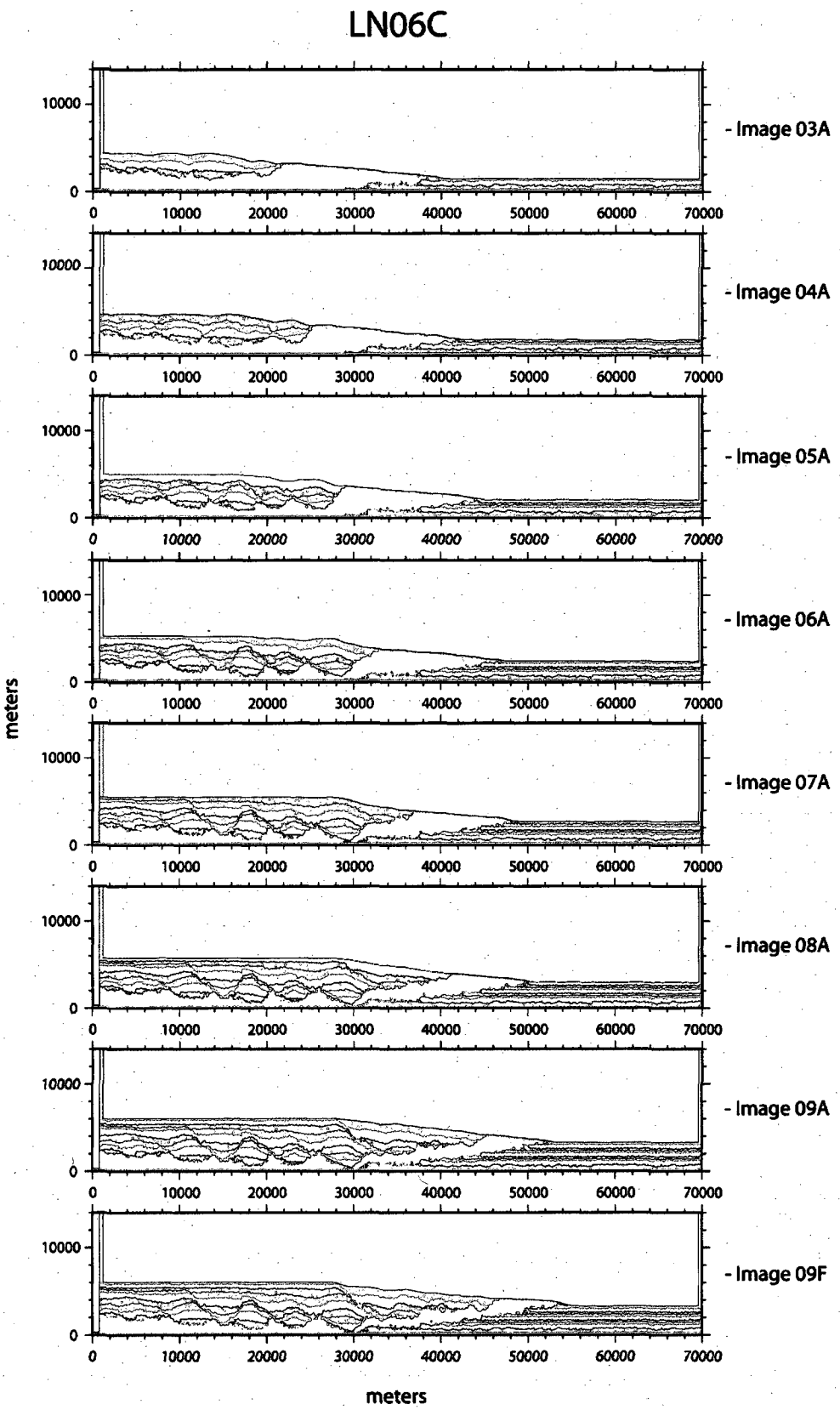

Figure A-13: Time progressive snapshots of the moderate sediment strength model LN06C.

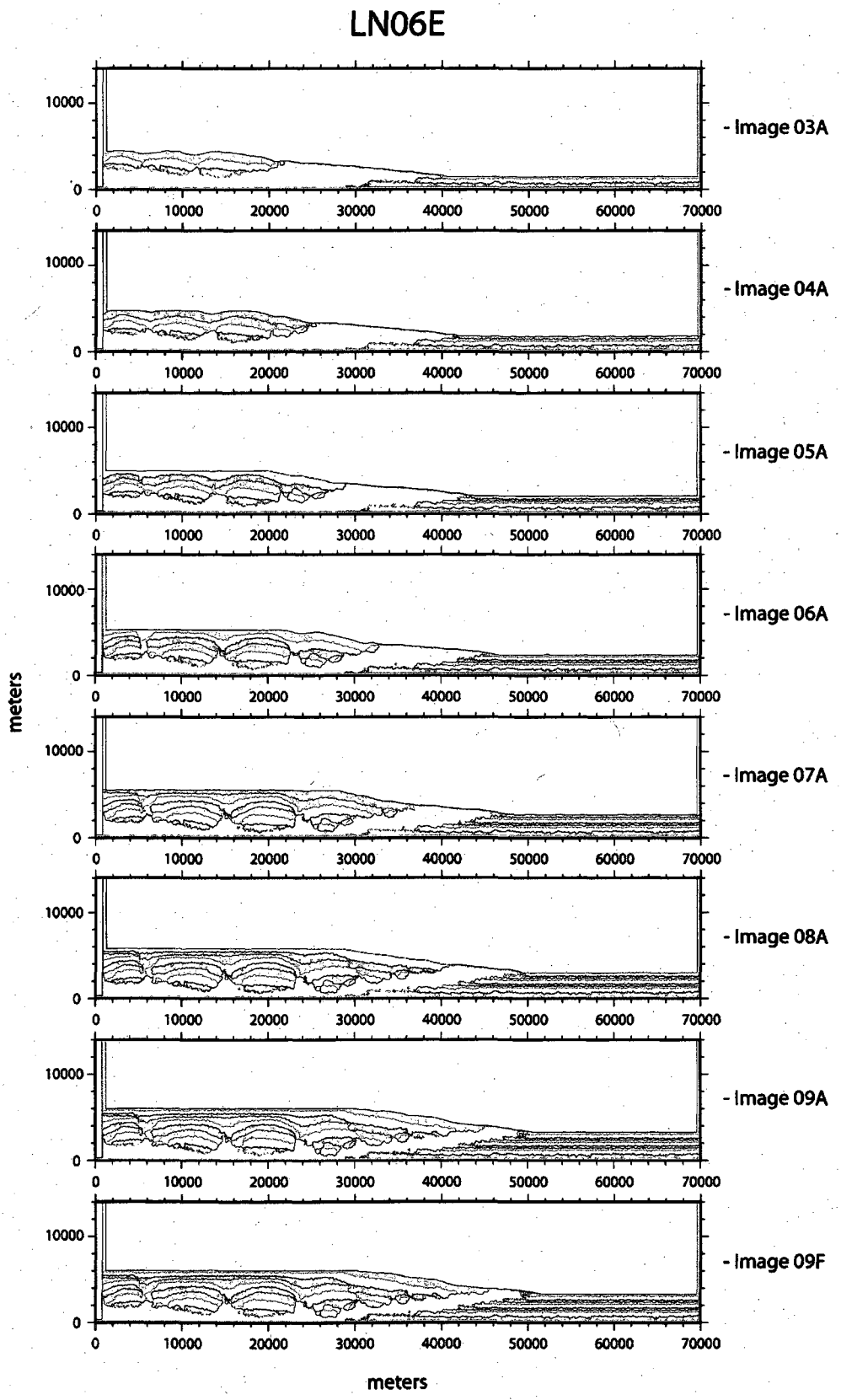

Figure A-14: Time progressive snapshots of the high sediment strength model LN06E

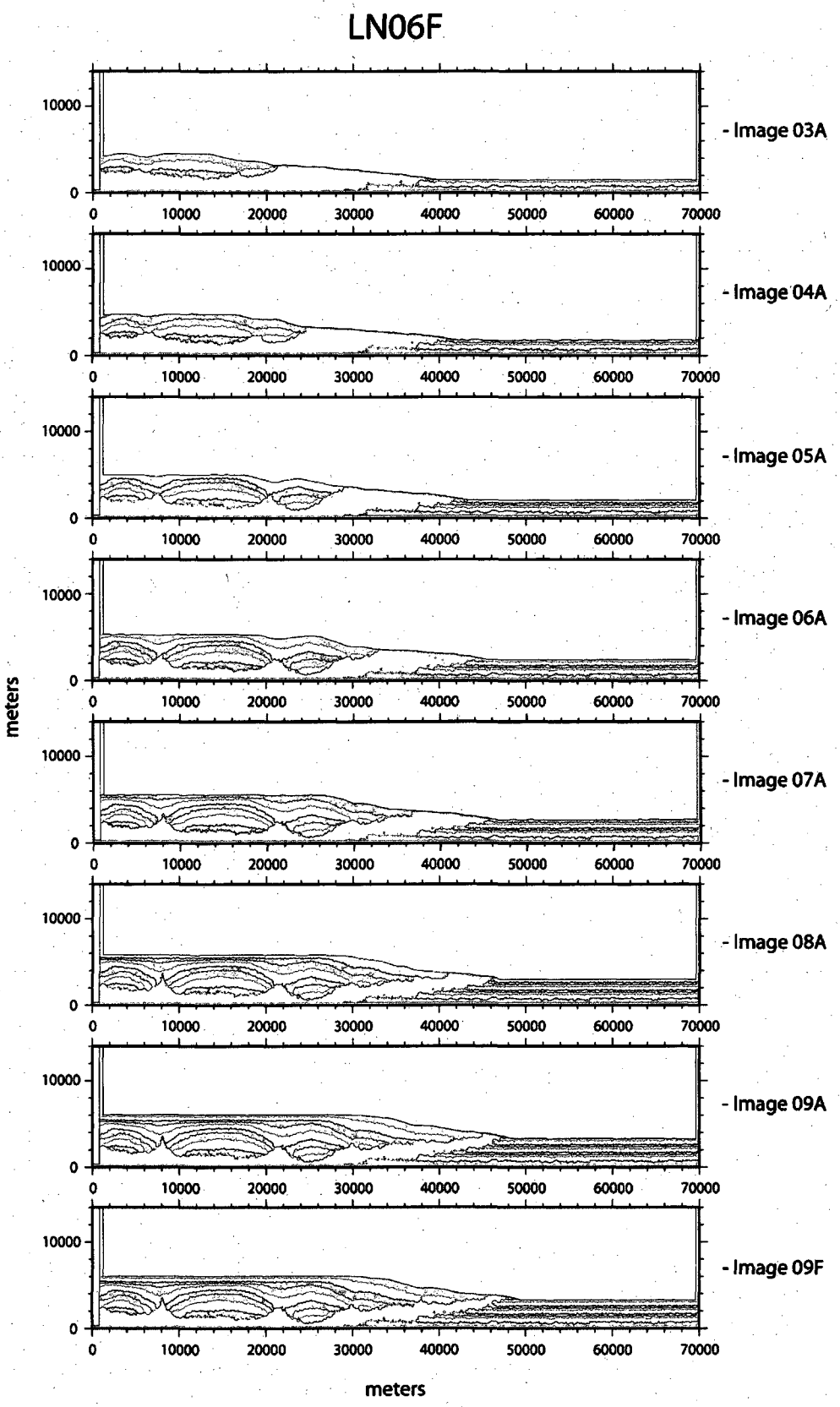

Figure A-15: Time progressive snapshots of the highest sediment strength model LN06F

Appendix B: Numerical Rocksalt Calibration

INTRODUCTION

Salt can be modeled as a viscous material, with negligible yield strength on geologic timescales (Jackson and Talbot, 1986). From laboratory experiments in compression (Carter et al., 1993), rocksalt flow has been approximated by the generalized viscous power-law equation of:

$$\dot{\varepsilon} = A \exp(-Q/RT)\sigma^n;$$

where A is the activation energy, Q is a temperature sensitive material constant for the rate-limiting mechanism, R is the universal gas constant, T is the temperature, and σ is the applied stress. The rate limiting mechanism for salt flow varies for different temperatures, differential stresses, strain rates, and grain size (Carter et al, 1993, Spiers and Carter, 1998; Peach et al., 2001). At low strain rates, rocksalt flows by a complex mixture of edge and screw dislocations. As dislocation density increases during deformation, the distance between dislocation planes is reduced and "pile-ups" occur (Aubertin et al., 1991). This process results in strain hardening of the material. In order to overcome these dislocation blockages, recovery mechanisms (i.e. edge dislocation climb and cross-slip of screw dislocations) move vacancies to other planes/axes allowing dislocation movement to continue. Carter et al. (1993) found that the processes of edge climb and cross-slip are the rate limiting mechanisms at different stresses and strain rates and they occur at higher stresses and higher temperatures than edge and screw dislocations. At lower temperatures and strain rates, strain is dominated by fluid movement on grain boundaries (Carter et al, 1993, Spiers and Carter, 1998; Peach et al., 2001) and salt deforms through pressure solution and fluid assisted grain boundary

migration (van Keken et al, 1993, Peach et al., 2001). In other studies, the influence of water on grain boundaries has been found to effectively reduce the strength of natural rocksalt by a full order of magnitude (Ter Heege et al., 2005). The combination of these deformation mechanisms results in an overall viscosity of 10^{17} Pa·s to 10^{18} Pa·s for strain rates of 10^{-12} s^{-1} and temperatures of 50-200° C – those typical of salt sheets in the Gulf of Mexico (Jackson and Talbot, 1986; Spiers and Carter, 1998).

Based on the description above described, the true rheologic behavior of rocksalt can not be accurately modeled using the DEM code, which employs frictional granular interactions with minimal time-dependence. However, the numerical method involves some time-dependence, e.g., through energy damping terms and pairwise particle interactions that propagate through the system with time. Therefore, it is feasible to quantify the apparent viscosity of "granular" salt. The simulations run to relate the viscosity of the granular salt used in the allochthonous salt sheet experiments are summarized in the main body of this thesis. Results from those experiments showed that our granular salt had a viscosity of 10^{10} Pa·s to 10^{12} Pa·s at strain rates from 10^{-10} s^{-1} to 10^{-14} s^{-1}. In order to understand how other models parameters could be used to increase this viscosity a series of additional calibration tests were run, which are presented here.

ADDITIONAL SALT CALIBRATION TESTS

Calibration test were run to test the effect of friction, shear, and damping on the viscosity of salt. The calibration experiments were run with the same basic set-up as described in the main body of this thesis. For each parameter test, only one parameter was changed relative to the "reference" simulations presented in the main body of the test, in which friction was set to 0.00 particle shear modulus was 30 MPa and

interparticle damping was set to 0.1. Three or more simulations were carried out for each suite, in order to allow a reliable fit line to be determined to calculate the viscosity. The results are displayed below (Figure B-1, Figure B-2, and Figure B-3).

Contact Friction Variation

In the friction variation model suite the coefficient of friction was varied between values of 0.01 and 0.05. The coefficient of friction acts on each particle contact and is indirectly related to the internal angle of friction for the particle assemblage (e.g., Morgan, 2004). The results of these simulations are compared to the 30 MPa confining pressure reference simulations, which used a coefficient of friction of 0.00 (Figure 5, Figure B-1). The results show that a small increase in the coefficient of friction results in a moderate increase in the shear stress required to maintain an equivalent shear strain rate. This results in a small (<5%) increase in the viscosity, as indicated by the increased slope of the line.

Shear Modulus Variation

Results of tests using different values for shear modulus are displayed in Figure B-2. A simulation using a shear modulus of 300 MPa is compared to the reference model which had a shear modulus of 30 MPa. The shear modulus controls the stiffness of the particles. A greater shear modulus results in stiffer particles which do not as easily undergo elastic deformation as the particle assemblage flows. As shown in the results, greater stiffness causes an increase in the shear stress needed to deform the particle assemblage at a given strain rate. This effect also causes a 10 % average increase in the overall viscosity.

Viscous Damping Variation

Simulations with coefficients of viscous damping of 1 and 0.01 were carried out to complete the viscous damping variation model. Viscous damping dissipates the total energy of the system by slowing particle motions proportionally to particle velocity. The effect is a viscous drag; one effect of this damping is a terminal velocity for particles settling under gravity. Variations in viscous damping produce substantial changes in the viscosity of the particle assemblage shear stress at each strain rate (Figure B-3). With an order of magnitude increase in the coefficient of viscous damping there is a 100% increase in the viscosity.

DISCUSSION

Although all of these parameters had the effect of increasing the viscosity of the salt in the particle assemblage, they all also produce undesirable behavior of the salt, leading to their rejection for the salt sheet models. As explained in the Material Calibration section of the thesis, increasing interparticle friction or particle stiffness will enhance granular dilation and thus, the pressure dependence of strength; this is inconsistent with the incompressibility of salt (Carter et al., 1993). Furthermore, the changes in viscosity induced by these parameters are too small to effectively raise the viscosity to natural values. Viscous particle damping, however, produced a much greater effect on the salt viscosity and could be used as a mechanism to increase salt viscosity. Unfortunately, the viscous damping terms currently apply universally for all particles in the simulation. Thus, an increase in viscous particle damping used to increase the viscosity of salt to natural levels would also affect the behavior of the sediment particles, and in particular,

would slow the settling of sediment particles dramatically. This would result in an impractical number of timesteps needed to deposit sediment layers, resulting in amounts of computing time that were not available for this study. For this reason, the best combination of parameters was chosen to optimize the behavior of the entire system, as summarized for our reference model in the text.

CONCLUSION

Although variations of several particle and numerical parameters can effectively increase the viscosity of the salt particle assemblage tested in these experiments, the observed changes and effects on the rest of the assemblage are less than optimal. The salt particle assemblage was therefore used in its lower viscosity form and the sedimentation rate and run length were scaled appropriately.

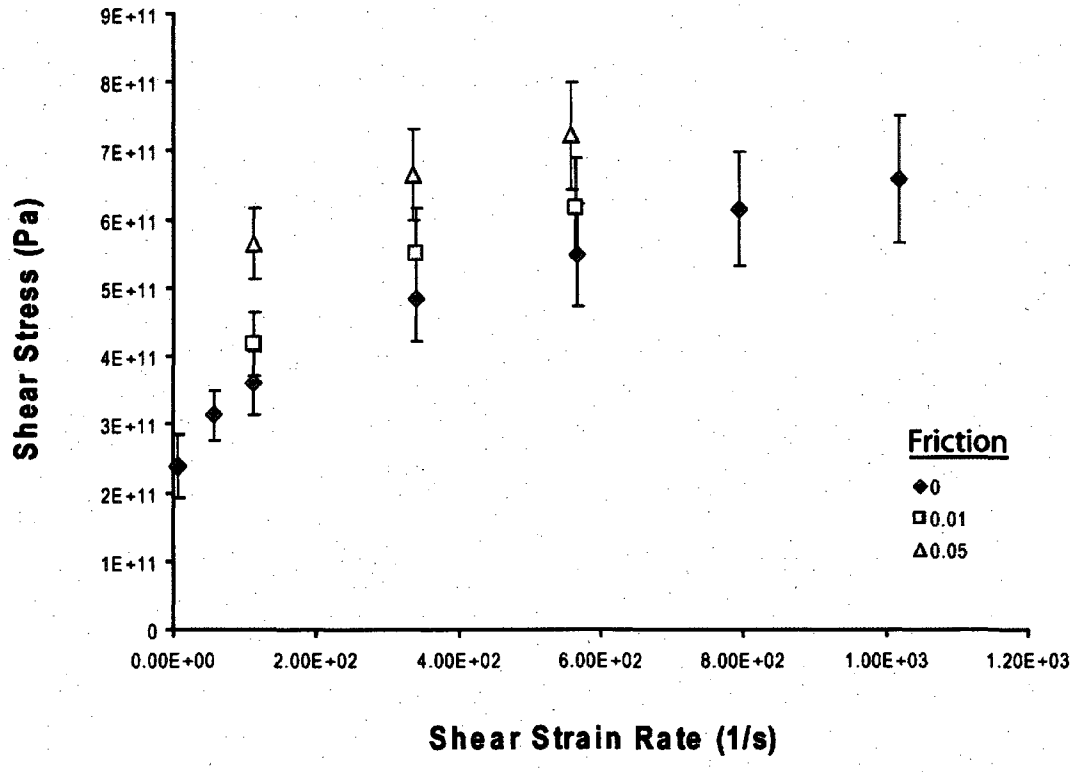

Figure B-1: Plot of effects of interparticle friction on shear strength. The best fit slope for each set of points defines the viscosity of the salt assemblage. Error bars are in black.

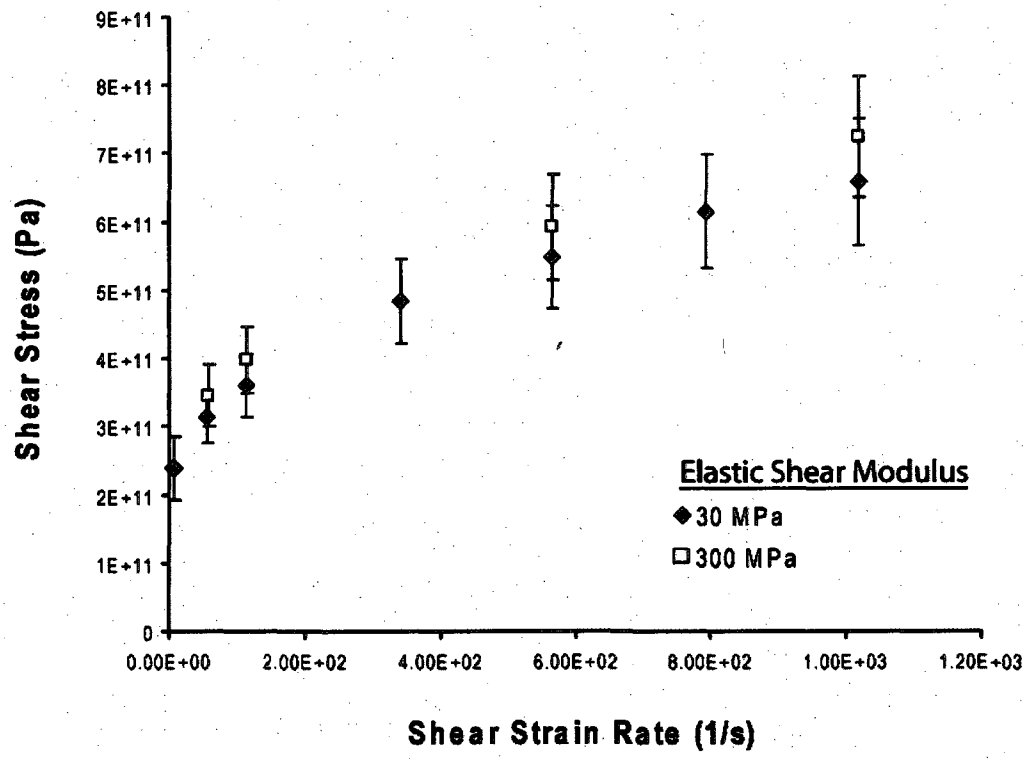

Figure B-2: Plot of effects of particle shear modulus on the assemblage shear stress. The best fit slope for each set of points defines the viscosity of the salt assemblage. Error bars are in blue and black.

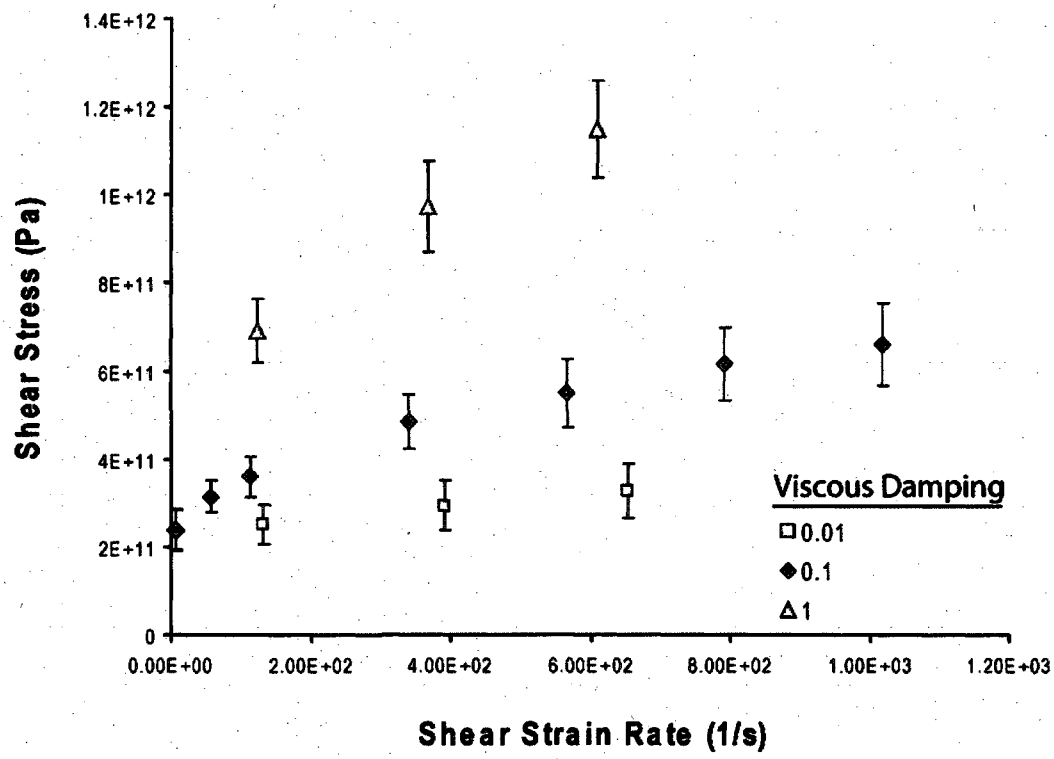

Figure B-3: Plot of effects of particle damping on the assemblage shear stress. The best fit slope for each set of points defines the viscosity of the salt assemblage. Error bars are in black.

Appendix C: Sediment Strength Calibration

The following graphs represent a more complete reporting of the sediment calibration experiments carried out to test the strength of the sediment particle assemblages used in the simulations described in the main body of this thesis. The majority of the experiments were carried out at the tensile strength of 1E7 MPa and the cohesive strength of 2E7 MPa. Samples at these bond strengths were consolidated at different confining pressures and then subject to the uniaxial compression described previously at a range of confining pressures. The results are displayed in Figure C-1. Because the 5MPa and 10MPa samples are representative of the pressures experienced by the particle assemblage in the salt sheet simulations a the time that they are bonded, the individual stress/strain paths are graphed in Figure C-2 and Figure C-3. In addition a series of experiments was also run using the bond strengths from the salt sheet sediment strength variation suite (LN06A-F, Figure 14). Samples were preconsolidated at 10 MPa and then subjected to compression at a range of confining pressure (0-100 Mpa). The results are displayed in Figure C-4.

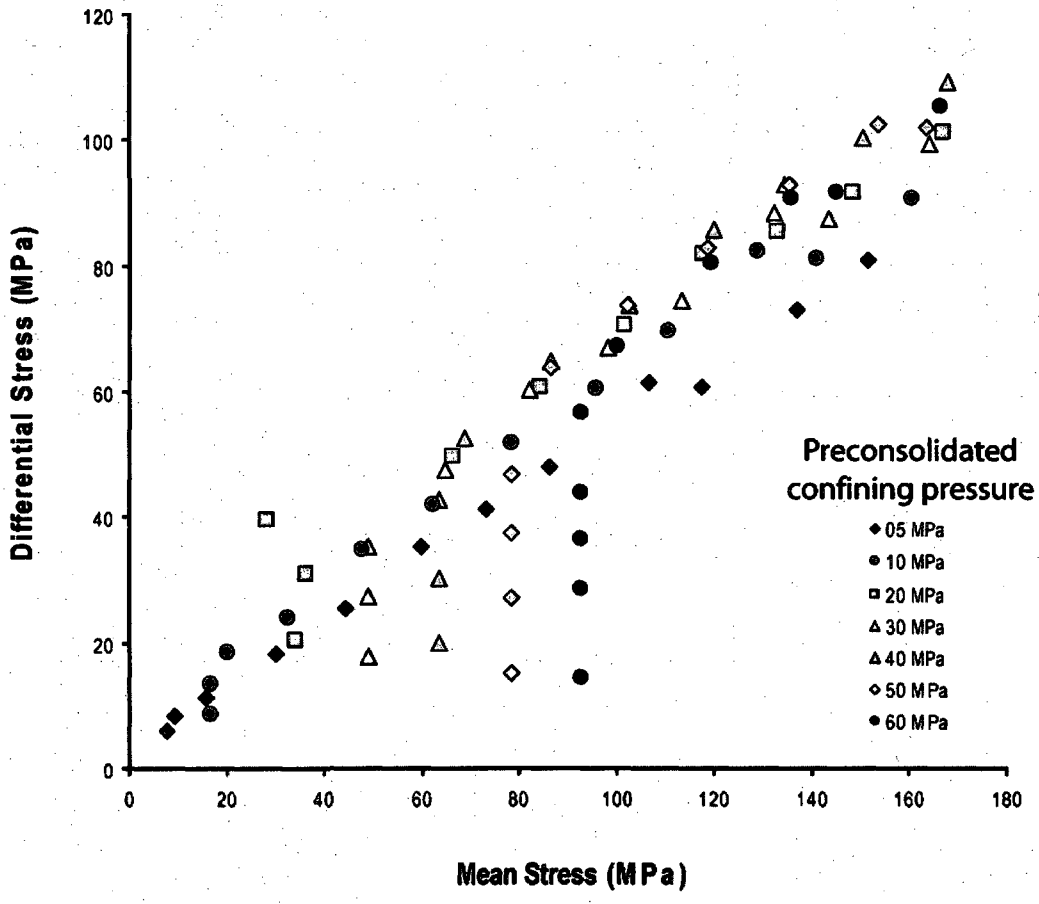

Figure C-1: Plot of differential stress at failure for samples tested under different confining pressures, for samples prepared under different preconsolidation stresses. Bond strengths for this suite are 10 MPa (tensile) and 20 MPa (cohesive).

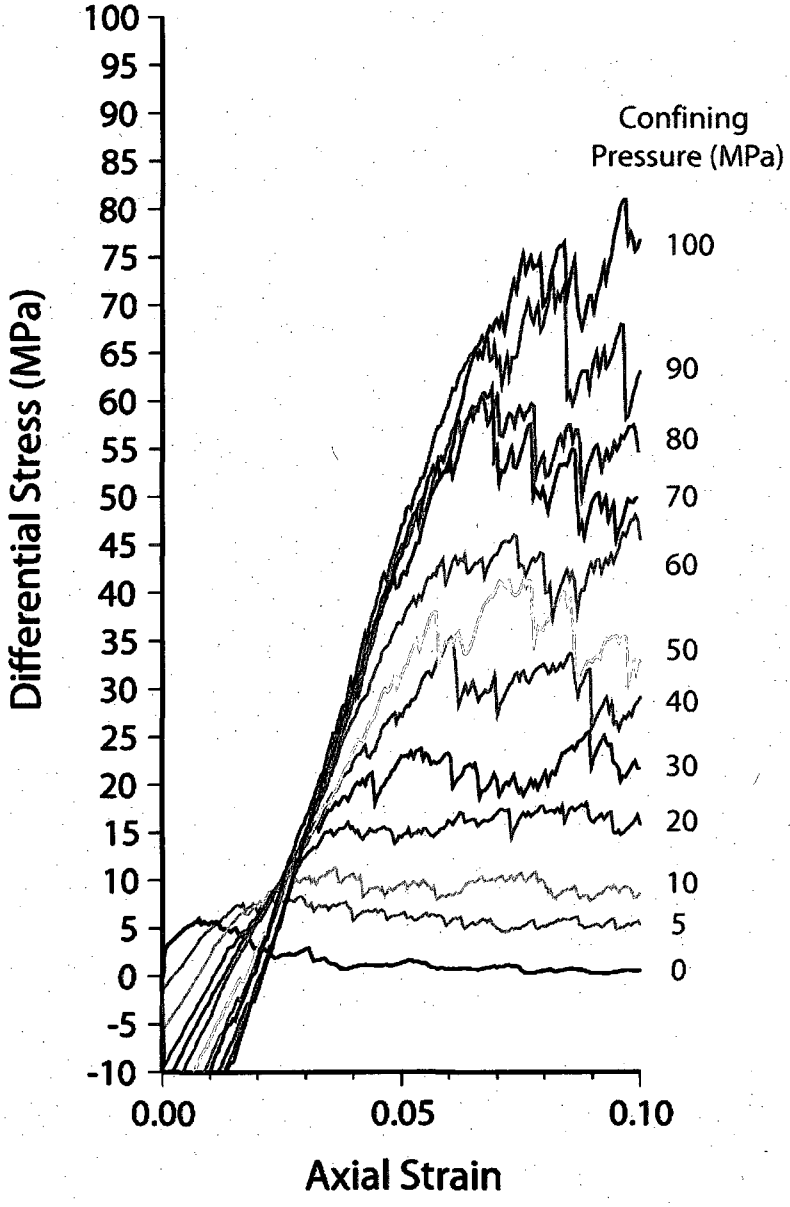

Figure C-2: Plot of differential stress against strain for biaxial failure tests for samples pre-consolidated to 5 MPa, and deformed under a range of confining pressures. Tests were carried out on assemblages with bond strengths of 10 MPa (tensile) and 20 MPa (cohesive)

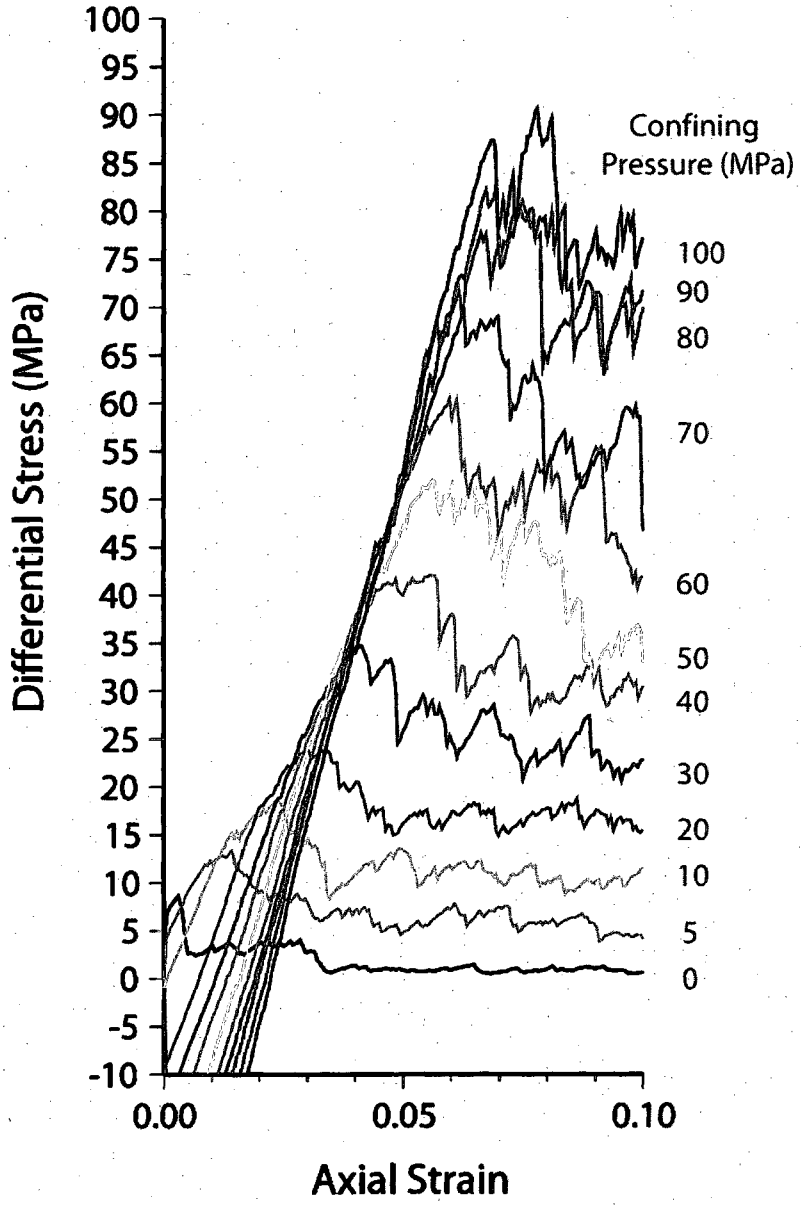

Figure C-3: Plot of differential stress against strain for biaxial failure tests for samples pre-consolidated to 10 MPa, and deformed under a range of confining pressures. Tests were carried out on assemblages with bond strengths of 10 MPa (tensile) and 20 MPa (cohesive).

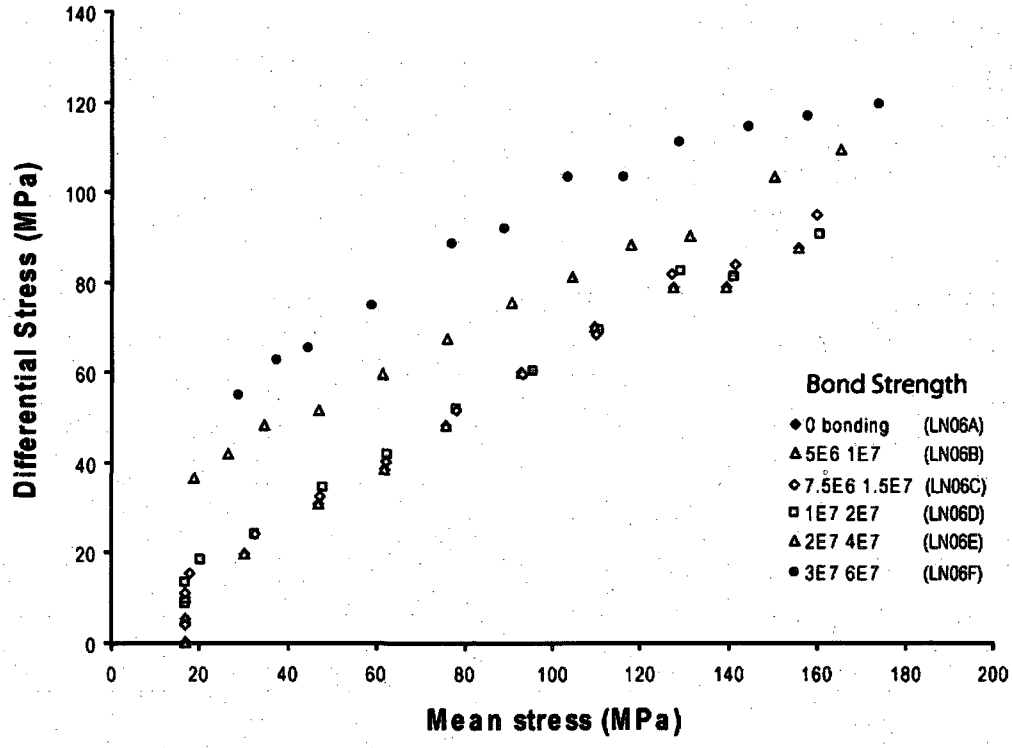

Figure C-4: Plot of differential stress at failure for samples tested under different confining pressures, for samples prepared with different bond strengths. All samples were pre-consolidated to 10 MPa. Samples correspond to sediment strength range represented in the LN06 suite of salt sheet simulations.

Appendix D: Physical Models

Physical models were run in connection with the numerical models described in the main body of this thesis. These models were run to serve as a reference for the numerical models, and designed after previous physical models carried out to explore the deformation styles of sediment layers above evacuating salt (e.g., Vendeville and Jackson, 1992a, 1992b; Cotton and Koyi, 2000; Fort et al, 2004; Talbot and Aftabi, 2004; Rowan and Vendeville, 2006; Brun, and Mauduit, 2009)

EXPERIMENT SET-UP

Experiments were carried out in a 75x30 cm box with glass sides (Figure D-1). Sand was used to represent overburden sediments, and Sport Look "Extreme Hold" styling gel (SLEH) was used to represent the allochthonous salt sheet. SLEH was chosen because it scaled similarly to the SGM 36 silicone gel used by previous studies to model salt as a viscous fluid (Table D-1) (Vendeville and Jackson, 1992a, b; Cotton and Koyi, 2000; Fort et al., 2004). Several problems exist with SLEH gel, such as: its relatively rapid evaporation rate and its slightly lower viscosity than SGM 36. However, the time scale of our experiment makes the evaporation rate negligible and the viscosity difference is small enough to be ignored. The gel also contains air bubbles that may affect the viscosity of the material. However, since they are almost uniformly distributed the effect should be negligible.

Each run began with the same basic setup. A 1.5 cm thick layer of gel was poured into a 40x30x1.5 cm section of the model box, buttressed on the right (downslope) by a clear acrylic plate. The box was tilted at an angle of 5 ° to represent common continental slope environments (Figure D-1) (Anderson et al., 2004). Sand was then added

incrementally in a series of 1 cm thick layers. Each layer was also accompanied by a thin (<2mm) covering of the same sand over the entire region of the model to fill in any accommodation space that had been formed by the evacuating gel. Thin, alternating, green and orange sand layers were used to distinguish between successive layers.

Sedimentation rate was the only variable that changed between the two runs. The models were run for the same amount of time (3 days) but sand was laid down every three hours in the high sedimentation rate model and every six hours in the low sedimentation model. Progradation was held constant in both model runs at a rate of 0.33 cm/hr. In theory, increased sedimentation should create greater roof strength and cause the system to favor counterregional salt expulsion systems (Hudec and Jackson, 2006). The models were photographed every three hours before and after sediment deposition. The results of each run are discussed below.

RESULTS

High Sedimentation Rate

The result of the high sedimentation rate model is shown in Figure D-2 and Figure D-3. Salt evacuation accelerated quickly under the first depositional load, although salt movement began when the domain was tilted to 5 °. Overburden deformation developed initially as an extensional horst and graben system. With continuing sedimentation, extensional deformation concentrated on the up-dip fault of each graben creating listric growth faults. This zone of extension started at the back of the overburden and progressively migrated downslope (Figure D-2). Migration was triggered by the evacuation of gel from beneath the extending portions of the overburden, thereby, creating a weld (Figure D-3). Extensional deformation became increasingly dominated by

a large central graben that developed during the second day of the model run. Extension on this graben ceased during day 3 after the sediment overburden had prograded over the toe of the rising salt diapir.

In the compressional zone, at the down-dip edge of the gel layer, deformation began as small wrinkles and expanded into larger wavelength folds with increasing sediment thickness, creating biharmonic folding. As the gel layer flowed downslope it pushed these folds upward into a large diapir that continued to grow until it was buried by the advancing sediment layers. The diapir formed because the layers of sand on the downslope acrylic plate created a high angle ramp. The steepness of the ramp slowed gel evacuation and forced it upwards into a diapir which rose passively with the sedimentation of each sand layer. The burial of the diapir stopped gel evacuation from below the overburden and extension in the up-dip graben.

Low Sedimentation Rate

Lowering the sedimentation rate resulted in a significant change in the style of overburden deformation. The model progression is shown in Figure D-4. The overburden began deforming similarly to the high sedimentation rate model but the listric growth faults were spaced at greater intervals. As the model progressed, these growth faults continued to develop and extension was completely confined to them. The zone of extension did not propagate downslope and grabens never developed. There was also less expulsion of the gel layer. The zone of compression formed in a similar manner to the high sedimentation rate model but the gel was able to push over the top of the acrylic plate. The advance of gel can be tracked by observing the up-dip cut offs of the sediment layers on top of the plate. As the gel began to move up the low angle ramp created by

these layer cutoffs, a new zone of extension formed above this portion of the sheet. The accommodation space created in this zone was filled in by the prograding sediments. Deformation continued in this region even after the allotted three days for the model run. On the opposite side of the modeling box, the gel layer advanced by folding the sand layers and rolling them over in a "tank-tread" manner. This type of advance is observable in salt glaciers around the world and in the analogue models of Talbot and Aftabi (2004).

DISCUSSION

The results of these models were similar in structure to the models of Fort et al. (2004) who observed large grabens at high sedimentation rates and listric growth faults with salt rollers at low sedimentation rates. The listric growth faults of the low sedimentation rate model match the general model for a roho geometries presented in the main body of this thesis. A counterregional system began to develop in the high sedimentation rate model but never fully developed. Low sedimentation rates resulted in a slightly greater amount of overburden extension than the high sedimentation rate model. The total volume of gel extruded in each case was similar although the final geometries were quite different. These results appear to match the hypotheses of Hudec and Jackson (2006) who predicted that lower sedimentation rates should result in roho systems and that high sedimentation rates should create counterregional systems.

The counterregional system did not develop completely because the gel diapir was buried by the advance of the prograding sediment layers. In nature, diapirs enter an active stage of growth (Rowan et al., 2004) and break through their roofs before continuing to grow passively. This did not happen in our model because the sand that touched the SLEH gel layer absorbed small amounts of water which formed a strong cap to the diapir.

This same phenomenon was observed in the second model as the extending allochthonous sheet was unable to break through the thin sand overburden and flow downslope in open-toe advance. Because of this "cap rock" on the head of the diapir, it was unable to continuing growing and the sediment layers were unable to subsidence. If the layers near the base of the diapir had continued to subside a counterregional geometry would have most likely formed as gel was expulsed up the diapir.

These results are somewhat dissimilar to the numerical model results presented in the main body of this thesis. The thick sediment numerical model (LN02C) produced greater overburden extension and a lower ramp angle than the thin sediment numerical model (LN02A) (Figure 12). The low ramp angle allowed the simulation to develop expulsion rollover geometry similar to those found in the Santos Basin, offshore Brazil and in the physical models of Ge et al. (1997). The main difference between the physical and the numerical models is that the "abyssal plain" sedimentation in the numerical models was held constant. It was varied according to the sedimentation rate in the physical models. The high sedimentation rate physical model was, therefore, able to build a steep ramp angle because the sediment thickness was greater above the acrylic plate than in the low sedimentation rate physical model. The physical models were also run at higher basal angles (5 °) than the numerical sediment thickness model (2.5 °). The physical models also had a lower progradation rate (~2.5 km/my) than the numerical simulations (4 km/my). The combination of the lower progradation rate (which also resulted in an increased ramp angle in the numerical simulations) and the increased sedimentation over the acrylic plate resulted in a higher ramp angle and the initiation of a counterregional geometry.

CONCLUSION

Physical modeling with SLEH gel showed that a change in sedimentation rate above an allochthonous salt sheet can produce a change in the deformational styles of both the overlying sediment layers and the emergent salt geometries. In accordance with the hypotheses of Hudec and Jackson (2006) low sedimentation rates produced roho systems and high sedimentation rates initiated counterregional systems, although the counterregional sediment geometries never fully developed. The results differed from the numerical experiments presented in the main body of thesis because the rate of progradation was lower and the "abyssal plain" sedimentation was allowed to change in the physical models. This resulted in a steeper ramp angle for the high sedimentation rate physical model, allowing a counterregional system to initiate.

Table D-1: Scaling factors for physical models 1 and 2 of allochthonous salt sheets.

Density	kg/m^3		**Viscosity**	Pa*S		**Length**		
Sediment	2400		Salt	$1.7x10^{18}$		Nature	70 km	
Sand	1500		SLEH	$\sim 1.0x10^{4}$		Model	70 cm	
	ratio	0.6		ratio	6x10-15		ratio	$1x10^{-5}$
Density			**Time**					
Salt	2200		Nature	10 my				
SLEH	860		Model	3 days				
	ratio	0.4		ratio	1.0×10^{-4}			

Figure D-1: Picture of box used for both runs representing the initial configuration of SLEH. The box was tilted at a 5 degree angle and the SLEH gel was buttressed down slope by a 1.5 cm thick plate.

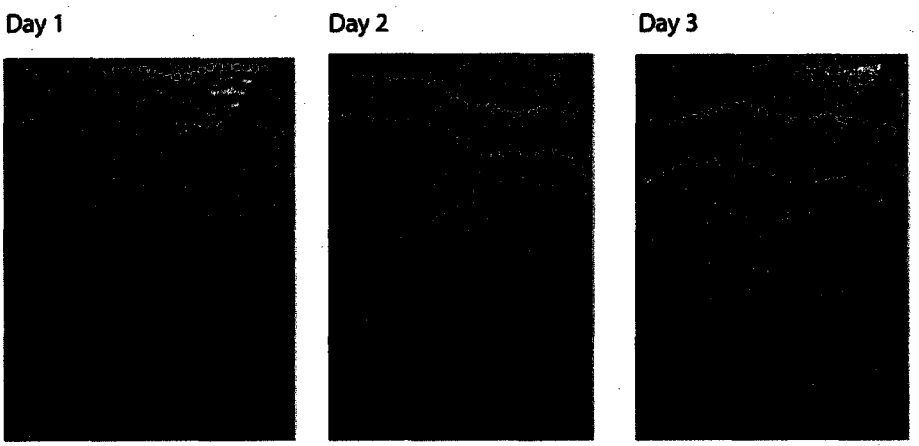

Figure D-2: Time progressive top-view photographs from each day of model 1 (left to right). Red dashed lines indicate the front of the zone of extension and the black lines represent the back of the zone.

Day 1

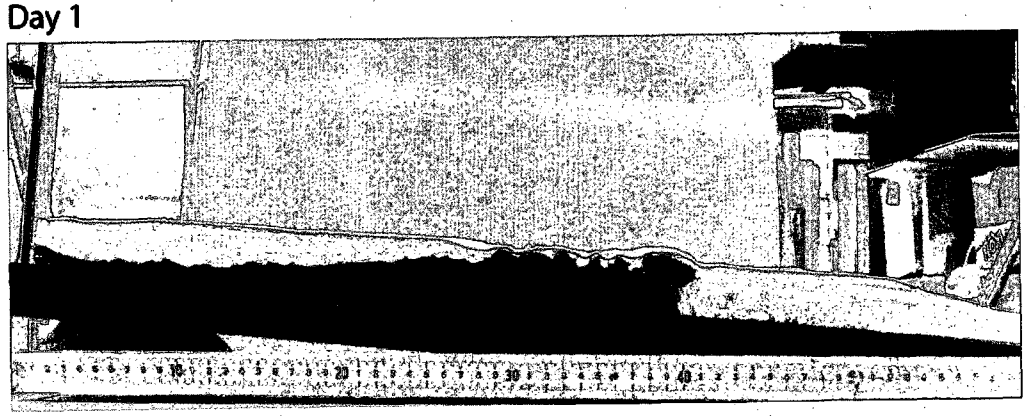

Day 2

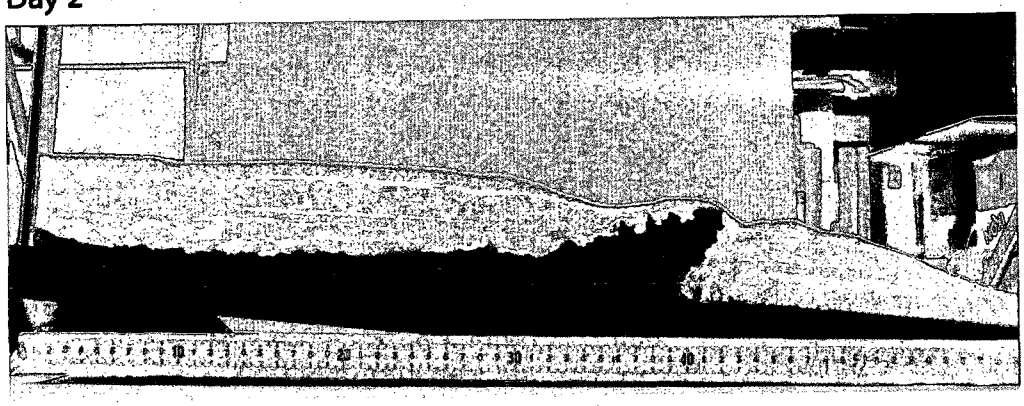

Day 3

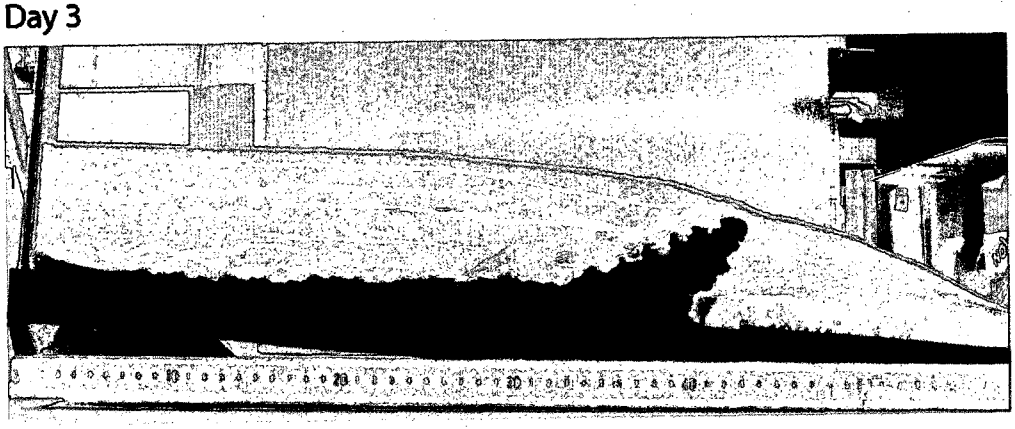

Figure D-3: Time progressive photographs of the high sedimentation rate mode (Model 1). Each photo represents one day of deformation. Bottom scale is in centimeters.

Day 1

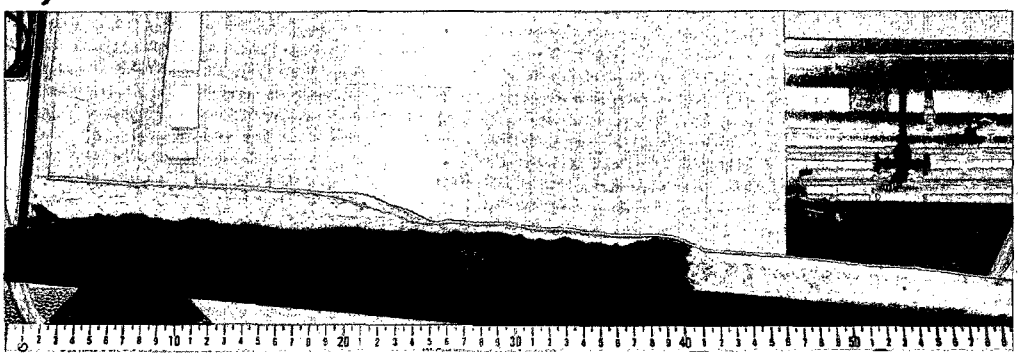

Day 2

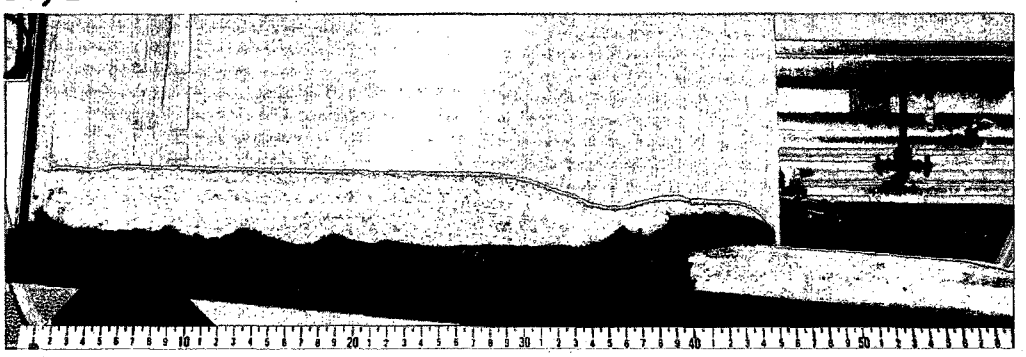

Day 3

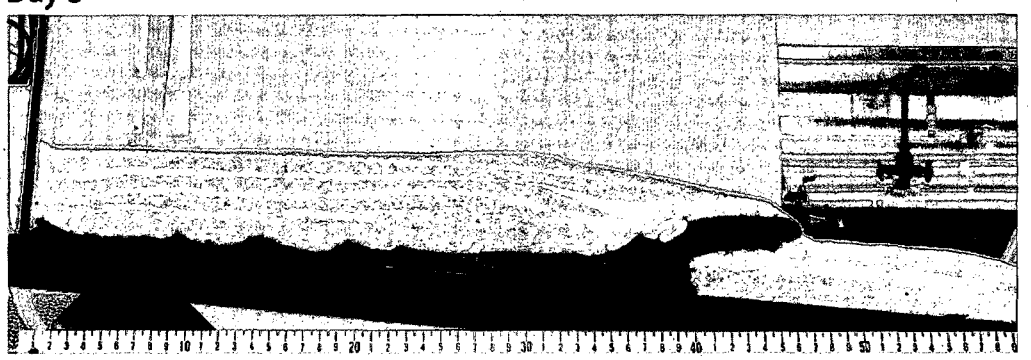

Figure D-4: Time progressive photographs of the low sedimentation model (Model 2). Each photo represents one day of deformation. Bottom scale is in centimeters